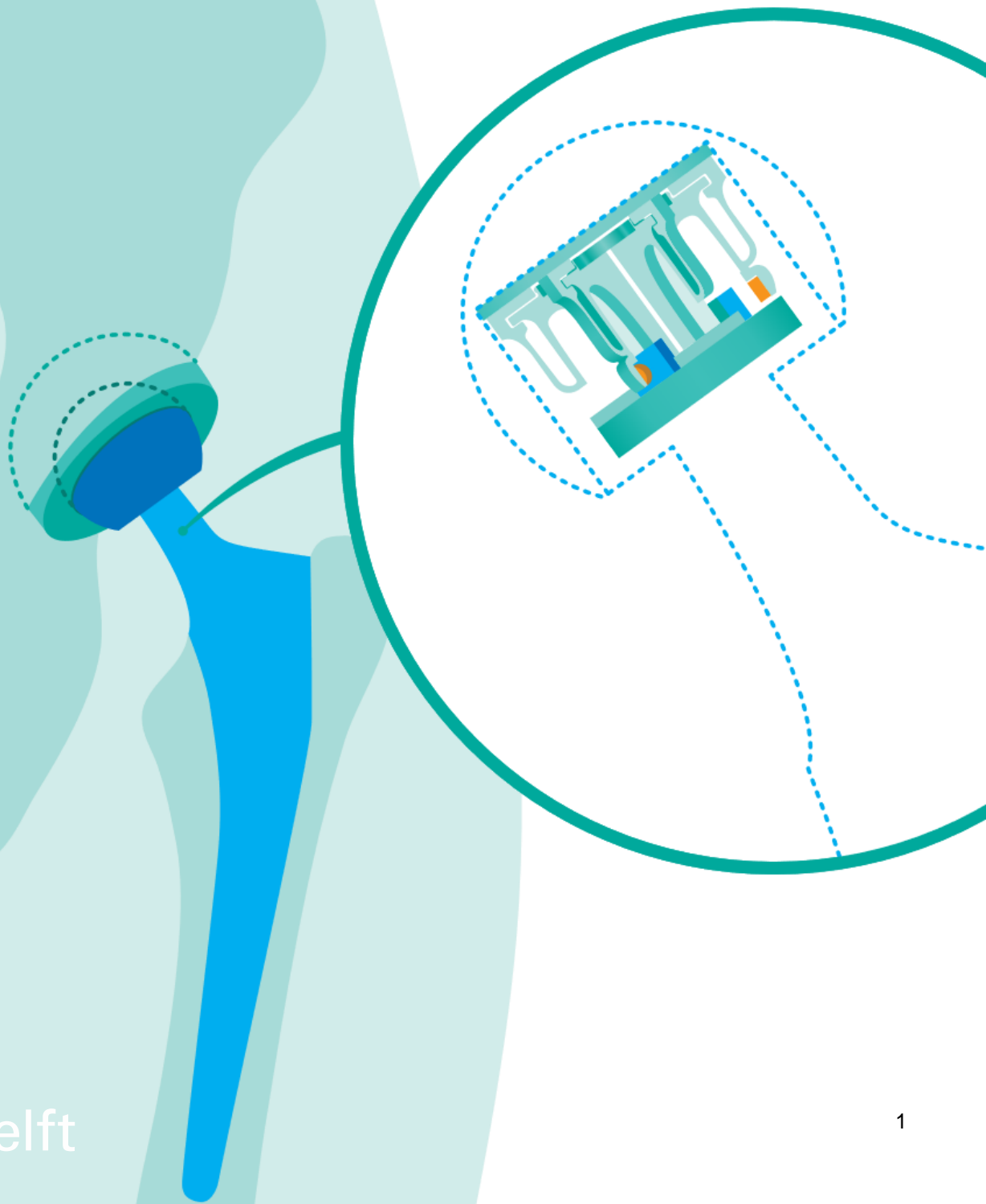


Hip implant force measurement

Design of an intraoperative hip joint
3-DOF force measurement system



Hip implant force measurement

Design of an intraoperative hip joint 3-DOF force measurement system

By

Tessa Mol

in partial fulfilment of the requirements for the degree of

Master of Science

in Biomedical Engineering

at the Delft University of Technology,

to be defended publicly on Friday November 3rd, 2023, at 13:45.

Student Number:	4158199	
Supervisors:	Dr.Ir. T. Horeman,	TU Delft
	Dr. Jonathan Wei	TU Delft
Thesis committee:	Dr. A. Hunt,	TU Delft

An electronic version of this thesis is available at <http://repository.tudelft.nl/>.

Preface and acknowledgements

Dear reader,

thank you for showing interest in my graduation project. It was fun and challenging to design an instrumented medical device which had to fit in the limited space of a hip prosthesis. The paper can be read by itself, but Appendix A gives supplemental information about total hip replacement surgery, including relevant anatomy, surgical techniques, and reasons why a patient would need this surgery.

During my graduation project, I've received support from many wonderful people whom I would like to acknowledge here. I would like to thank my supervisors Tim Horeman and Jonathan Wei for providing me with valuable feedback. Mark Röling, thank you for sharing your soldering skills and your knowledge about PCB design, electrical circuits, and all other things vaguely electrical that I had questions about. I'm also very grateful to Thyco van Engelshoven and Daniel Kalcevic, for combing through my paper and providing constructive and often very detailed comments. Marloes, thank you for your valuable insights. Reinier van Antwerpen, Damian van Nijs, and Bert Bakker, thank you for your much needed contributions to the production of my prototypes. I would also like to thank Patrick van Holst for lending me his time and knowledge on prototype testing. Mom, thank you for being my sounding board whenever I needed one, and dad, thanks for checking in with me when I was not doing well, it really made a difference. Jeroen, thank you for supporting me during this process and remaining optimistic, even when I was decidedly not.

Tessa Mol

Delft, October 2023

Contents

Preface and acknowledgements	4
Contents	5
Hip implant force measurement.....	7
1 Introduction.....	7
1.1 Project aim.....	9
1.2 Thesis outline.....	9
2 Methods.....	9
2.1 List of requirements	9
2.2 Proof-of-principle	9
2.3 Final design	14
3 Results	18
3.1 Proof-of-principle	18
3.2 Final design	21
4 Discussion	26
4.2 Limitations.....	28
4.3 Recommendations for future research	28
5 Conclusion.....	28
References	29
A Literature study	31
A.1 Anatomy of the hip.....	31
A.2 Hip implant components	34
A.3 Reasons for primary THA	34
A.4 The primary THA procedure	35
A.5 Risks associated with THA for revision surgery	35
A.6 Achieving accurate soft tissue tension	38
A.7 Quantifying soft tissue tension.....	40
A.8 Summary	43
A.9 References	43
B List of requirements	47
B.1 Force reading.....	47
B.2 Corail implant compatability.....	47
B.3 Suitability for in-surgery use	47
B.5 Assignment bounds	48
B.6 References	48
C Mathematical derivation.....	49

D	Comparison between the simulation and the prototype	53
D.1	Method	53
E	Code.....	55
E.1	Matlab code proof-of-principle prototype	55
E.2	Arduino code final prototype	56
E.3	Matlab code final prototype displaying calculated voltages.....	57
E.4	Matlab code final prototype displaying calculated forces	60
F	Material and production method selection	64
F.1	Compliant mechanism	64
F.2	Sensor base	66
F.3	References.....	66
G	Sensor-magnet distance test	67
G.1	Introduction	67
G.2	Method	67
G.3	Results	68
G.4	Conclusion	68
G.5	References.....	68

Hip implant force measurement

Design of an intraoperative hip joint 3-DOF force measurement system

Tessa Mol, Jonathan Wei, Tim Horeman

Abstract: Achieving appropriate soft tissue tension around the hip joint is an important factor for achieving hip stability after Total Hip Arthroplasty (THA). Hip instability leads to dislocations, pain, and is a common reason for early revision surgery. The current soft tissue tension assessments available during surgery rely on experience, and dislocations occur twice as often after THAs performed by inexperienced surgeons compared to more experienced surgeons. This paper presents a new mechanism which measures and displays hip force in Three Degrees Of Freedom (3-DOF) during THA. A prototype measured axial and normal force components up to 75 N with a sampling frequency of 14.6 Hz, an accuracy up to 11 N, and a Root Mean Square Error (RMSE) of 4.0 N (axial) and 3.0 N (normal). Additionally, it measured the normal force direction with an accuracy up to $7.1 \cdot 10^{-2} \pi \text{ rad}$ and RMSE of $7.1 \cdot 10^{-2} \pi \text{ rad}$. Data needs to be collected to build a predictive model which estimates the required hip force range and distribution to achieve a stable joint. When combined with such a predictive model, the proposed design is a promising assistive surgical tool.

Keywords: hip arthroplasty, hip joint force, instrumented prosthesis, hip implant, 3-DOF, intraoperative.

1 INTRODUCTION

Primary Total Hip Arthroplasty (THA) is a surgery in which a damaged hip joint is replaced by a prosthetic joint. Figure 1A shows a diagram of a hip implant. The surgery has a high success rate; 80% of the patients regain their pre-symptomatic sports level [1] and 88% of the patients intending to return to work are able to do so [2]. However, the patients' self-reported long-term physical quality of life and hip functionality remain lower than those of healthy age-controlled individuals [3]. Over two thirds of patients

reported pain in their operated hip, 12% of which was experienced as moderate or continuous. 29% of patients were taking pain relief medication at the time of questioning [3].

30,000 people underwent THA in the Netherlands in 2018 and an additional 4,000 revision surgeries were required to correct artificial joint problems [4]. The number of THAs is increasing and this trend is expected to continue [5], [6]. The incidence of revisions will increase disproportionately [6]. One reason is the increased life expectancy of the last three decades. Implants only have a limited lifespan, and thus need to be replaced more often if usage is prologued. A second reason is the increasing utilisation of primary THAs in patients younger than 65 years. Young patients are more likely to require revision surgery within 20 years after the initial surgery than older patients. Additionally, the time intervals between revisions reduce for each additional revision. The rising incidence of revisions will vastly increase the health care costs and thus an increased focus on revision risk prevention is essential [6].

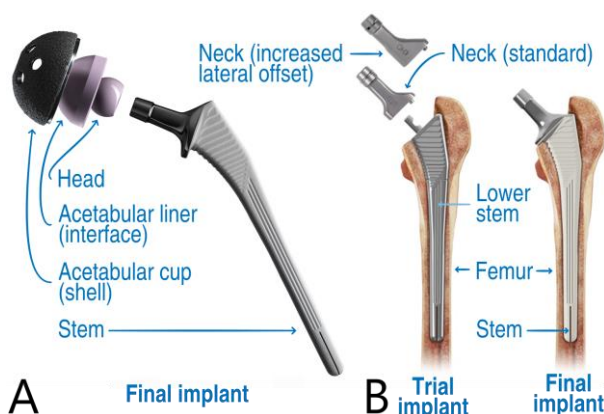


Figure 1: The Corail-Pinnacle hip implant. The exploded view of the implant (A), adapted from [28], and the Corail trial implant compared to the permanent implant (B), adapted from [29].

Hip instability is a common reason for early revision surgery. Retrospective reviews published varying

percentages; Kelmer et al. reported hip instability to be the reason for 18.4 % of revisions performed within 2 years [7]. Other sources mention it to be the cause for 15.5 % to 33 % of revisions performed within 5 years [5], [8]–[11]. Table 1 in Appendix A.5.1 lists the sources with additional information such as year, study group and study size. Incorrect tension in the surrounding ligaments, tendons, and muscles around the hip is a common cause for hip instability [12]. In one study ($n = 55$) the soft tissue tension was four times lower in repeatedly dislocating hips than in stable hips after surgery [13]. Inadequate soft tissue tension can also cause pain, impeded range of motion, and an impaired gait [14].

Surgery influences the soft tissue tension. Surgeons use trial implants, shown in Figure 1B, and stability tests to assess the tension [15]. These tests are subjective, relying on surgeons' experience in performing THAs. The work of inexperienced surgeons leads to twice as many registered dislocations compared to more experienced surgeons [16].

StemForce project

This thesis is part of the StemForce project. The StemForce project develops objective intraoperative testing tools, intended to be used predominantly by inexperienced surgeons to reduce the number of hip implant failures due to deficient soft tissue tension [12].

One such device measures hip force along the axis of a trial implant neck [12]. Figure 2 depicts an exploded view. This device is intended to provide the surgeon with an objective measuring tool providing real-time feedback during THA. Additionally, it can serve as a teaching aid for new surgeons.

The force is measured using a linear Hall sensor. This type of sensor can withstand multiple autoclave

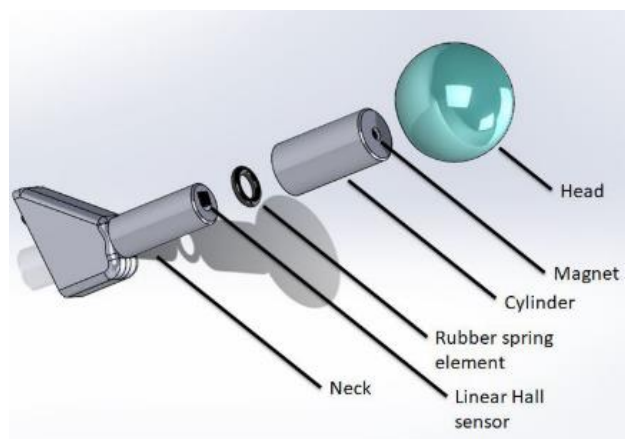


Figure 2: Exploded view of the 1-DOF hip force measuring device.

cycles, is low-cost, easy to use, and has a sufficient resolution and repeatability for its application [12]. Van der Pol did consider other sensor types and sterilized several sensors in an Autoclave ($134\text{ }^{\circ}\text{C}, 2\text{ bar}, 20\text{ min}$). The tested opto-reflective sensor still functioned after sterilization but were deemed less robust and more difficult to apply than a Hall sensor. The tested piezoresistive force sensor and capacitive force sensor did not survive sterilization in an autoclave. Additionally, the strain gage glues suitable for medical use and available in Europe can only be sterilized once by autoclave.

The linear Hall sensor is combined with, a magnet, a sliding bearing, and a compliant o-ring [12]. Axial load on the device compresses the o-ring, reducing the distance between magnet and sensor. The output voltage of a linear Hall sensor is directly proportional to the magnetic field density passing through the sensor [17]. Adjusting the distance of a nearby magnet changes this magnetic field and thus the sensor output, which can be calibrated to the load. The drawbacks of this design are elastic hysteresis in the o-ring and friction in the sliding bearing, which both cause error in the force measurements. Furthermore, this design solely measures force acting along the implant neck axis (axial force). It disregards the force component acting perpendicular to the axis (normal force) and thus cannot determine the magnitude and direction of the resultant force. Additional information on this device can be found in Appendix A.7.2 and in D. van der Pol's MSc thesis [12].

A working principle was proposed within the StemForce project to measure hip forces in Three Degrees Of Freedom (3-DOF). It consists of three linear Hall sensors, each paired with a magnet attached to a compliant mechanical displacement amplifier. These groups are placed rotational symmetrically around the axis of the implant head. The amplifiers are combined into a compliant mechanism. This mechanism has three main functions:

1. allowing for elastic deformation of the mechanism,
2. converting deformation into a unique combination of magnet displacements and thus Hall-sensor outputs,
3. amplifying the displacement of the top of the mechanism into larger displacements of the

magnets, increasing the force sensing sensitivity.

A mechanism using this working principle will be able to measure the applied forces assuming the relationship between the sensor outputs and applied forces is determined.

1.1 Project aim

The aim of this thesis is the design and validation of a new compliant force measurement mechanism which senses hip forces in 3-DOF, is suitable for in-surgery use, and is compatible with the Corail trial hip implant.

1.1.1 Research questions

The design will be validated by answering the following research questions:

1. How successfully can the mechanism measure force in 3-DOF?
2. How suitable is the mechanism during a THA?
3. How well can the mechanism fit within a Corail trial hip implant?

1.1.2 Hypotheses

It is hypothesised that:

1. The mechanism will be able to differentiate between axial force and normal force and load changes in real-time.
2. The mechanism will be sterilisable by autoclave and all non-biocompatible components can be sealed-off.
3. The mechanism will fit within the geometry of the implant head and neck without impeding movement.

If these three hypotheses are demonstrated to be correct, then the proposed mechanism is valid and a device implementing this mechanism will provide accurate and valuable real-time information.

1.1.3 Objectives

The project aim is divided into the following objectives:

1. List the requirements which the mechanism must meet to be suitable for in-surgery use and compatible with the Corail trial implant.

2. Find a mathematical model for the proposed force measurement method.
3. Implement the model such that it can read, process, display, and save all inputs and outputs.
4. Design the mechanism according to the design specifications.
5. Build a physical prototype of the mechanism.
6. Test the performance of the prototype.

1.2 Thesis outline

Section two details the methods used to design and test the new mechanism. The implementation of the mathematical model, design progress, prototyping and testing is divided into two iterations: a proof-of-principle, and a final design. Section three reports the results, section four is a discussion, and section five is the conclusion.

2 METHODS

2.1 List of requirements

The mechanism is designed to the requirements listed in Table 1 (page 10) to be able to sense forces, be compatible with the Corail trial implant, and be suitable for in-surgery use. These requirements assume the mechanism measures the force on the hip implant in components, as depicted in Figure 3 on page 11. A Cartesian coordinate system was fitted on the implant head, with the origin in the centre of the head and the z-axis along the axis of the head. The force is measured in an axial component, measured along the z-axis, a normal component, measured in the xy-plane, and angle α . Angle α , which ranges from 0 rad to $2\pi \text{ rad}$, describes the direction of the normal force component. The angle is measured in a clockwise direction, starting at the x-axis. Additional requirements and justification thereof are listed in Appendix B.

2.2 Proof-of-principle

2.2.1 Mechanism design

Compliant amplifier design

The mechanism was designed by first generating and collecting ideas for compliant mechanical displacement amplifiers (flexors) suitable for a small space and possible configurations thereof. Two possible ideas were modelled in Solidworks (2019, Waltham, USA) one by Tessa Mol, the second by Tim

Table 1: Requirements.

No.	Requirement	Reasoning
FORCE READING		
R.1.1	Sensing range 0 – 150 <i>N</i> for compressive axial forces 0 – 75 <i>N</i> for normal forces 0 – 2π <i>rad</i> for the angle of engagement of the normal force	Dr. B.J. Blaauw estimates the soft tissue tension during a THA to range between 50 – 120 <i>N</i> , with a peak maximum of 200 <i>N</i> [18]. The upper bound of the axial sensing range was set at 1.25 times the upper bound of the force range. The upper bound of the normal force range was set half as high, since most of the tension runs along the axis of the implant [18].
R.1.2	Accuracy <i>Must have</i> 20 <i>N</i> maximum error per force component 0.15π <i>rad</i> maximum error of the force angle if the normal force exceeds 20 <i>N</i> <i>Nice to have</i> 5 <i>N</i> maximum error per force component 0.05π <i>rad</i> maximum error of the force angle if the normal force exceeds 5 <i>N</i>	The required accuracy of the sensed forces is currently unknown. With an accuracy of 20 <i>N</i> and 0.15π <i>rad</i> the device can be used for approximating the force range and distribution within hip joints, information which can be used to update R.1.1 for further iterations of this design. However, I expect an accuracy of 5 <i>N</i> (10% of the lower bound of the estimated tension during surgery) and 0.05π <i>rad</i> , would be required to give sufficient insight into the force distribution within an individual hip.
R.1.3	Minimum resolution 5 <i>N</i>	10% of the lower bound of the estimated tension during surgery.
R.1.4	Minimum frequency 10.3 <i>Hz</i>	Annett et al. found that participants were not able to perceive latencies up to 97 <i>ms</i> when performing inking tasks with a stylus with an obstructed view, and while watching on a separate screen [19]. The surgeon will also be performing a physical task while watching the force display. The latency will not be exceeded if the code runs with a minimum frequency of 10.3 <i>Hz</i> .
CORAIL IMPLANT COMPATIBILITY		
R.2.1	Size May use the space of the Corail trial implant's neck (\emptyset 13 <i>mm</i> , <i>h</i> 38,5 <i>mm</i> cavity: \emptyset 11 <i>mm</i> , <i>h</i> 25 <i>mm</i>) and head (\emptyset 32). The geometry may exceed these sizes, but then the restrictions in implant range of motion must be determined	Geometry exceeding the size of the final implant will restrict the range of motion of the joint and might alter the force distribution on the implant.
SUITABILITY FOR IN-SURGERY USE		
R.3.1	Maximum deformation 1 <i>mm</i> while subjected to a load of 40 <i>kg</i>	This value was determined in consultation with MD Bryan Blaauw in an earlier StemForce thesis [12].
R.3.2	Maximum static load 300 <i>N</i> compressive axial force and normal force must be withstood without breaking or permanently deforming	The maximum expected hip force of 200 <i>N</i> multiplied by a safety factor of 1.5.
R.3.3	Biocompatibility All materials in direct contact with the patient must be biocompatible and resistant to bodily fluids. Wire connections must be sealed	The device must be safe for use in patients.
R.3.4	Sterilizability Must withstand temperatures up to 135°C and pressures up to 3.1 bar during at least three autoclave cycles.	Autoclaves have different types of sterilisation programs. The devices reach temperatures of around 110 – 135 °C, and pressures up to 3.1 <i>bar</i> [20], [21].

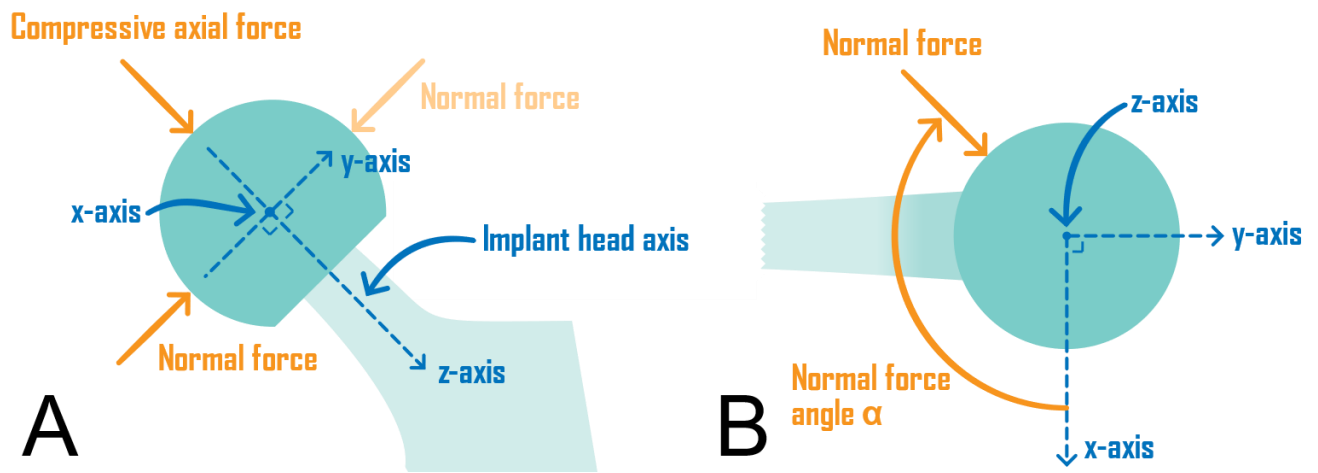


Figure 3: Force components measured by the mechanism, view in the yz-plane (A) and the xy-plane (B).

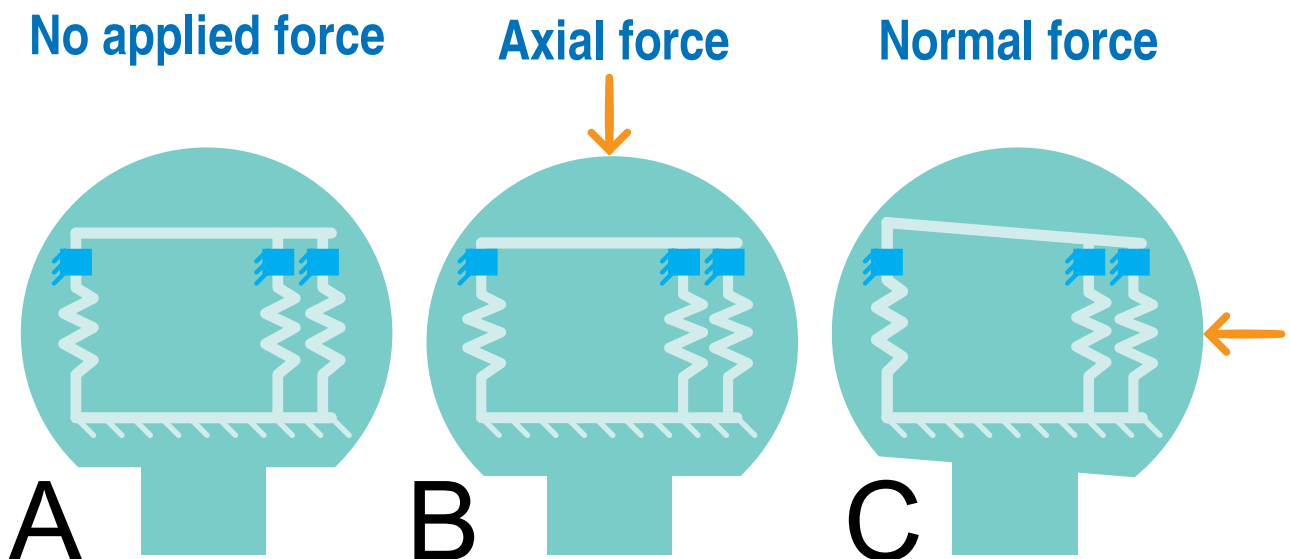


Figure 4: Schematic view of the compliant mechanism (A) and its expected deformation when axial force (B) or normal force (C) is applied to the implant head.

Horeman. The flexors were modelled in 2 mm thick spring steel (AISI 301). Simulations were run on both designs with an applied axial load of 30 N. The designs were compared based on displacement of the top of the mechanism and the displacements where the magnets would be attached, the amplification rate of the displacement, and the maximum internal stress. Due to similar results, the expected ease of prototyping was considered as well.

Converting normal force into an internal moment

The flexor type used in both ideas was designed for amplifying a displacement due to (de)compression between its top and bottom into a larger displacement of the extremity to which the magnet will be attached. When installed lengthwise along the z-axis of the compliant mechanism, this flexor is well suited for amplifying displacements caused by force load in the axial direction. However, this type of flexor is unsuitable for forces directed from its side; it does not

amplify the displacement and it lacks stiffness. Sliding pivots were added to each flexor to restrict translation along the xy-plane. When force is applied to the implant head, normal to the axis, the pivots provide an equal reaction force in the opposite direction. These forces cause an internal moment, assuming they do not act on the same place on the z-axis. The moment leads to varying levels of lengthwise (de)compression in the amplifiers, depending on the direction and magnitude of the applied normal force. When axial force is applied to the implant head, the flexors can slide freely along the pivots. Figure 4 shows a schematic view of the expected elastic deformation, in which the amplifiers are simplified into springs and the sliding pivots into sliders.

2.2.2 Mathematical model

The mathematical model describes the relationship between the force on each flexor and the force components of the applied force. These components are the axial force, the normal force, and the normal force angle α depicted in Figure 3 on page 11. In the mathematical model, the compliant mechanism is simplified into linear springs and rigid beams. It was assumed that no external moments act on the mechanism and implant head, as well as that the applied force always goes through the centre of the head. These assumptions are made because both the acetabular liner and the implant head are spherical and that the force acting on the implant head is acting through the acetabular cup. The soft tissue tension surrounding the joint should keep the head in position. Additionally, both connecting surfaces are smooth, which minimises friction. It was further assumed that the top of the mechanism can only translate in the axial direction (z-axis) and rotate around the mechanism's x- and y-axes, as shown in Figure 5. Translation around the x and y-axes and rotation around the z-axis are assumed to be impossible due to the pivots and the stiffness of the frame of the mechanism. The applied force was simplified and resolved into a normal and an axial point force component. Equations of equilibrium were combined with the linear spring formula and rewritten into the mathematical model, as shown in Results section 3.1.2. The full derivation is described in Appendix C.

2.2.3 Mathematical model implementation

Code was written in Matlab (2019A, Natick, USA) to record, save, and display the sensor outputs during testing, see Appendix E.1. This code was a precursor to code implementing the mathematical model and was used to check whether it displayed the sensor outputs correctly.

2.2.4 Prototyping and testing

A proof-of-principle test (see section 2.3.4) was performed with a physical prototype of the best idea. This prototype included an implant head, 3 Hall sensors, 2 magnets and a sensor base to hold the sensors in place. One of the sensors was not paired with a magnet, and consequently it could sense the interference of the other magnets. The prototype was produced in house using readily available materials. The prototype was connected through an Arduino Uno (Somerville, USA) to a laptop running Matlab (2019A, Natick, USA).

Test set-up

A Materials Testing Machine (MTM) (Zwick Z005, Zwick/Roell, Ulm, Germany) was used to apply force on the head of the proof-of-principle prototype. The set-up is shown in Figure 6A and close-ups of the prototype in multiple load cases are shown in Figure 6B-D. The elapsed time, applied force, and displacement of the load frame were recorded using the MTM. The prototype outputs were recorded for analysis compared to the MTM data.

2.2.5 Protocol

The maximum travel speed was 20 mm/h . This test consisted of three phases:

1. Axial force $0 - 30\text{ N}$

The force was cycled in 3 N increments. Each increment was held for 4 s . This was repeated three times.

2. Normal force, $0 - 30\text{ N}$

Identical to phase one, except that the force was applied perpendicular to the implant axis, with $\alpha = 0\text{ rad}$.

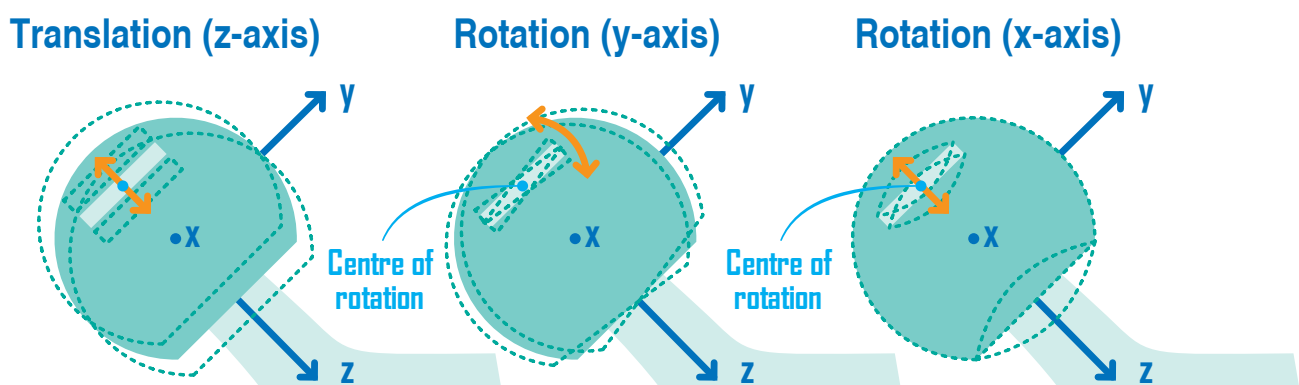


Figure 5: Possible displacements of the top of the mechanism and implant head.

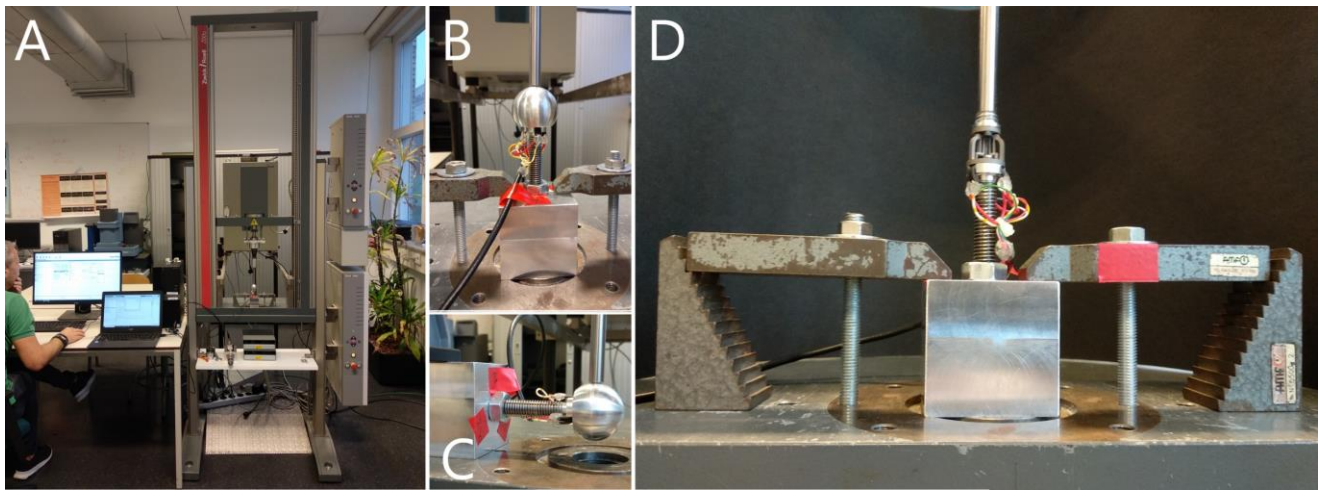


Figure 6: Test set-up. An overview of the set-up during the proof-of-principle test (A), and close-ups during axial loading (B), normal loading (C), and axial loading without the prototype head.

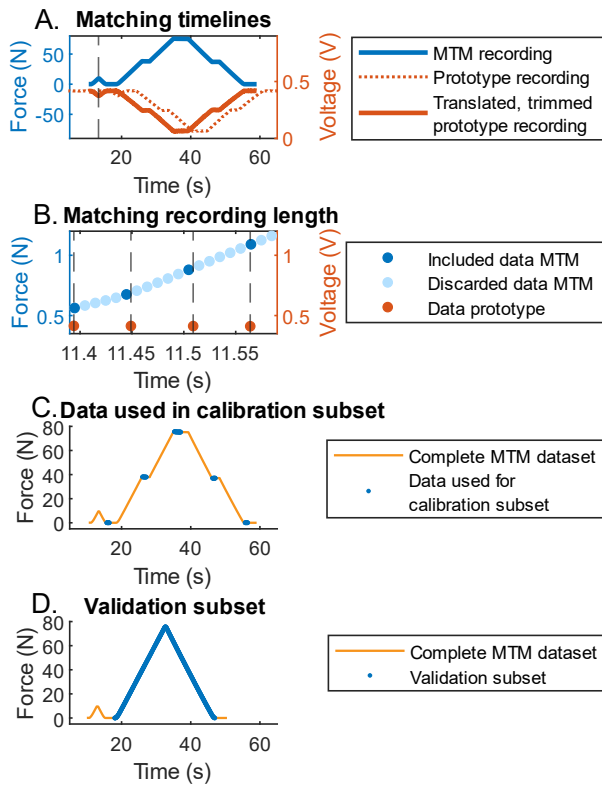


Figure 7: Figures showing how the data was divided and preprocessed, shown on data of the final force test. A visualisation of synchronizing the MTM and prototype data (A), a visualisation of which MTM data was discarded (B), force data of the calibration data subset (C), and Force data of the validation data subset (D). This figure uses data from the final test.

3. Axial force 0 – 65 N

The force was cycled. The head of the prototype was removed to expose the mechanism. The prototype was photographed at the extremes of the load cycle.

Data processing

Preprocessing of data

The prototype and MTM data were synchronized by visually matching peaks in the applied force and

voltage outputs. Data outside the test phase time frame was discarded, as shown in Figure 7A. The sampling rate of the MTM was higher than that of the prototype. The MTM datasets were reduced by matching the nearest timestamp data points and discarding the remaining points, visualised in Figure 7B. Hereby the MTM and prototype datasets equalled in total number of samples.

Creating data subsets

Per test run, two data subsets were created: one for validation and one for calibration. The validation subset only includes dynamic load data, visualised in Figure 7D. The calibration subsets consisted of 3 force input and 3 voltage output values per sensor. Each value was the mean of 32 data points recorded at either no load, maximum load, or the halfway point, from both the loading and the unloading curve. This is visualised in Figure 7C. Test phase 3 did not have a static loading step at the halfway points. The datapoints closest to the halfway points were used instead.

Axial force calibration and assessment

Three types of regression lines were fitted on the calibration subset of sensor 1 and 2 of test phase 3:

$$F = a \cdot V + b \quad \text{Eq.1}$$

$$F = a \cdot V^2 + b \cdot V + c \quad \text{Eq.2}$$

$$F = -\log_a(V - 2.5) - b \quad \text{Eq.3}$$

Where V is the input voltage in volts and F is the applied force per flexor, one third of the total applied force, in Newtons. The asymptote of the logarithmic equation is set at 2.5 V, which is the quiescent sensor output. No regressions were fitted to the data of sensor 3 since this sensor was not paired to a

magnet. The deviations of the regression lines were assessed using the Root Mean Square Errors (RMSE) to the validation subset. For these tests the regression line with the lowest deviation is the most suitable.

The most suitable regression type was fitted on the validation subset of test phase 3 as well, and the RMSE was calculated. The effect of using a data subset of 3 datapoints for calibration instead of the more extensive validation subset was assessed by comparing the RMSEs of the most suitable regression type fitted to both data subsets.

The most suitable type of regression was fitted on the calibration data of test phase 1.

Calculation of forces

The mathematical model with the determined regression lines in conjunction with the validation data of test phases 1 and 2 were used to calculate the force on the implant head. The regression line and data of sensor 2 were duplicated and used for sensor 3. The original data of the third sensor could not be used in these calculations since the sensor was not paired with a magnet.

The accuracy of the calculated forces was assessed using the maximum error and RMSE to the applied forces. A constant c was added to the part of the mathematical model calculating normal force to improve accuracy. This constant was determined by minimising the RMSE of the calculated normal forces on the data of test phase 2.

Review data

The update frequency of the voltage output was calculated using the whole datasets. The noise of the voltage output signal was quantified as the standard deviation of the first 32 data points of each voltage recording. The change in voltage output resulting from a change in force, was determined using the calibration subset.

The minimum voltage resolution was determined using:

$$V_{res} = \frac{V_{operating}}{2^{bits}} \quad \text{Eq.4}$$

where V_{res} is the minimum voltage resolution, $V_{operating}$ is the operating voltage of the Arduino, and bits is the number of bits of the Analog-to-Digital Converter (ADC) of the Arduino. The minimum force

resolution in Newtons is based on both the minimum voltage resolution and the regression line describing the relationship between the voltage input and force output. It was calculated per sensor, at the largest slope of the regression lines. The following equation was used:

$$F_{res} = regression(V_{slope} + V_{res}) - regression(V_{slope}) \quad \text{Eq.5}$$

In which F_{res} is the minimum force resolution, $regression$ is the regression equation used during the test, V_{slope} is the voltage value of the calibration subset recorded at the steepest part of the regression, and V_{res} is the minimum voltage resolution.

The change in voltage output of each sensor in unloaded state over the duration of the test is calculated by subtracting the mean of the last 32 data points of the last recording from the mean of the first 32 data points of the first recording.

The maximum deflection was calculated using the validation subsets of test phases 1 and 2, subtracting the travel at the start of the recording from the maximum travel, averaged between the three test cycles per test phase.

Comparison of physical testing to simulations

The accuracy of the simulations was estimated by comparing the simulated displacements to the displacements observed during the third test phase (normal loading, without prototype head). The displacement was measured at the centre of the area of the flexors where the magnets were attached.

The displacement during the physical test was estimated by comparing the photographs made of the prototype while in unloaded state and while subjected to 65 N axially. The photos and further details can be found in Appendix D. The digital 3D model was subjected to an axial force of 65 N.

2.3 Final design

The mechanism was redesigned to meet the list of requirements. The results of the proof-of-principle test were used to further improve the mechanism's design.

2.3.1 Mechanism design

Mechanism geometry

The geometry of the compliant mechanism was optimised in Solidworks (2021, SolidWorks Corp., Waltham, USA) for the maximum displacement of the magnet, while maintaining the full sensing range. The compliant mechanism was designed with interlocking geometry to protect it from plastic deformation. The mechanism was simplified to a single part during the load simulations to reduce the required computing power. The required load range was doubled during these tests to correct for a simulation inaccuracy found during the proof-of-principle test.

The sensors were placed further apart to reduce the interference between sensor-magnet pairs. The sensor base and implant head were updated to be compatible with the new geometry. A cavity was added to the bottom of the sensor base to hold a Printed Circuit Board (PCB). A 'connector part' was designed to close off this cavity, to guide the wires, and to connect the device with a base for testing.

Materials and production processes

The material of the compliant mechanism was changed, as the requirements could not be met using the material of the first prototype. The material database Granta EduPack (2021 R2, Ansys, Canonsburg, USA) was used to find both biocompatible materials with a high yield strength and high elasticity, as well as suitable production methods. The material and production methods were selected based on suitability, availability, and price. The material of the sensor base was changed to a plastic to avoid short circuits. Several sources were accessed to find materials retaining their mechanical properties and with dimensional stability during multiple autoclave cycles. All considered materials can be found in Appendix F.

Instrumentation

The magnet must be small and sterilizable. The flux density of a magnet decreases when the temperature increases from its ambient level. This change is reversible if the maximum operating temperature of the magnet is not exceeded [22]. Therefore, magnet types were identified which have a maximum operating temperature exceeding the temperature reached in the autoclave.

The sensors, magnet types, and the distance between them were optimised for high sensitivity. The outputs of two Hall sensors were charted while several types of magnets were held at varying

distances. Appendix G contains a graph with the results.

The output voltage of linear Hall sensors is sensitive to fluctuations in the supply voltage. The proof-of-principle prototype was supplied voltage through a USB 2.0 laptop port. The output of such a port can range from 4.75 V to 5.25 V and varies depending on the charge of the laptop battery and fluctuations introduced by the laptop components. Additionally, discontinuous power draw of the sensors causes voltage drops. The power supply for the final design is a 7.5 V DC power adapter requiring 230 AC input. The voltage was regulated by a 5 V Low-Dropout (LDO) regulator. The voltage drops were removed by the use of two 10 μ F capacitors. A PCB holding the LDO regulator and capacitors was designed to fit underneath the sensor base. In the final design, shielded wiring was used and an Arduino MKR Zero instead of Uno due to the higher resolution. The magnets were turned around, north pole facing the sensors, ensuring the sensor output voltage will not exceed the operating voltage of 3.3 V of the Arduino MKR Zero.

2.3.2 Mathematical model implementation

Arduino code was written to supplement the existing code in order to increase output frequency and reduce output noise of the sensors, see Appendix E.2. The block-wise average of 16 voltage outputs per sensor is continuously sent to Matlab. The Matlab code was accommodated for the new code, the resulting code can be examined in Appendix E.3. Additionally, the mathematical model was implemented into a copy of the Matlab code to calculate the force components on the mechanism in real-time, see Appendix E.4. The model was amended to allow for normal force calibration. Partial recalibration of the sensors is done at the start of each recording, setting the start value at 0 N. For every sensor, the difference was calculated between the voltage output used during calibration and the average of the first 32 voltage data points of the recording. The subsequently recorded voltages were corrected by this value prior to the conversion to force components.

2.3.3 Prototype

A physical prototype was produced specifically for force testing. Where possible without influencing the test results, materials were swapped for at hand materials to increase prototyping speed and reduce cost. The interlocking geometry was removed from

the mechanism, as the accuracy of the simulations was uncertain. The locking mechanism could engage prematurely, where priority was given to testing the mechanism's capabilities over the full sensing range.

2.3.4 Force test

The test set-up and protocol are based on the proof-of-principle test. The following sections detail the differences and refer to the proof-of-principle test were applicable.

Test set-up

The set-up was similar to the previous one. A wider rod was used in the MTM to apply force to the head of the final prototype, as depicted in close-ups of multiple load cases in Figure 8A-D.

Protocol

The prototype was running on the Matlab code displaying live output voltages. The maximum travel speed can be assumed to be 20 mm/h . Each test iteration started by cycling the force from 0 N to 9 N . This data is only used to synchronize the elapsed time recordings of the prototype and the MTM. This test consists of nine phases on the MTM:

1. Axial calibration $0 - 75\text{ N}$

The force was cycled. 0 N and 37.5 N were held for 2 s , 75 N for 4 s .

2. Axial validation $0 - 75\text{ N}$

The force was cycled. This was repeated three times.

3. Axial validation $0 - 75\text{ N}$

Phase 2 with the speed increased to 30 mm/h .

4. Normal calibration $\alpha = 1.5\pi\text{ rad}$, $0 - 75\text{ N}$

The force was cycled from 0 N to 37.5 N . Then it was cycled from 0 N to 75 N . 0 N was held for 2 s , 37.5 N and 75 N for 4 s .

5. Normal validation $\alpha = 1.5\pi\text{ rad}$, $0 - 75\text{ N}$

Phase 2, but with normal force loading ($\alpha = 1.5\pi\text{ rad}$).

6. Normal validation $\alpha = 1.5\pi\text{ rad}$, $0 - 75\text{ N}$

Phase 5, but with the speed increased to 30 mm/h .

7. Normal validation $\alpha = 0\text{ rad}$, $0 - 60\text{ N}$

Phase 5, but with $\alpha = 0\text{ rad}$, and maximum force of 60 N .

8. Normal validation $\alpha = \pi\text{ rad}$, $0 - 75\text{ N}$

Phase 5, but with $\alpha = \pi\text{ rad}$.

9. Combined validation $\alpha = \pi\text{ rad}$, $0 - 75\text{ N}$

Phase 2, but the applied force comprises of equal parts axial force and normal force.

The maximum applied axial force was reduced from the intended 150 N to 75 N during pre-testing. Sensor 1 made physical contact with a magnet when 75 N was exceeded. The maximum applied normal force ($\alpha = 0\text{ rad}$) was reduced to 60 N .

After the test on the MTM, the prototype was tested displaying live calculated forces:

10. Update frequency assessment

Manual loading of various angles and loads, for 120 s .

This last test phase was only used to measure the update frequency of the calculated forces. This data is not used in the data processing unless specifically mentioned.

Data processing

Preprocessing of data and creating data subsets

The prototype and MTM data were synchronized by visually matching the peaks of the synchronization step. Thereafter the preprocessing and the creation of data subsets was performed as in the proof-of-principle test. Calibration data subsets were created from test phase 1 and 4, and validation subsets from test phase 2,3, and 5 to 9.

Axial force calibration and assessment

Logarithmic regression lines were fitted on the axial calibration dataset. Eq.3 is adapted to the magnet

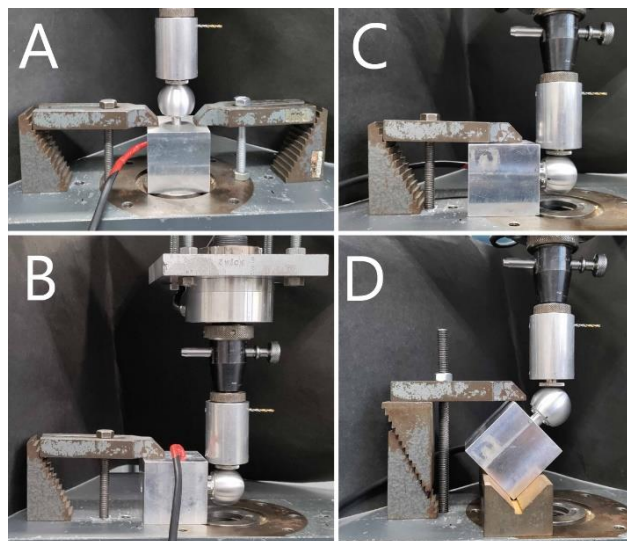


Figure 8: Test set-up close-ups of the final force test. During axial loading (A), normal loading from the $\alpha = 1.5\pi\text{ rad}$ direction (B), normal loading from the $\alpha = \pi\text{ rad}$ direction (C), and combined loading (D).

orientation of the final prototype by mirroring the equation around both $2.5 V$ and $0 N$:

$$F = \log_a(-V + 2.5) + b \quad \text{Eq.6}$$

The voltage output of sensor 3 had a different response above $53.5 N$ axial force compared to the other two sensors. This irregularity was mitigated by creating a piecewise regression, where a logarithmic regression was fitted below $53.5 N$ and a linear regression (Eq.1) was fitted above. Two force input and voltage output values were added to the calibration subset to allow for the piecewise regression: one at $\sim 52.5 N$ and one at $\sim 54.5 N$. These values were the mean of 20 data points, recorded $\pm 1 N$ from $53.5 N$ and outwards. This is visualised in Figure 9. The fit of the four regression lines was assessed using RMSE.

Normal force calibration and recalibration to zero

The prototype was calibrated to normal force by calculating forces using the normal force calibration data subset and determining the multiplication factor needed to match the mean value to the mean applied force. This multiplication factor is entered into the mathematical model for the future normal force calculations.

The zero calibration at the start of each test was done by finding the difference between the voltage output used during calibration and the average of the first 32 voltage data points of the current recording. The voltages inserted into the force calculation equations were adjusted by these differences. This was done for all sensors independently.

Calculation of forces

The amended mathematical model with the determined regression lines in conjunction with the

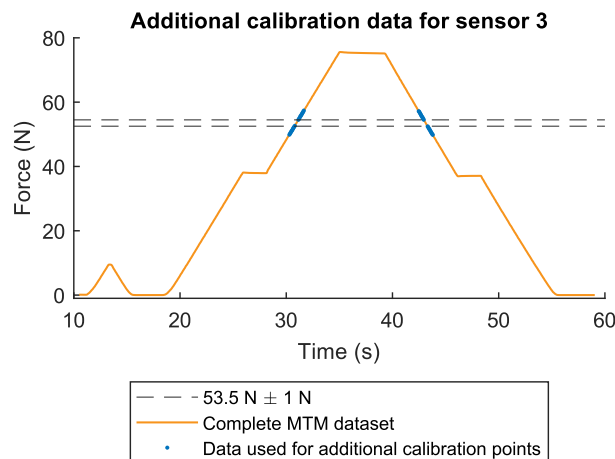


Figure 9: Visualisation of the data used for the extra datapoints in the calibration data subset of sensor 3.

validation data were used to calculate the force on the implant head. The accuracy of the calculated forces was assessed using the maximum error and RMSE to the applied forces.

Review data

The update frequency of the voltage output was calculated using the last dataset (test phase 10). The noise, minimum voltage resolution, change in voltage output of each sensor in unloaded state over the duration of the test, and the maximum deflection were determined using the proof-of-principle test method. The deflection was calculated for each test orientation. The equation used to calculate the minimum force resolution in Newtons (Eq.5) is updated to include the block-wise averaging performed by the prototype:

$$F_{res} = regression \left(V_{slope} + \frac{V_{res}}{n_{avg}} \right) - regression(V_{slope}) \quad \text{Eq.7}$$

In which F_{res} is the minimum force resolution, $regression$ is the regression equation used during the test, V_{slope} is the voltage value of the calibration subset recorded at the steepest part of the regression, V_{res} is the minimum voltage resolution, and n_{avg} is the number of datapoints combined during the block-wise averaging.

The influence of the loading speed was determined by comparing RMSEs of identical set-ups being loaded at different speeds.

Comparison of physical testing to simulations

The accuracy of the simulations was assessed by comparing the simulated deflections of the implant head to the deflections measured during the physical test. Simulations were run with static loads from either the axial or $\alpha = \frac{3}{2}\pi rad$ direction, ranging from $0 N$ to $75 N$ in 4 equal increments. The deflection of the implant head was sampled at the point of contact of the applied load and measured collinearly.

The deflections during the physical test were calculated from the validation data subsets of test phases 2 and 5. They were determined as the difference between the travelled distance and the initial travelled distance in the validation data subset. The average of the travelled distance was determined per load magnitude ($\pm 0.5 N$) and orientation.

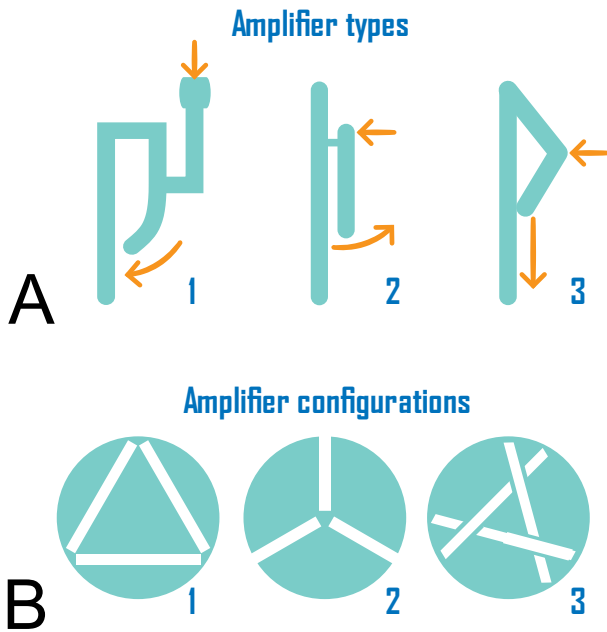


Figure 10: Promising amplifier types and configurations.

Table 2: Characteristics of the compliant mechanism ideas when subjected to 30 N in the axial direction.

	Idea 1	Idea 2
Displacement top [mm]	$-1.4 \cdot 10^{-2}$	$-4.4 \cdot 10^{-2}$
Displacement magnet [mm]	$-2.9 \cdot 10^{-2}$	$-8.8 \cdot 10^{-2}$
Amplification factor	2.1	2.0
Maximum internal stress [MPa]	$1.6 \cdot 10^8$	$1.7 \cdot 10^8$

3.1 Proof-of-principle

3.1.1 Compliant mechanism design

Figure 10 shows the selected amplifier types and configurations, and Figure 11A and C show the two proposed compliant mechanisms. Figure 11B and D show the deformation, magnified for visibility, in both ideas when 30 N is applied in the axial direction. shows that both ideas had similar performance when based on the maximum internal stress and the amplification rate of the displacement by the amplifiers when subjected to a simulated axial force. The second idea had a larger displacement of the magnets and could be fully constructed out of plate metal. Based on these results, the second idea was selected for further development.

3.1.2 Mathematical model

Angle α is 0 rad if the normal force is applied from the direction of sensor 1 and increases in a clockwise direction, as shown in Figure 12A. The z-axis runs along the axis of the implant head and the mechanism. Each flexor was simplified to a horizontal arm with constant length d , and a vertical linear spring, see Figure 12B. The springs are not subject to normal forces, see Figure 12C. The moment arm h of the applied normal force component is simplified to a constant. F_{stop} prevents translation along the x- and y-axes.

The forces on each flexor are converted to an axial component, the normal component, and the

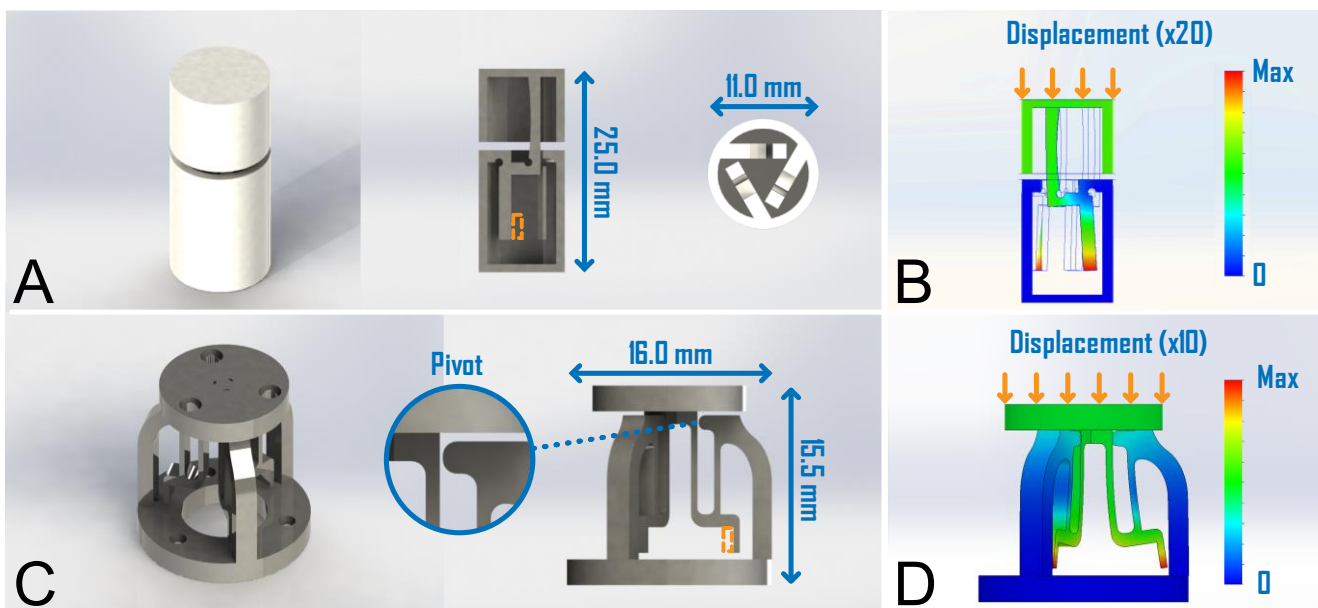


Figure 11: Proof-of-principle designs of the compliant mechanism. The first idea (A), the displacement in the first idea when subjected to 30 N in the axial direction (B), the second idea (C), and the displacement in second idea when subjected to the same force (D). The orange outline signifies the magnet placement.

directional angle α of the normal component of the total applied force using the following:

$$F_{ax} = F_1 + F_2 + F_3 \quad \text{Eq.8}$$

$$F_n = \frac{d}{h} \left(F_1 \cdot \cos(\alpha) + F_2 \cdot \cos\left(\alpha - \frac{2}{3}\pi\right) + F_3 \cdot \cos\left(\alpha - \frac{4}{3}\pi\right) \right) \quad \text{Eq.9}$$

$$\alpha = \arctan\left(\frac{3 \cdot F_1 + 6 \cdot F_2 - 3 \cdot F_{ax}}{3\sqrt{3} \cdot F_1 - \sqrt{3} \cdot F_{ax}}\right) + n \cdot \pi \quad \text{Eq.10}$$

In which:

- F_{ax} is the axial force applied to the prototype, which is visualised in Figure 12B,
- F_1 is the internal force acting on flexor 1, visualised in Figure 12C,
- F_2 and F_3 are the internal forces acting on flexor 2 and 3 respectively,
- F_n is the normal force applied to the prototype, visualised in Figure 12A,
- d is the distance between the spring of the flexors and the centre of the mechanism, visualised in Figure 12A-B,
- h is the moment arm of the applied normal force, visualised in Figure 12B,
- α is the angle of application of the applied normal force, visualised in Figure 12A.
- $n \in \mathbb{Z}$

If the calculated normal force is negative, this is corrected by changing its sign and adding $\pi \text{ rad}$ to α . Thereafter, the angle is corrected to be within $0 \text{ rad} \leq \alpha \leq 2\pi \text{ rad}$.

3.1.3 Mathematical model implementation

The code which records, saves, and displays the sensor outputs of the proof-of-principle prototype is included in Appendix E.1.

3.1.4 Proof-of-principle prototype

The proof-of-principle prototype is shown in Figure 13 (next page). The mechanism was constructed out of parts laser cut from 2 mm thick spring steel (AISI 301). The parts were filed, sandblasted, and joined by silver brazing. Two magnets (Wish, San Francisco, USA) were modified from $\varnothing 3 \text{ mm}, h 1 \text{ mm}$ discs to a width of 2 mm. The magnets were glued with CyanoAcrylate (CA) adhesive to the mechanism, across from sensor 1 and 2, south-pole facing the centre axis. Sensor 3 remained unpaired. The top of the mechanism was connected to a $\varnothing 32 \text{ mm}$ aluminium hip implant head using three M2 screws and screw thread. The bottom of the mechanism was screwed to the sensor base using three M2 screws.

The linear Hall sensors (A1324, Allegro, USA) were glued to the sensor base, facing outward. The pins were connected to wires and insulated with shrink wrap and glue. The wires were connected via an Arduino Uno (Arduino, Somerville, USA) to a pc running Matlab (R2019b, Mathworks, Natick MA, US) for data recording and processing.

The prototype was mounted on a threaded rod protruding from an aluminium cube. The rod was secured with an adjusting bolt.

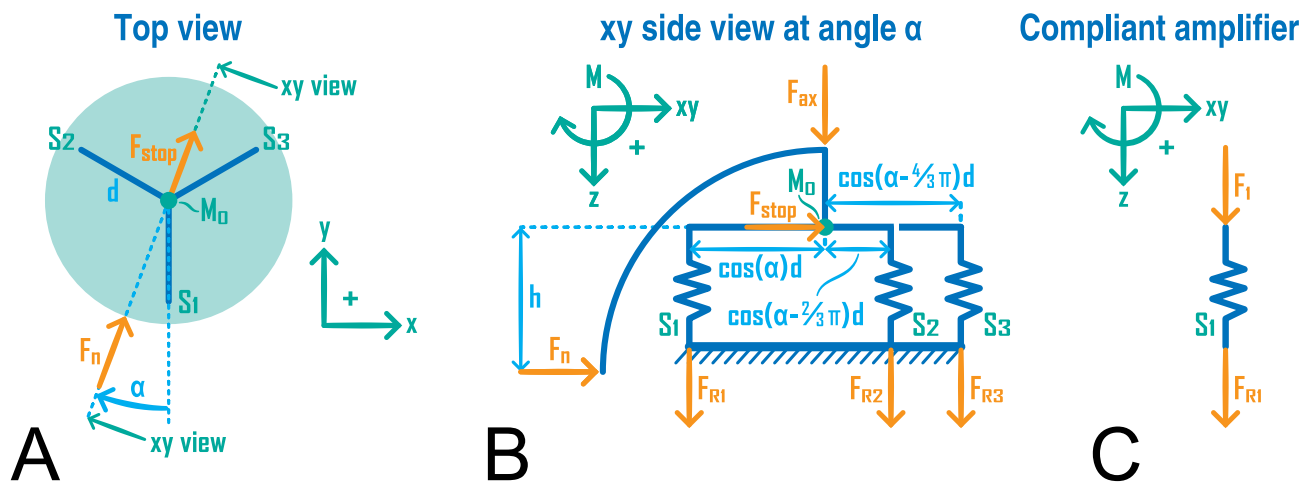


Figure 12: Free body diagrams of the mechanism. A top view, in which the z-axis goes into the page (A). A side view from angle α (B), in which the xy-axis lies in the xy-plane. And the forces acting on flexor 1 (D).

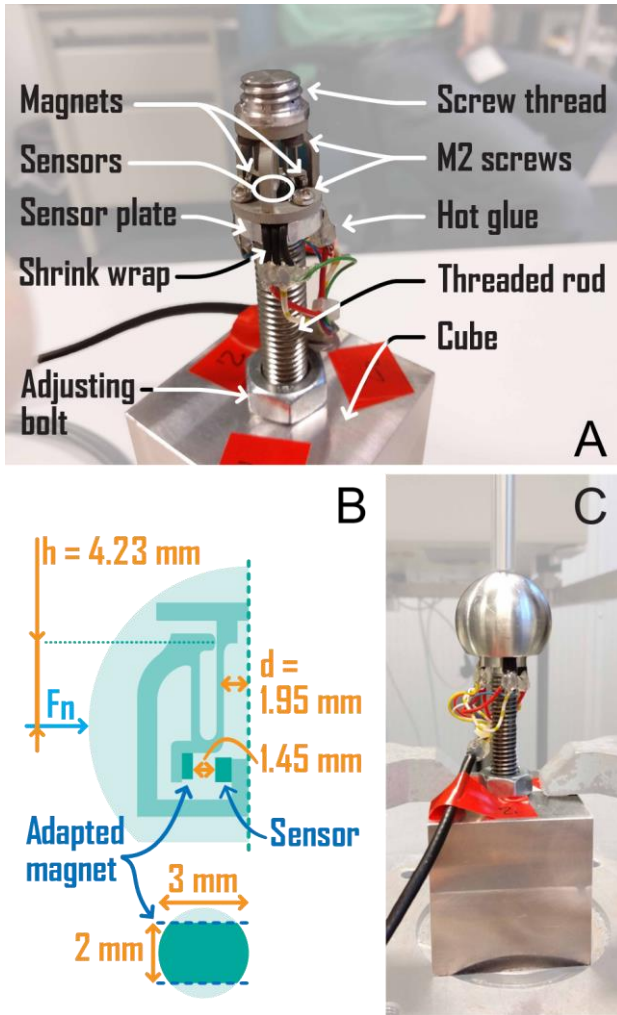


Figure 13: The proof-of-principle prototype, without the head (A), a schematic view of one third of the mechanism (B), and the whole prototype including the head (C).

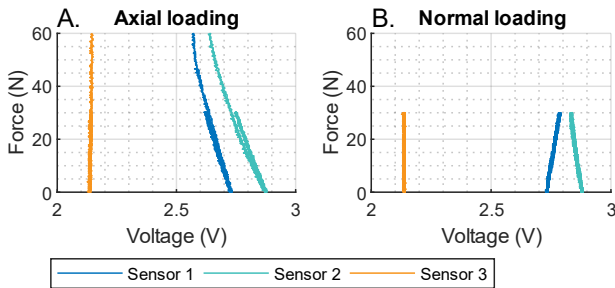


Figure 14: The voltage-force curves of the proof-of-principle test, during axial loading (A), and during normal loading (B).

Table 3: The mean voltage output differences during the first two test phases and in unloaded state over the duration of the test.

Test condition	Mean voltage output difference [V]		
	Sensor 1	Sensor 2	Sensor 3
Axial force 0 N to 30 N	-0.11 (-3.0%)	-0.13 (-4.5%)	(0.28%)
Normal force 0 N to 30 N	$5.4 \cdot 10^{-2}$ (2.0%)	$-4.6 \cdot 10^{-2}$ (-1.6%)	
Whole test 0 N	$-9.2 \cdot 10^{-4}$	$-4.0 \cdot 10^{-3}$	$-7.6 \cdot 10^{-4}$

3.1.5 Proof-of-principle test

Figure 14 shows the relationship between the applied load and the voltage output of the proof-of-principle prototype. Table 3 lists the mean voltage output difference between an unloaded state and when 30 N is applied in either the axial or normal ($\alpha = 0 \text{ rad}$) direction. It also shows the voltage output decrease measured over the duration of the test. Table 4 lists additional characteristics of the prototype. The maximum deflection under normal loading was calculated using only the last two cycles of applied normal force (test phase 2). The first cycle was excluded from this calculation, due to differing too much from the other two and not returning to its initial value, see Figure 15.

Regression assessment and calibration

Figure 16 shows the different regression types fitted on the calibration subset of test phase 3, superimposed over the validation data. Table 6 lists the RMSEs between the regressions and the validation data subset of test phase 3.

Logarithmic regressions provided the best fit on the data of test phase 3 and therefore were used for the prototype calibration, as shown in Figure 17. The goodness-of-fit is listed Table 6. Within the calibration range, the minimum resolutions are 0.62 N and 0.47 N for sensors 1 and 2.

Table 4: Characteristics of the proof-of-principle prototype.

Characteristic	Value
Signal noise standard deviation [V]	$3.2 \cdot 10^{-3}$
Mean sampling frequency [Hz]	8.6
Minimum resolution [V]	$4.9 \cdot 10^{-3}$
Maximum deflection [mm] 30 N axial load	$8.1 \cdot 10^{-2}$
Maximum deflection [mm] 30 N normal load, $\alpha = 0$	0.30

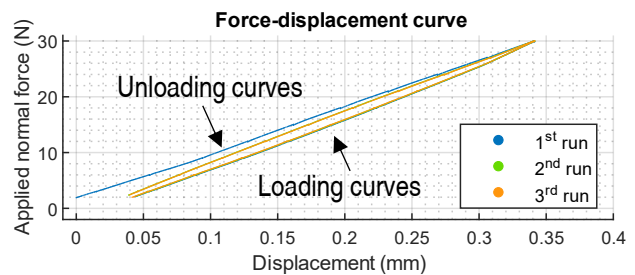


Figure 15: The force displacement curves of the second test phase (applied normal force) lie on top of each other. The loading curve of the first run differs from those of the second and third.

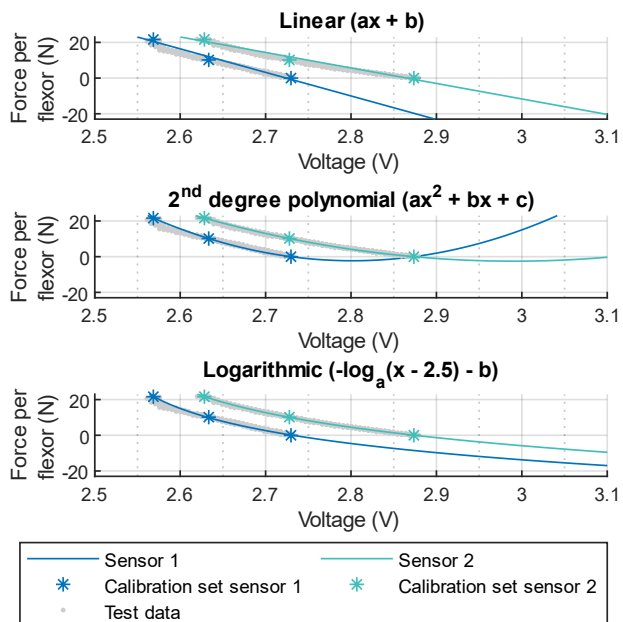


Figure 16: The regression types fitted on the calibration data-subset of test phase 3 (0-65 N axial loading). Linear regression (A), 2nd degree polynomial regression (B), and Logarithmic regression (C).

Table 6: The RMSE between the validation subset of either test phase 1 or 3 and various regression lines fitted to data of the same test phase.

Regression Fitted to data subset	RMSE [N]	
	Sensor 1	Sensor 2
DATA OF TEST PHASE 3 – ASSESSING REGRESSIONS		
Linear Calibration	1.6	1.3
2nd degree polynomial Calibration	1.4	0.50
Logarithmic Calibration	1.2	0.39
Logarithmic Validation	0.79	0.38
(Difference to previous regression)	(-0.38)	(-1.5 · 10 ⁻²)

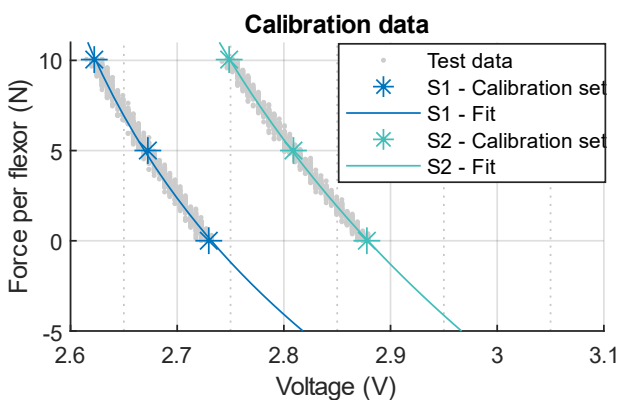


Figure 17: The logarithmic regression lines fitted on the calibration data of test phase 1, superimposed over the validation data.

Table 5: The error between the calculated force components and the applied force during the proof-of-principle test.

Force component	Max Error [V]	RMSE [V]
Axial force	4.2	1.5
Normal force	6.1	1.5

Force calculation

Constant c was added to Eq.9 of the mathematical model:

$$F_n = c \cdot \frac{d}{h} \left(F_1 \cdot \cos(\alpha) + F_2 \cdot \cos\left(\alpha - \frac{2}{3}\pi\right) + F_3 \cdot \cos\left(\alpha - \frac{4}{3}\pi\right) \right) \quad \text{Eq.11}$$

The smallest RMSE between the calculated force and applied force was achieved when constant c was 9.7. Figure 19 (next page) shows the error of the calculated force components for both applied force directions. The maximum error and RMSE of the axial and normal force components are listed in Table 5.

Difference between the physical test and the simulation

The deflection was a factor 2 larger during the physical test than during the simulation.

3.2 Final design

3.2.1 Device design

Compliant mechanism

Figure 18A (next page) shows a render of the compliant mechanism. The mechanism is made from 1.1 mm thick Elgiloy sheet metal. This is a high strength material ($\sigma_y = 1.31 \text{ GPa}$) with high flexibility. Figure 18B shows a side view of one of the flexors of the compliant mechanism. The number of flexors was doubled to six, to enable the mechanism to withstand the full force range. The three extra flexors lack the geometry designed to hold a magnet, since the number of magnets was kept at 3. The flexors are connected through a top and bottom plate and an additional support disc. Each flexor has a pivot with a clearance of 0.1 mm. Combined, the six pivots prevent translation along the x- and y-axes. The geometry above the flexors and the top plate interlocks when the applied force exceeds the sensing range, allowing the mechanism to withstand a simulated axial load up to 300 N and normal load up to 150 N. Table 7 (page 23) lists the distances between the sensors and their paired magnets during various load simulations. These distances are slightly inflated, as they do not take adhesive thickness into

account. Figure 18D shows the displacement within the mechanism when the implant head is subjected to an axial or normal load. This displacement is amplified by a factor 5 to increase visibility. The parts of the compliant mechanism are laser cut with a tolerance of $\pm 0.01\text{ mm}$ and assembled through laser welding.

Instrumentation

Both high temperature Neodymium magnets and Samarium Cobalt magnets were found to be suitable options. They are available in small sizes and have sufficiently high maximum operating temperatures. Both magnet types should be coated to prevent corrosion and to be biocompatible. The chosen

Error of the calculated force components

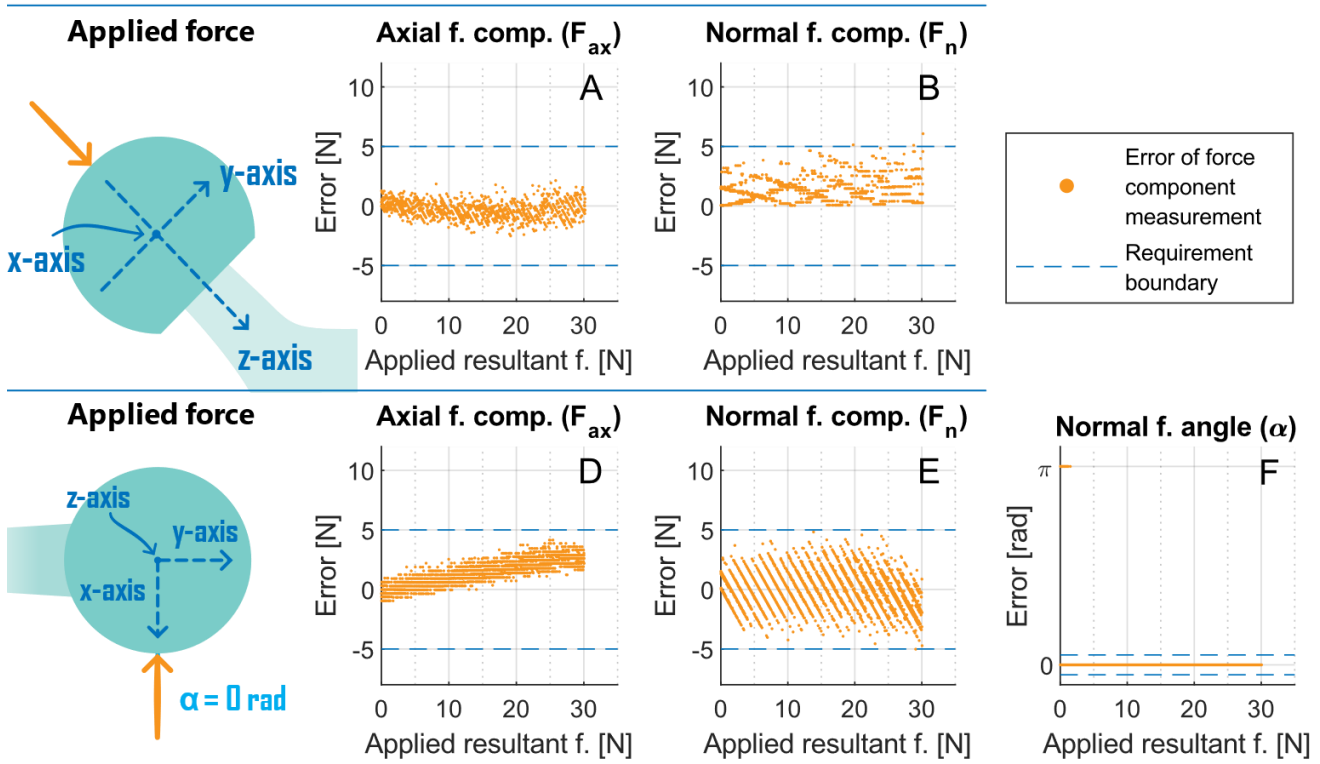


Figure 19: The error of the calculated force components during the proof-of-principle test. The error of the axial force component (A) and the normal force component (B) when force is applied from the axial direction, and the error of the axial force component (D), the normal force component (E), and the normal force angle (F) when force is applied normal to the implant axis.

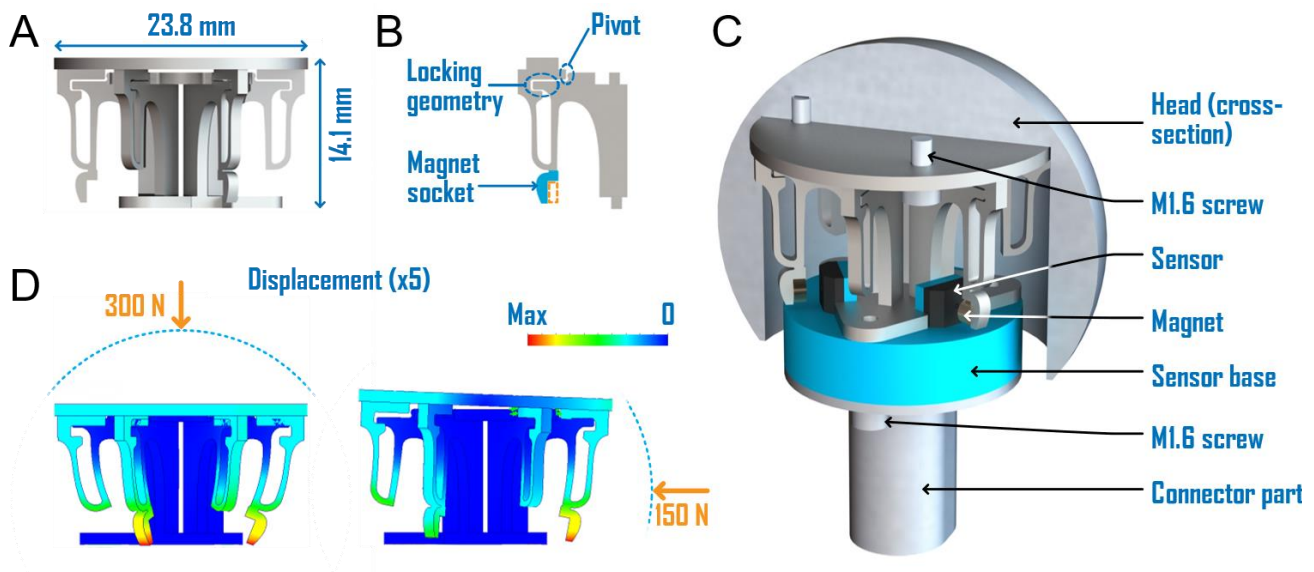


Figure 18: Final mechanism design and behaviour. A side view of the mechanism (A), a flexor of the mechanism (B), the mechanism assembled within the device (C), and the displacement of the mechanism under two different loads, amplified by a factor 5.

magnet type is a $\varnothing 2 \cdot 1 \text{ mm}$ axial disc magnet (Wish, USA), with an approximated remanence field of 3500 Gauss . The magnet is coated and attached to the mechanism using an epoxy based, medical grade, autoclave resistant adhesive such as Dymax's 1040-M [23].

Three linear Hall sensors (A1324, Allegro, Manchester, USA) are soldered to a PCB. This board contains a 5 V LDO (LP2980IM5-5.0/NOPB, Texas Instruments, Dallas, US) and two $10 \mu\text{F}$ capacitors (GRM155R61A106ME11D, Murata, Kyoto, Japan). The power is supplied by a 7.5 V DC power adapter (GST40A07-P1J, Mean Well, New Taipei City,

Table 7: Distance between the sensors and their paired magnets with different simulated load cases.

Applied load			Sensor-magnet distance [mm]		
F_{ax} [N]	F_n [N]	α [rad]	Sensor 1	Sensor 2	Sensor 3
0	0	0	1.3	1.3	1.3
300	0	-	0.85	0.85	0.85
0	150	π	1.58	1.16	1.16
0	150	$\frac{3}{2}\pi$	1.30	1.54	1.07
0	150	0	1.04	1.44	1.44
75	75	π	1.31	1.13	1.13
75	75	0	1.08	1.27	1.27

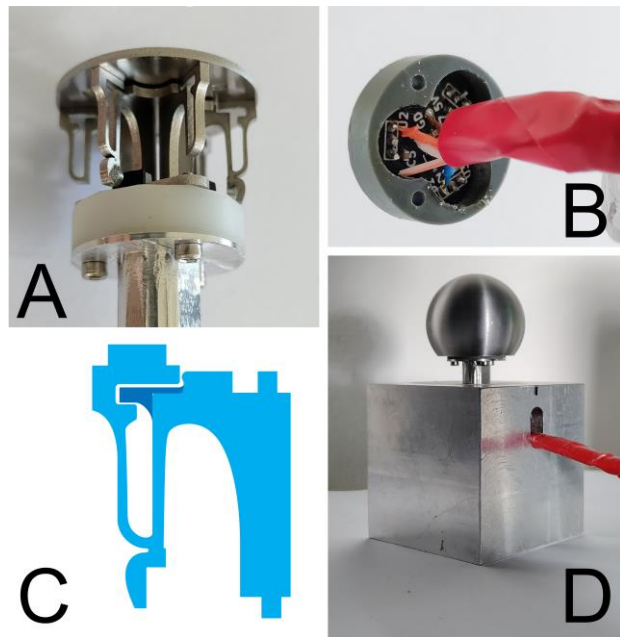


Figure 20: The final prototype. The mechanism (A), The PCB assembled in the sensor base (B), a diagram of the changes in the flexor design for the prototype (C), and the assembled prototype (D).

Taiwan) which plugs into a socket. The sensor output is connected to an Arduino MKR Zero (Arduino, Somerville, USA) through a shielded Ethernet cable (S/FTP cat 7, Allteq, Birmingham, US). The Arduino has an operating voltage of 3.3 V and a 12-bit ADC. The sensors are each facing the north-pole of a paired magnet.

Other parts and connections

Figure 18D shows a render of the assembled device. The sensor base is produced from medical grade polyacetal copolymer. This plastic serves as an electrical insulator, is suitable for both injection moulding and machining, and retains its dimensional and mechanical properties in the autoclave [24], [25]. The sensors and PCB are sealed off and connected to the sensor base using the same adhesive as used for the magnets.

3.2.2 Mathematical model implementation

The constants of Eq.9 were replaced by a constant c , which is determined during calibration in the normal direction. The updated equation is:

$$F_n = c \left(F_1 \cdot \cos(\alpha) + F_2 \cdot \cos\left(\alpha - \frac{2}{3}\pi\right) + F_3 \cdot \cos\left(\alpha - \frac{4}{3}\pi\right) \right) \quad \text{Eq.12}$$

The adapted mathematical model incorporated in the code for the final prototype consists of Eq.8, Eq.10, Eq.12, and the corrective measures listed in section 3.1.2. The code written for the final prototype is included in in Appendices E.2–E.4.

3.2.3 Prototype test alterations

Figure 20D shows the assembled prototype, Figure 20A-B show parts which aren't visible after the full assembly. The locking mechanism was omitted from the flexors in the prototype, shown as the dark area in Figure 20C. The sensor base was 3D printed out of resin and finished by milling. The sensors and magnets were attached using CA adhesive. The electronics were not sealed. The cube from the first prototype was adapted to fit around the connector part and was fixed using CA adhesive as well.

3.2.4 Final force test

The prototype can sense $0 - 75 \text{ N}$ axial force and normal force from the $\alpha = \frac{3}{2}\pi, \pi$ directions, and $0 - 60 \text{ N}$ normal force from the $\alpha = 0$ direction. Figure 22 (next page) shows the relationship between the different loading conditions and the output voltage of the prototype. The voltage-force

curve of sensor 3 diverged from its expected shape when the voltage output was below 0.6825 V. Table 9 lists the mean voltage output differences between an unloaded state and when the maximum load is applied in each test orientation. It also shows the difference in voltage output at the start of test phase 1 and end of test phase 9. The largest changes occurred between measurements with different

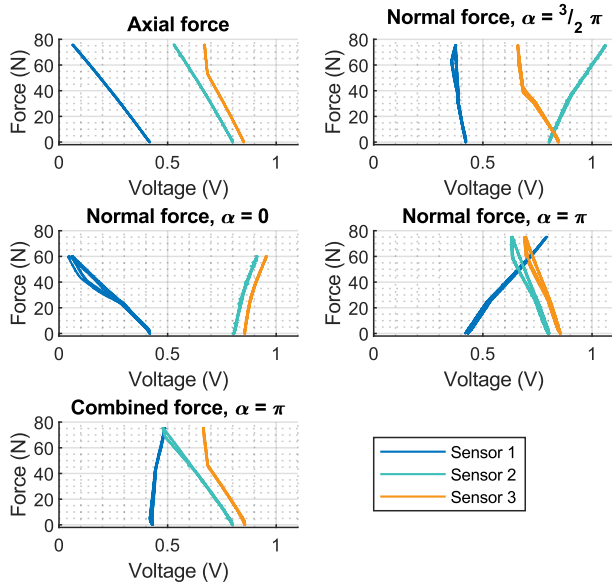


Figure 22: The voltage-force curves of the final prototype test, during loading from four different directions: normal force with $\alpha = \frac{3}{2}\pi$ rad (A), $\alpha = 0$ rad (B), $\alpha = \pi$ rad (C), or a combined force with $\alpha = \pi$ rad (D).

Table 9: The mean voltage output differences in each test orientation and in unloaded state over the duration of test phases 1 to 9.

Test condition	Mean voltage output difference [V]		
	Sensor 1	Sensor 2	Sensor 3
Axial force 0 N to 75 N	-0.35 (-84%)	-0.27 (-34%)	-0.18 (-21%)
Normal force 0 N to 75 N $\alpha = \frac{3}{2}\pi$ rad	$-6.5 \cdot 10^{-2}$ (-15%)	+0.26 (+32%)	-0.19 (-22%)
Normal force 0 N to 60 N $\alpha = 0$ rad	-0.36 (-87%)	+0.11 (+13%)	+0.10 (+12%)
Normal force 0 N to 75 N $\alpha = \pi$ rad	+0.37 (+86%)	-0.17 (-21%)	-0.16 (-19%)
Combined force 0 N to 75 N $\alpha = \pi$ rad	$+5.9 \cdot 10^{-2}$ (+14%)	-0.32 (-40%)	-0.19 (-22%)
Phases 1-9 0 N	$1.3 \cdot 10^{-2}$ (0.99 N)	$1.7 \cdot 10^{-3}$ (0.17 N)	$4.7 \cdot 10^{-3}$ (0.52 N)

prototype orientations and during the first cycle of test phase 8 (normal force, $\alpha = \pi$ rad). Table 8 lists additional characteristics of the final prototype.

Calibration

Figure 21 shows the regressions fitted on the axial calibration data, superimposed over the axial validation dataset. The goodness-of-fit of the regressions are listed in Table 10 (page 26). Constant c of Eq.12 of the mathematical model was set to 1.5072 during calibration in the normal direction. Within the calibration range, the minimum resolutions are $3.9 \cdot 10^{-3}$ N, $5.1 \cdot 10^{-3}$ N and $3.0 \cdot 10^{-2}$ N for sensors 1, 2, and 3.

Force calculation

Figure 23 shows the error of the calculated force components for each loading condition during the test. The calculated force is larger during unloading

Table 8: Characteristics of the final prototype.

Characteristic	Value
Signal noise standard deviation [V]	$8.0 \cdot 10^{-4}$
Mean sampling frequency [Hz]	14.6
Minimum resolution [V]	$5.0 \cdot 10^{-5}$
Maximum deflection [mm] 75 N axial load	$8.0 \cdot 10^{-2}$
Maximum deflection [mm] 75 N normal load, $\alpha = \frac{3}{2}\pi$ or π rad	0.28
Maximum deflection [mm] 75 N combined load, $\alpha = \pi$ rad	0.17

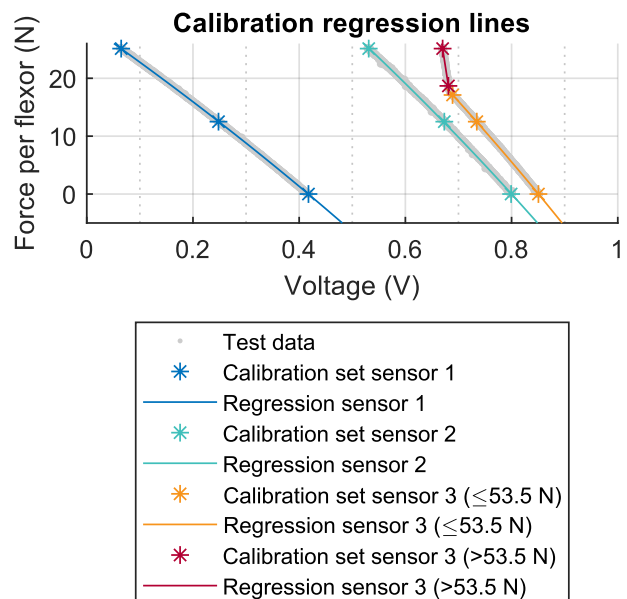


Figure 21: The regression lines fitted on the axial calibration data. An additional linear regression line was fitted on the higher voltage output range of sensor 3.

Error of the calculated force components

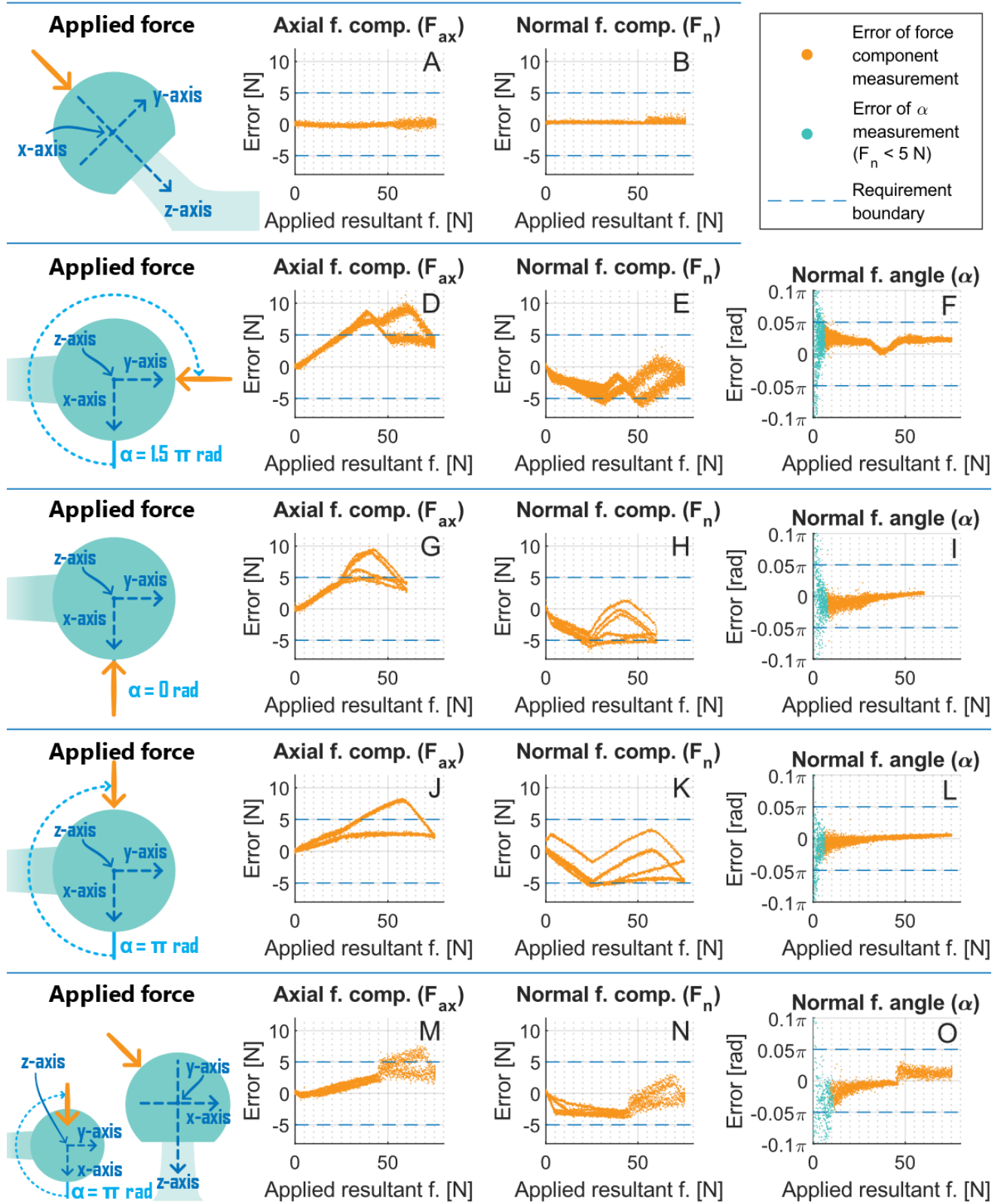


Figure 23: The error of the calculated force components when force is applied along the implant neck axis (A-B, $n = 6$), normal to the axis at angle α is 1.5π rad (D-F, $n = 6$), at angle α is 0 rad (G-I, $n = 3$), at angle α is π rad (J-L, $n = 3$), or when force is applied between the axial and normal direction at angle α is π rad (M-O, $n = 3$). The upper curves are the unloading curves.

than during loading when the applied load includes a normal force component. Table 11 lists the maximum error and RMSE. An increased loading speed had negligible effect on the accuracy of the force calculations; The recorded RMSE differences are between $\pm 2.9 \cdot 10^{-2} N$ and $0.46 N$ and the difference in angle was $4.5 \cdot 10^{-4} \pi rad$.

Difference between physical test and simulation

Figure 24 shows the compression of both the simulated and prototyped mechanisms. Axial loading caused compression around 2 times larger in the prototype than in the simulation. The compression due to normal force loading ($\alpha = \frac{3}{2} \pi rad$) was around 2.5 times larger in the prototype compared to the simulation.

Table 10: The goodness-of-fit of the regressions.

Sensor output Regression type	RMSE [N]
Sensor 1 Logarithmic	0.10
Sensor 2 Logarithmic	0.18
Sensor 3 ($\geq 0.6825 V$) Logarithmic	0.17
Sensor 3 ($< 0.6825 V$) Linear	0.32

Table 11: The error of the calculated force components.

Force type	Max Error	RMSE
Axial force [N]	11	4.0
Normal force [N]	6.8	3.0
Normal force angle α [rad] ($F_n > 5 N$)	$7.1 \cdot 10^{-2} \pi$	$1.6 \cdot 10^{-2} \pi$

Mechanism compression of the prototype and the simulation

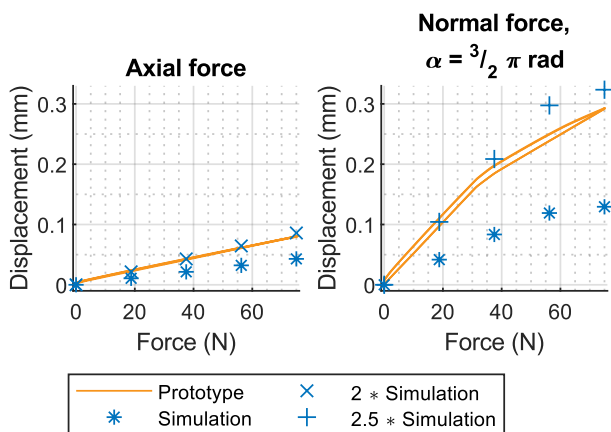


Figure 24: Mechanism compression of the prototype compared to the simulations.

4 DISCUSSION

The aim of this thesis was “*the design and validation of a new compliant force measurement mechanism which senses hip forces in Three Degrees of Freedom (3-DOF) and is compatible with the Corail trial hip implant*”. The designed mechanism is further explored in the following paragraphs referencing the research questions, hypotheses, and design constraints.

4.1.1 How successfully can the mechanism measure force in 3-DOF?

It was hypothesised that the mechanism could differentiate between axial force and normal force and load changes in real-time. This was proven during the force tests. The majority of the force measurement constraints were met by the final prototype. It was able to measure force with a resolution, frequency, and accuracy within the design constraints. The error between the calculated and applied force did exceed the optional tighter accuracy constraints. Lastly, the axial force sensing range of the prototype was only half the required range. When a higher force was applied, one of the magnets came too close to its paired sensor, causing oversaturation. The safety margin within the sensor-magnet distance was too small to compensate for the error margins of the magnets and sensors, the thickness of the adhesive and the error introduced by the manual assembly. It proved to be difficult to position the sensors in the prototype due to soldering them by hand and shrinkage in the sensor base. However, when sufficient distance between the sensors and magnets is ensured, the mechanism is expected to accurately sense forces within the entire range.

Force measurement accuracy

The mathematical model was adjusted to reach sufficient accuracy in normal force calculation. During the proof-of-principle test, the calculated normal forces were off by a factor 9.7 when using the original model. The equation for normal force included two constants: moment arm h and the distance between the springs and the centre of the mechanism d . Both are difficult to determine to a sufficient degree. This was bypassed in the final test by combining all constants into one and determining its value during calibration. However, this did not eliminate all error in the calculated force components. The following paragraphs discuss possible causes.

Clearance of the pivot

One of the simplifications used during the mathematical derivation was that the compliant mechanism could not translate around its x- and y- axes. The mechanism's pivots prevent this movement, but these are only engaged once sufficient normal force is applied. Before that, a small clearance within the pivot (0.1 mm – the cutting width of the laser) needs to be bridged. The delayed engagement of the pivots causes the bend in the mechanism compression graph seen in Figure 24 and in the force-voltage curves when normal force is applied in Figure 22. It also explains the approximately linearly increasing error in the calculated axial and normal force components in Figure 23 when the normal load on the prototype was small.

Friction

The force-error curves in Figure 23 show a difference between the loading and the unloading curves of the flexors with an engaged pivot. The curves are steeper at the start of the unloading curve, due to friction in the pivot. Once the pivot is disengaged, at lower loads, the unloading curves are similar to the loading curves.

The location of the pivot

The model was built on the assumption that normal force would cause the mechanism to pivot around its axis. However, especially in the final design, the pivots are placed further outward. Therefore, the distances between each spring and the centre of rotation were assumed incorrectly. This affects the equation calculating the normal force (Eq.9), since internal moment arms used in this equation have a different length. It also affects the axial force calculation. The reaction forces caused by the applied normal force sum up to zero if the mechanism would pivot around its axis. However, with the current pivot placement they sum up to a negative value. This is not accounted for in the equation calculating axial force (Eq.8). This causes the downward curve visible in the loading curves of the calculated axial force component in Figure 23. This curve is steeper in Figure 23G in which the mechanism pivots around a single pivot than in Figure 23J in which the mechanism pivots around two pivots. The distance between the centre of rotation and the axis is smaller if the mechanism pivots around two pivots, thus the effect should be smaller as well.

Damaged sensor

The sensors of the final prototype were soldered to the PCB by hand. This was difficult due to the small size of the solder pads, the tight placement tolerances, and the proximity of other components. One of the sensors of the prototype was damaged, resulting in an altered characteristic curve at lower voltages. This had to be accounted for during calibration in the test by dividing the curve into two parts. The force-error curves based on the data of the altered characteristic show more noise and are slightly offset with respect to the other force-error data.

Too narrow holes in the sensor base

The holes in the sensor base were too tight for the screws to move freely. This made tightening the screws difficult and a small clearance allowing movement between the mechanism and the connector part might have remained. This could explain the difference between curves in Figure 23K.

4.1.2 How suitable is the mechanism during a THA?

It was hypothesised that the mechanism would be sterilisable by autoclave and all non-biocompatible components could be sealed-off. Theoretically this has been achieved. The materials in direct contact with the patient are biocompatible and repeatably sterilizable by autoclave. The chips can withstand the heat generated during an autoclave cycle. The electronic connections and PCB are located within a sealable cavity.

Additional constraints pertaining to this research question concerned the maximum deformation and the mechanism's ability to withstand forces out of the measurement range. The maximum deformity is within bounds. The mechanism's ability to withstand forces exceeding the measurement range was not tested. The interlocking geometry designed to prevent plastic deformation within the mechanism while subjected to a load exceeding the measurement range was designed using Solidworks simulations. The simulations calculated smaller deformations than were measured during the force tests and that difference was not fully accounted for in the design. Multiple iterations of the design and tests would be required to mitigate this. If the geometry would lock prematurely while still within the measurement range, the expected measurable load range would not be reached.

4.1.3 How well can the mechanism fit within a Corail trial hip implant?

It was hypothesized that the mechanism would fit within the geometry of the implant head and neck without impeding movement. The mechanism, including PCB, fits within the spherical shape of the head. Only the connector part encasing the wires protrudes from this area and this part fits within the geometry of the implant neck.

4.2 Limitations

The performance of the mechanism was tested in a controlled set-up which does not accurately mimic the intended use of the device. The most important difference is that the applied force did not change direction during a test cycle. Therefore, the impact of changing the force direction on the device its performance is unknown. Furthermore, the test set-up was designed under the assumption that all significant forces on the implant head go through its centre. However, little is known about the actual forces in the hip joint during surgery.

The prototype introduced additional limitations, which were not addressed due to time constraints. Only half of the intended force range could be tested due to the oversaturation of one of the sensors. Additionally, one of the sensors was damaged during assembly, which affected the output of the device.

The sterilizability of the design was confirmed in theory. However, this conclusion would be more robust if the effects of repeated sterilisation were tested with accurate prototypes. It was chosen not to perform this test due to cost and time constraints.

4.3 Recommendations for future research

The mechanism

Load Range

Further testing to confirm the prototype can measure the specified load range is required. Reinstalling the sensors with tighter tolerances and re-configuring the magnets would lead to better results. Alternatively, magnets with a weaker magnetic strength could be used.

Increasing accuracy

The force measurement accuracy can be increased by incorporating the bend in the normal force-voltage curves, created by the pivot, into the force equations. Alternatively, the design could be altered to ensure the pivot is engaged at lower applied forces.

The accuracy can be increased further by altering the mathematical model to take the pivot placement into account. If necessary, the six separate pivots could be substituted for a circle-shaped pivot concentric around the axis of the mechanism. This would ensure a consistent distance between the centre of rotation and the axis, no longer dependent on normal force angle α .

Lastly, the accuracy can be increased by reducing the friction on the pivot in the compliant mechanism. For example, with a biocompatible lubricant.

Improved plastic deformation protection

The compliant mechanism must be protected from plastic deformation forces exceeding the force range. This is especially important during the reduction and dislocation of the hip implant. The current interlocked geometry needs to be redesigned, as it is not likely to work as intended. More accurate simulations would benefit this process. Adjusting the settings might improve the simulation outcomes.

Electrical design improvements

Currently the device design ends in the connector part and wires leading to the Arduino. The wires could end in a waterproof socket at the base of the connector instead. Another option would be to combine the connector piece and implant neck into one part. The surgeon tries multiple neck geometries during surgery; thus (dis)assembly should be swift. Therefore, it is important to consider ease of assembly.

Predictive model

A reliable prediction of a proper force range and distribution is required to assist the surgeon in achieving adequate soft tissue tension. Data needs to be collected in a standardized method [12] to build a predictive model. This should include hip force and distribution during standardised range of motion tests and parameters known to influence the hip force. For example, surgical parameters as approach, anaesthesia, and neuromuscular blocking agents and patient parameters including anthropometric variables and activity level [12], [26], [27].

5 CONCLUSION

This paper presents a new device which measures and displays hip forces during THA. The device is intended as an objective measuring tool which supports the surgeon in selecting the appropriate implant geometry. The overarching objective is to

improve patient outcomes by reducing the number of hip implant failures due to incorrect soft tissue tension.

A prototype including a compliant mechanism, Hall sensors, and magnets was successfully developed. The prototype was able to measure axial and normal forces, and a combination of both, providing more insights in all possible load cases. The prototype did not reach all design requirements fully. However, with the results presented in this paper it can be concluded that all requirements can be achieved in future iterations.

With more required data to be collected for a predictive model, further developments in this topic can result in improved patient outcomes. This prototype has shown promising results for the creation of an assistive surgical tool.

REFERENCES

- [1] A. Hoorntje *et al.*, "The Effect of Total Hip Arthroplasty on Sports and Work Participation: A Systematic Review and Meta-Analysis," *Sports Medicine*, vol. 48, no. 7, pp. 1695–1726, 2018, doi: 10.1007/s40279-018-0924-2.
- [2] K. Al-Hourani, D. J. MacDonald, G. S. Turnbull, S. J. Breusch, and C. E. H. Scott, "Return to Work Following Total Knee and Hip Arthroplasty: The Effect of Patient Intent and Preoperative Work Status," *Journal of Arthroplasty*, vol. 36, no. 2, pp. 434–441, 2021, doi: 10.1016/j.arth.2020.08.012.
- [3] M. Mariconda, O. Galasso, G. G. Costa, P. Recano, and S. Cerbasi, "Quality of life and functionality after total hip arthroplasty: A long-term follow-up study," *BMC Musculoskelet Disord*, vol. 12, no. 222, pp. 1–10, 2011, doi: 10.1186/1471-2474-12-222.
- [4] "LROI-rapportage Type of procedures 2010-2018," *LROI*. <https://www.lroi-rapportage.nl/hip-numbers-type-of-procedures-2010-2018> (accessed Jul. 17, 2020).
- [5] K. Liu, W. Wu, and J. Wang, "When and how do prosthetic hips fail after total hip arthroplasties? - A retrospective study," *Journal of the Formosan Medical Association*, vol. 115, no. 9, pp. 786–793, 2016, doi: 10.1016/j.jfma.2015.07.014.
- [6] C. Pabinger, H. Lothaller, N. Portner, and A. Geissler, "Projections of hip arthroplasty in OECD countries up to 2050," *HIP International*, vol. 28, no. 5, pp. 498–506, 2018, doi: 10.1177/1120700018757940.
- [7] G. Kelmer, A. H. Stone, J. Turcotte, and P. J. King, "Reasons for Revision: Primary Total Hip Arthroplasty Mechanisms of Failure," *J Am Acad Orthop Surg*, vol. 29, no. 2, pp. 78–87, 2021, doi: 10.5435/JAAOS-D-19-00860.
- [8] N. G. Burke, J. P. Gibbons, A. J. Cassar-Gheiti, F. M. Walsh, and J. P. Cashman, "Total hip replacement — the cause of failure in patients under 50 years old?," *Ir J Med Sci*, vol. 188, no. 3, pp. 879–883, 2019, doi: 10.1007/s11845-018-01956-8.
- [9] J. S. Melvin, T. Karthikeyan, R. Cope, and T. K. Fehring, "Early Failures in Total Hip Arthroplasty — A Changing Paradigm," *Journal of Arthroplasty*, vol. 29, no. 6, pp. 1285–1288, 2014, doi: 10.1016/j.arth.2013.12.024.
- [10] K. J. Bozic, S. M. Kurtz, E. Lau, K. Ong, T. P. Vail, and D. J. Berry, "The Epidemiology of Revision Total Hip Arthroplasty in the United States," *J Bone Joint Surg*, vol. 91, no. 1, pp. 128–133, 2009, doi: 10.2106/JBJS.H.00155.
- [11] S. D. Ulrich, T. M. Seyler, D. Bennett, R. E. Delanois, and K. J. Saleh, "Total hip arthroplasties: What are the reasons for revision?," *Int Orthop*, vol. 32, no. 5, pp. 597–604, 2008, doi: 10.1007/s00264-007-0364-3.
- [12] D. Van der Pol, "Assessment of soft tissue tension during total hip arthroplasty." MSc Thesis, Dept. of Biomed. Eng., Techn. Univ. of Delft, Delft, 2017.
- [13] T. Ogawa, M. Takao, H. Hamada, T. Sakai, and N. Sugano, "Soft tissue tension is four times lower in the unstable primary total hip arthroplasty," *Int Orthop*, vol. 42, pp. 2059–2065, 2018, doi: 10.1007/s00264-018-3908-9.
- [14] P. Kosev, B. Valentinov, Y. Andonov, and C. Sokolov, "Soft Tissue Balancing In Total Hip

- Arthroplasty," *Journal of IMAB*, vol. 21, no. 1, pp. 752–756, 2015, doi: 10.5272/jimab.2015211.752.
- [15] M. N. Charles, R. B. Bourne, J. R. Davey, A. S. Greenwald, B. F. Morrey, and R. C. H. "Soft-Tissue Balancing of the Hip," *J Bone Joint Surg*, vol. 86, no. 5, pp. 1078–1088, 2004.
- [16] U. Hedlundh, L. Ahnfelt, C.-H. Hybbinette, J. Weckstrom, and H. Fredin, "Surgical Experience Related to Dislocations after Total Hip Arthroplasty," *Journal of Bone and Joint Surgery*, vol. 78, no. 2, pp. 206–209, 1996.
- [17] "Hall Effect Sensor," *Electronics Tutorials*. <https://www.electronicstutorials.ws/electromagnetism/hall-effect.html> (accessed Aug. 25, 2020).
- [18] N. Zhang, "Three-axis force-sensing hip implant for soft tissue tension assessment during total hip arthroplasty," MSc Thesis, dept. of Biomech. Eng., Techn. Univ. of Delft, Delft, 2020.
- [19] M. Annett, A. Ng, P. Dietz, W. F. Bischof, and A. Gupta, "How Low Should We Go? Understanding the Perception of Latency While Inking," in *GI '14: Graphics Interface*, Montreal Quebec Canada: Canadian Information Processing Society, May 2014, pp. 167–174.
- [20] AutoclaveDepot, "Autoclave Comparison Chart | Compare Autoclaves Midmark & Tuttnauer." <https://www.autoclavedepot.com/autoclave-comparison-chart/> (accessed Sep. 02, 2019).
- [21] S. Ferretti, "Load type and process/ autoclave selection - Basics and Recent Developments for Autoclaves and Lyophilizers." Presentation slides, PDA Europe, Tel Aviv, Israel, Nov. 13, 2017. [Online]. Available: [http://pdaisrael.co.il/131117/PDA Fedegari Sara Ferretti AutoClave Selection.pdf](http://pdaisrael.co.il/131117/PDA_Fedegari_Sara_Ferretti_AutoClave_Selection.pdf)
- [22] "Temperature effects on permanent magnets," *Magnet Expert*. <https://www.magnetexpert.com/technical-advice-for-every-application-magnet-expert-i685/temperature-effects-on-magnets-i683> (accessed Sep. 18, 2023).
- [23] "MD 1040-M Autoclave Resistant Material for Bonding, Potting, or Encapsulating," *DYMAX*. 2022. Accessed: Sep. 21, 2023. [Online]. Available: <https://www.intertronics.co.uk/wp-content/uploads/2021/12/1040-M-PDS.pdf>
- [24] "Better Plastics for Medical Devices," *Modern Plastics*. <https://modernplastics.com/industries/plastic-s-for-medical-devices/> (accessed Mar. 20, 2023).
- [25] "Sterilisable and autoclavable medical grade plastics," *Ensinger Plastics*. <https://www.ensingerplastics.com/en/shapes/plastic-material-selection/sterilisable-autoclavable> (accessed Dec. 21, 2021).
- [26] V. Schwachmeyer, P. Damm, A. Bender, F. Graichen, and G. Bergmann, "In Vivo Hip Joint Loading during Post-Operative Physiotherapeutic Exercises," *PLoS One*, vol. 8, no. 10, pp. 12–14, 2013, doi: 10.1371/journal.pone.0077807.
- [27] S. S. Sathappan, D. Ginat, V. Patel, M. Walsh, W. L. Jaffe, and P. E. Di Cesare, "Effect of Anesthesia Type on Limb Length Discrepancy After Total Hip Arthroplasty," vol. 23, no. 2, pp. 203–209, 2008, doi: 10.1016/j.arth.2007.01.022.
- [28] "Health economics," *CorailPinnacle*. <https://www.corailpinnacle.net/value-solutions/health-economics> (accessed Aug. 04, 2020).
- [29] "CORAIL® Revision," *Corail Pinnacle*. <https://www.corailpinnacle.net/corail/revision> (accessed Aug. 04, 2020).

A Literature study

This appendix starts with a quick overview of the anatomical terms relevant for this thesis, followed by short descriptions of the Corail implant, reasons for THA, and the THA procedure. Thereafter the known risks factors for revision surgery are discussed. Then follows an outline of techniques and tools to achieve proper tissue tension. This appendix ends with a summary emphasizing the need for this thesis.

A.1 Anatomy of the hip

Anatomy is described in universal terminology. Knowledge of these terms is essential to correctly interpret medical descriptions and figures. Figure 1 visualises the relevant anatomical directions and hip movements.

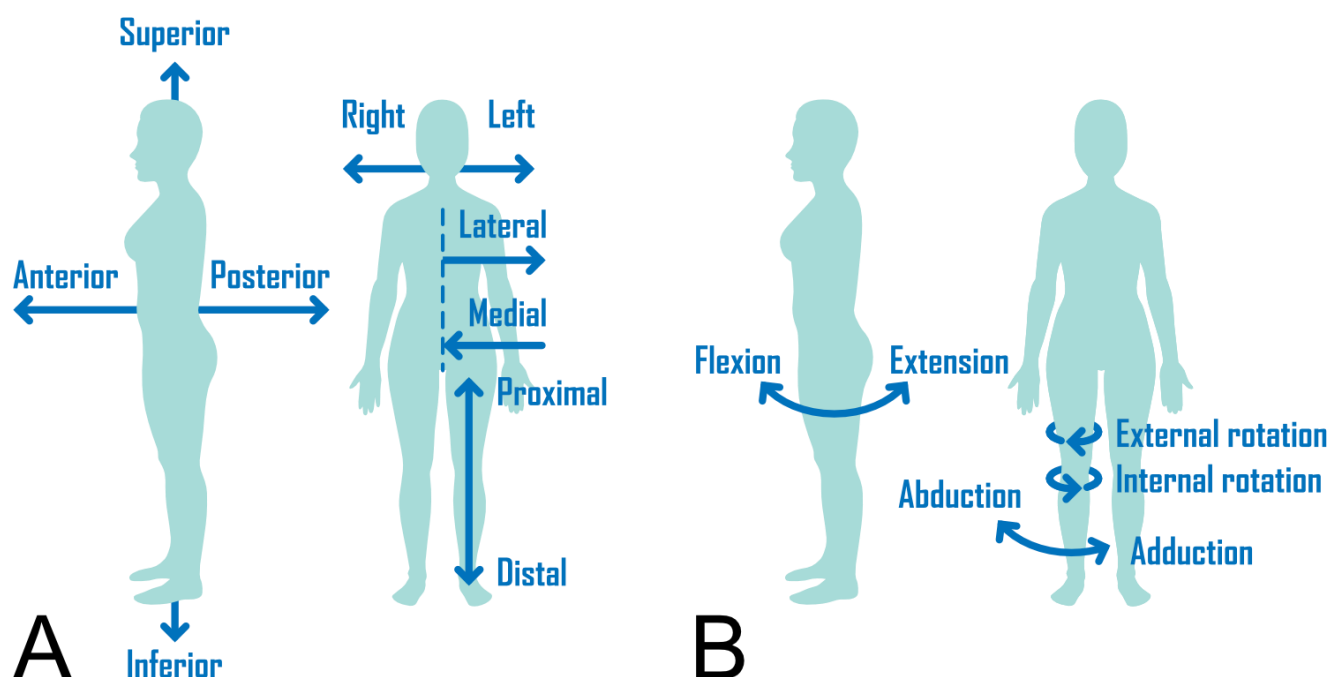


Figure 1A: Anatomical directions. 1B: Hip movements.

A.1.1 The hip

The hip joint is a ball-and-socket joint, meaning that the round protrusion of one bone moves within a cup-shaped depression of another bone. Figure 2A shows the bones of the pelvic region and upper leg. Each hip bone consists of three bones fused during childhood. The acetabulum, the socket of the hip joint, is formed of a combination of these three bones [1]. The femoral head forms the ball of the hip joint. The shortest distance between the centre of rotation of the femoral head and the femoral axis is called the femoral offset (Figure 2B).

Apart from its shape, the hip joint is provided stability by the tension in its internal and surrounding soft tissues. As mentioned in the introduction, ligaments, tendons, and muscles are the main contributors to this soft tissue tension. Other examples of soft tissues are fascia, nerves, fats, synovial membranes, and blood vessels [2].

The femoral head and acetabulum are enclosed and held together by an articular capsule (Figure 2B). Within this capsule, the bones are lined by cartilage and separated by a lubricating fluid. An additional ring of cartilage increases the depth of the acetabulum and decreases the width at its opening. Three external ligaments further reinforce the joint. A fourth ligament located inside the capsule does not aid with stability [1].

Many muscles contribute to hip stability and motion. Figure 3 shows the location of the muscles mentioned in the following sections of this thesis.

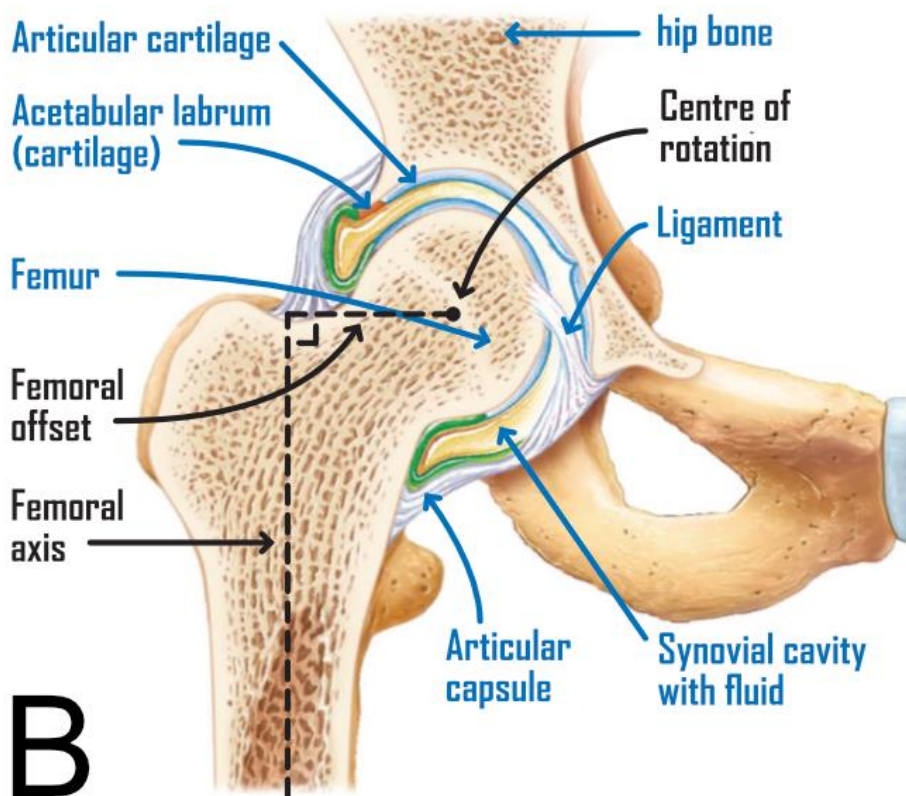
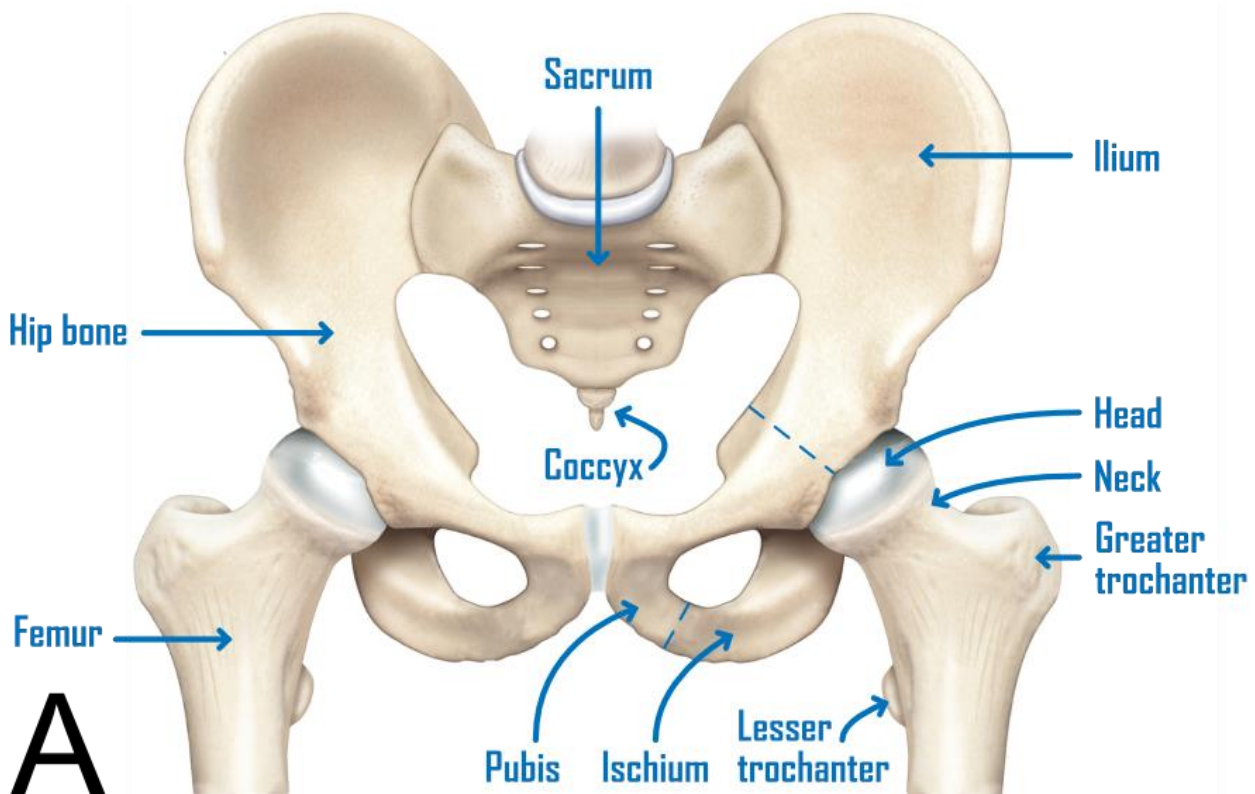
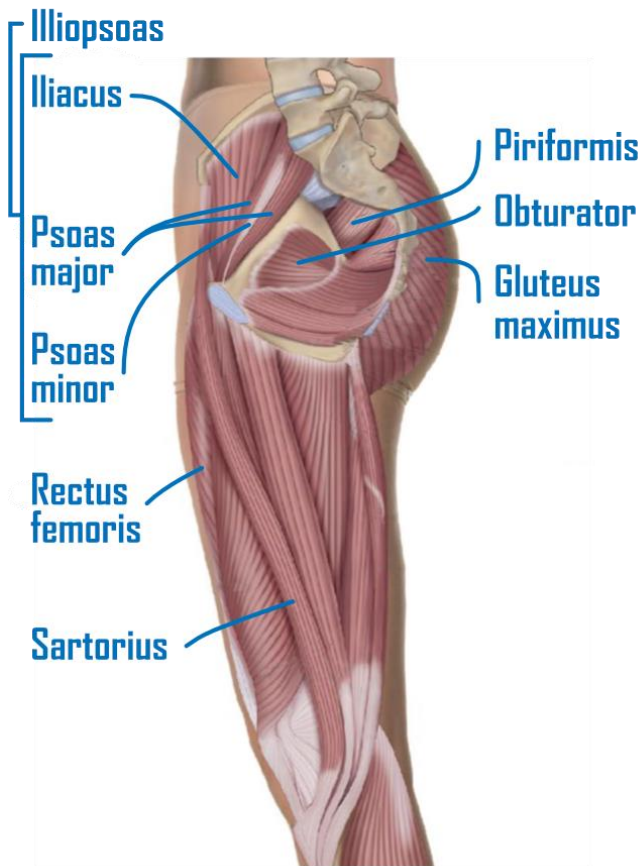
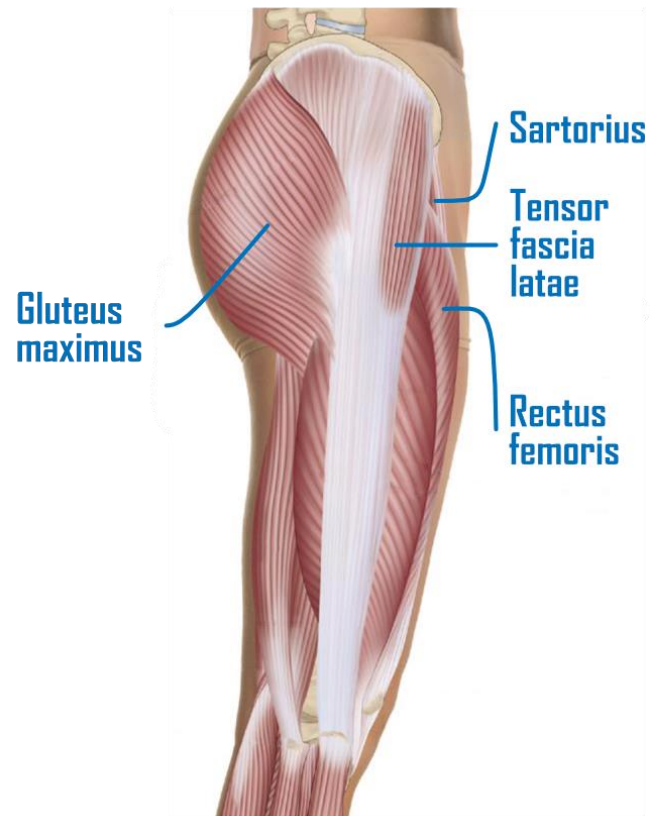


Figure 2A: Anterior view of the bones of the pelvic region. Adapted from [3]. B: Anterior view of the cross-sectioned the hip joint. External ligaments surround the articular capsule. Adapted from [1].

Right hip, medial view



Right hip, lateral view



Deep posterior view

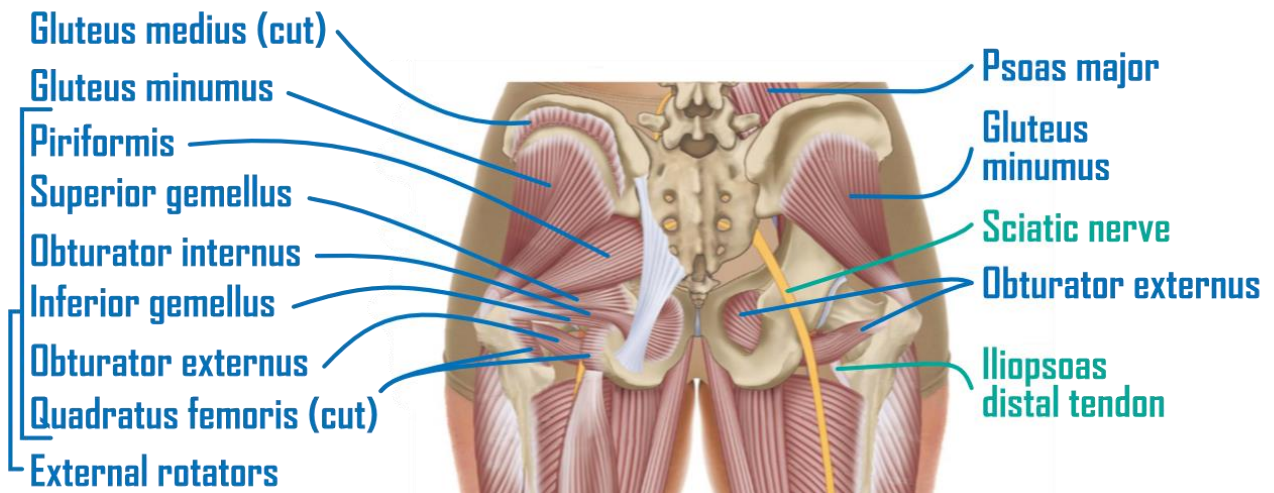


Figure 3: The muscles of the pelvis (mentioned in this thesis). Adapted from [4].

A.2 Hip implant components

A hip implant replaces the acetabulum and upper region of the femur. Figure 4A shows the Corail Pinnacle hip implant. The cup and liner are implanted into the acetabulum of the hip bone to form the artificial hip socket. The stem is inserted into the femur and the head replaces the function of the removed femoral head. Both the cup and the stem are produced out of titanium and provide optimal bone attachment. The liner and head form the articular surfaces of the prosthesis. They are produced out of ceramics and/or polyethylene to reduce wear debris generated by friction [5]. The implant is available in varying lengths, angles, and offsets. During surgery, the surgeon uses a trial implant (Figure 4B) to determine the final values of these variables. The stem of the trial implant is modular. In this research, we work with three different neck geometries: standard (STD), increased lateral offset (high offset - KHO), and reduced angle between neck and shaft (coxa vara – KLA). More than twenty head variations are available [2]. In this research we use three, heads with offsets of +1, +5 and +9 mm. The depth of the cavity in the head determines the neck length and thus the femoral offset.

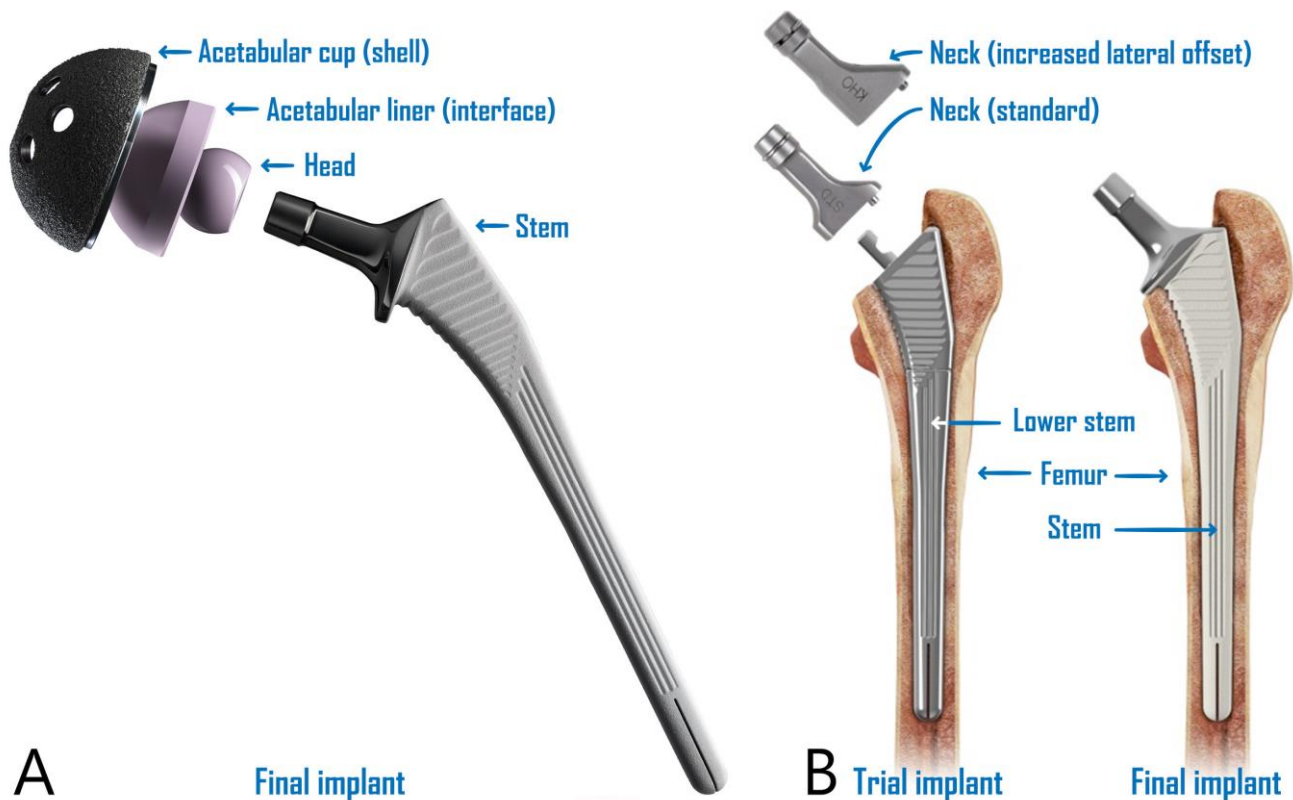


Figure 4. A: Exploded view of the Corail Pinnacle Hip implant. Adapted from [6] on 04-08-2020. B: The trial implant (left) and the final implant (right). Adapted from [7] on 04-08-2020.

A.3 Reasons for primary THA

Doctors may recommend THA for patients who experience hip stiffness or pain so severe that it limits everyday activities and which cannot be relieved adequately with pain relieve medication, physical therapy or walking supports [8]. Patients who have undergone THA reported pain and difficulties performing activities of daily life such as walking, taking the stairs and putting on shoes as the most important reasons for wanting the surgery [9]. The vast majority (72%) of THAs is performed after a diagnosis of primary osteoarthritis – osteoarthritis of no other known aetiology [10]. Other aetiologies leading to surgery are hip dysplasia (11%), avascular necrosis (10%), post-traumatic arthritis (4%), and inflammatory arthropathy (2%).

A.4 The primary THA procedure

This section gives a general overview of the THA procedure, including pre-operative planning.

A.4.1 Pre-operative planning

Prior to the surgery, the patient undergoes a clinical examination, and the hip joint is imaged using X-rays or a CT-scan [11]. The surgeon makes a surgical plan, which includes the surgical approach, anaesthesia type, implant type (materials, geometry, fixation method), and implant placement and orientation.

A.4.2 The surgery

The patient is positioned, and anaesthesia is administered. Then, the surgeon incises and displaces overlying tissues to gain access to the hip joint [12]. After dislocating the joint, the femoral head and neck are removed using a saw.

Placing the acetabular cup

The acetabulum is reshaped with a reamer to restore its original centre of rotation and to fit the acetabular cup [13]. A trial cup can be used to test placement and orientation. The final cup is fixated by a press fit, screws, spikes, or cement. The liner is pressed into the cup.

Placing the femoral stem

A cavity is created in the shaft of the femur by consecutively inserting broaches of increasing sizes using a hammer. In case of the Corail implant, the largest broach is the stem of the trial implant. A trial neck and head are attached [14]. The surgeon rejoins the hip and assesses stability, leg length, range of motion, and component position. The surgeon can adjust the leg length and offset by switching to different trial neck and head configurations. According to Dr. B.J. Blaauw, the trial head is switched approximately twice during surgery, but changing the neck is unusual [2]. Once the appropriate configuration is found, the surgeon dislocates the hip, removes the trial implant, and inserts the final stem. The stem is fixated by a press fit or cement. The head is attached to the stem.

After rejoining the hip, the surgeon carefully sutures the incised tissues. The skin can be closed using staples, sutures and/or glue. The wound is covered with a sterile dressing [11].

A.5 Risks associated with THA for revision surgery

Despite the general success of THA, the procedure or implant can fail. Possible complications include implant loosening, infection, and instability. Table 1 lists the percentage of THA revision surgeries executed due to instability, as reported in six sources. To correct the complications, the surgeon can replace the prosthesis or part thereof during a revision surgery. This surgery is more technically challenging than primary THA [15] and its success rate is much lower. Patients who underwent revision surgery required further revision five times more often than patients who underwent a primary THA [16]. Revision THA is associated with higher costs and greater risk to the patient due to longer length of hospital stay and greater duration of the operation.

The risk factors identified for revision surgery are discussed in the next sections.

A.5.1 The surgery

The identified risk factors introduced by the surgery are the surgeon's experience, the surgical approach, the implant placement, and the achieved soft tissue tension.

The surgeon's experience

The success of the surgery is dependent on the experience of the surgeon. The work of inexperienced surgeons has twice as many dislocations registered as the work of more experienced surgeons. [17]. Ravi et al. (2014) found that patients of surgeons who perform less than 35 procedures per year suffered an increased risk of dislocation and early revision. Furthermore, a positive relation has been found between the duration of the procedure and the number of complications [19]. The average operation time decreases as the surgeon gains more experience.

Table 1: Percentage of THA revision surgeries executed due to instability, based on retrospective reviews.

Study authors, year, and study group	All revisions		Early revisions (<5 yr.)	
	Total (n)	Due to instability	Total	Due to instability
Kelmer et al., 2021 [20] <i>Revisions at an institution in the USA, between January 2010 and May 2019</i>	444	65 (14.6%)	136	25 (18.4%) (<2 yr.)
Burke et al., 2018 [21] <i>Revision patients under 50 years old at an institution in Ireland, between 2008 and 2013.</i>	146	14 (9.6%)	71	11 (15.5%)
Liu et al., 2016 [22] <i>Revision patients at an institution in Taiwan, between 2000 and 2012.</i>	402	25 (6.2%)	117	20 (17.1%)
Melvin et al., 2014 [23] <i>Revision patients at an institution in the USA, between 2001 and 2011.</i>	-	-	282	54 (19.1%)
Bozic et al., 2009 [24] <i>Revision patients in the USA, between October 2005 and December 2006.</i>	51,345	11,560 (22.5%)	-	-
Ulrich, Seyler, Bennett, Delanois, & Saleh, 2008 [25] <i>Revision patients who have undergone THA at two institutions in the USA, between 1996 and 2004.</i>	237	40 (16.9%)	118	39 (33%)

The surgical approach

The hip joint can be accessed from different directions (see Figure 5) and the risks differ per direction. The three most used approaches are posterior (45%), direct lateral (42%), and direct anterior (10%) [26].

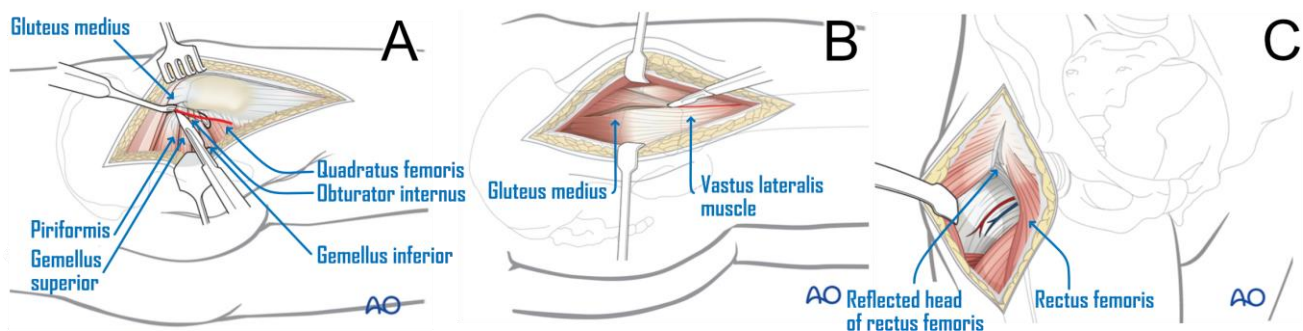


Figure 5: Surgical approaches. A: Posterior approach. Adapted from [27]. B: Lateral approach. Adapted from [28]. C: Anterior approach. Adapted from [29].

Posterior approach

During the posterior approach, the gluteus maximus and its overlying connective tissue are split to gain access to the short external rotators [12]. The tendons connecting these muscles to the greater trochanter are cut to gain access to the posterior joint capsule (see Figure 5A). This approach has an increased incidence of dislocation compared to the anterior approach [30].

Direct lateral approach

The skin and connective tissue overlying the interval between the tensor fascia lata (TFL) and the gluteus maximus is incised (see Figure 5B). The gluteus medius muscle and tendon are split to gain access to the hip capsule. This approach has a low reported dislocation rate but has an increased risk of weakened abductor muscles compared to the posterior approach [12].

Direct anterior approach

After incising the skin, the lateral femoral cutaneous nerve is transposed and the connective tissue overlying the TFL is incised. No muscles are cut during this approach. Instead, the TFL, sartorius, rectus femoris, and gluteus medius muscles are transposed using retractors to expose the anterior joint capsule (see Figure 5C). This approach offers limited femoral exposure, which can complicate achieving proper implant placement [12]. The incidence of femoral loosening is higher with this approach than with the posterior approach [30].

Revision risks due to surgical approach

While Angerame et al. (2018) found no statistical difference in overall revision rates between the anterior and posterior approach, Pincus et al. (2020) found a small increased risk of major complications associated with the anterior approach compared to the posterior and lateral approaches.

Implant placement

Improper implant positioning, especially of the acetabular cup, increases the risk of dislocation [32]–[34]. It can lead to impingement or an inadequate contact area between the articular surfaces [34].

Soft tissue tension

Insufficient soft tissue tension increases the risk of instability and dislocation [33], [34]. The surgeon can increase soft tissue tension by increasing the leg length, increasing the femoral offset and by repairing incised tissues. In Fackler and Poss' (1980) research, the average reduction of hip offset in patients suffering from dislocations was considerably larger than in the control group (5.2 mm and 0.02 mm respectively).

This thesis proposes a mechanism to provide the surgeon with real-time information to ensure optimal soft-tissue tension and thus to reduce the risk of revision.

A.5.2 The Implant

The implant materials, head size, fixation method and modularity were found to influence the revision risk.

Materials

Hip implants with metal-on-metal (MoM) articular surfaces result in significantly higher revision rates than other implants [32]. In Melvin et al.'s (2014) retrospective review into early revisions, 38 of 39 metallosis cases and two-third of the aseptic acetabular loosening cases involved an all-metal cup. Crosslinked polyethylene (XLPE) shows an increased wear resistance compared to the traditionally used polyethylene [32].

Head size

An increased head-to-neck ratio decreases the chance of dislocation [32]. Head sizes of 28 mm or smaller result in a higher risk of revision due to dislocation than head sizes of 36 mm or larger. However, metal on cross-linked polyethylene (MoXLPE) implants with heads larger than 32 mm wear more quickly than MoXLPE implants with smaller heads. This same effect is not observed in ceramic on XLPE implants [36].

Fixation method

The survival rates of uncemented hip implants were significantly higher than that of cemented hip implants in a 20-year follow up study [37].

Modularity

Femoral stems with a separate neck are revised twice as often as femoral stems with a fixed neck. These modular stems have a higher chance of loosening, dislocation and fracture [32].

A.5.3 The patient

The patient introduces many risk factors for revision, a number of which can be influenced prior to the surgery. These include a BMI > 40, anaemia, diabetes mellitus, vitamin D deficiency, tobacco or opioid use, and malnutrition. Optimizing these risk factors to recommended values before surgery could improve recovery rates [38], [39]. Bernstein et al. (2018) found that including preoperative optimization yielded similar patient outcomes at lower healthcare costs. Patients who received preoperative education and/or who underwent preoperative exercise had significantly less postoperative pain and significantly improved postoperative function than the control group [41].

Young age is an obvious risk factor. Implants have a lifespan of ~10-20 years, and thus, younger patients are more likely to require a revision. However, after adjusting for mortality, younger patients are still at higher risk for aseptic loosening and infection [15], [39]. Contrarily, older patients are at increased risk of dislocation [33].

Other risk factors include pre-operative diagnoses of hypothyroidism, depression, anxiety, liver disease, COPD, and fluid/electrolyte disorders [15], [32]. Dementia and neuromuscular diseases such as cerebral palsy and Parkinson's increase the risk of dislocation [33]. Primary diagnoses of polyarthritis, rheumatoid arthritis, a fractured neck of the femur, and osteonecrosis also increase the risk. Additionally, multiple previous emergency hospitalisations and the male gender were both identified as important risk factors [15], [32]. A high activity level increases the risk of aseptic loosening [32]. Previous hip surgeries, prior fractures, the female gender, and failure to comply to movement restrictions all increase the chance of dislocation [32], [33].

A.6 Achieving accurate soft tissue tension

Achieving adequate soft tissue tension is closely related to equalising leg lengths and restoring femoral offset [42]. This section lists relevant techniques and tools.

A.6.1 Preoperative templating using X-rays or CT-scans

Imaging techniques help determine variables such as leg length discrepancies (Figure 6A), the femoral offset and angle, and the predicted level of the neck cut. Based on the imagery, the surgeon can anticipate the required implant type, implant orientation, and possible intraoperative difficulties [43]. However, these techniques cannot show the full picture. They only visualise the hip in a static state and X-rays provide only a 2D view.

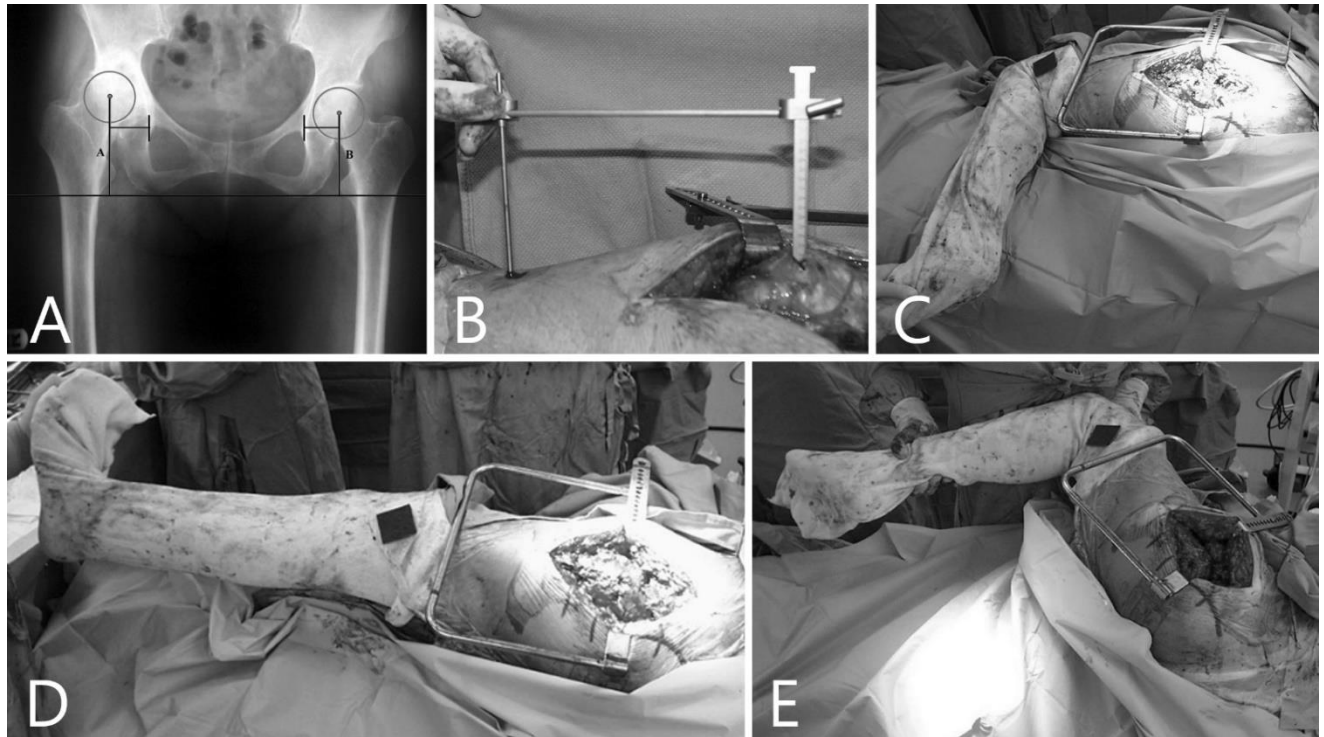


Figure 6. A: Preoperative X-ray to assess leg length discrepancy. B: A jig used to measure leg length and femoral offset. C: The dropkick test. D&E: Stability assessment tests. Figure belongs to [44].

A.6.2 Implants allowing for intraoperative leg-length and offset restoration

Implants available in varying offsets, angles, and lengths allow the surgeon to make final adjustments during surgery. Trial implants are inserted into the hip during surgery to mimic the function of the final prosthetic [42].

A.6.3 Intraoperative leg-length and offset measurement

The distance between two fixed points of the affected hip can be measured using a jig (Figure 6B). Measurements before hip dislocation and after insertion of the trial implants can be compared. Additionally, the contralateral knee and foot can be palpated to compare limb lengths [42]. The distance between the femur and the pelvic bone can be palpated to determine the femoral offset [45]. A finger width or more is required between the hip bone and the greater trochanter when the leg is abducted and externally rotated. The same minimal distance is advised between the hip bone and the lesser trochanter when the leg is extended and externally rotated.

A.6.4 Intraoperative soft tissue tension assessment

Several tests are available to the surgeon, including the shuck, the drop-kick, and stability tests. The femoral offset and leg length can be adjusted if the tension is found inadequate.

During the shuck test traction is applied to the leg in an inferior direction. The surgeon can assess the soft tissue tension in the joint by noting the level of distraction in the joint [44]. Sources report differing guidelines as to how far the joint should disengage [2]. The use of spinal anaesthesia renders this test unreliable, as this is associated with lowered soft tissue tension [46].

During the drop-kick test the hip is extended and the knee is flexed to a 90° angle (Figure 6C). Both the knee resisting bending or promptly extending when released are signs of increased soft tissue tension. The leg length should be reduced [44].

During the stability tests the hip is assessed for impingement, range of motion, and instability in two positions. The first position has the leg extended and under maximal external rotation, the second has both the hip and the knee flexed to 90° with the leg under maximal internal rotation (Figure 6D&E) [44].

The effectiveness of these techniques is reliant on the experience of the surgeon since all of them are based on subjective measurements.

A.6.5 Release or sequential cutting of muscles and tendons

Tight muscles or tendons can cause soft tissue imbalance, pain, and can restrict range of motion [45]. Restricted hip extension can be counteracted by removing the anterior capsule or elongating the iliopsoas tendon by sequential cutting. The TFL can be released to correct limited adduction and limited abduction combined with external rotation. The rectus femoris can be released to achieve proper knee flexion.

A.7 Quantifying soft tissue tension

An objective soft tissue tension assessment technique could aid surgeons in establishing proper tension. Such a technique could be especially helpful for inexperienced surgeons, who have not yet mastered the required skill and intuition. Regrettably, the literature on objective soft tissue tension assessment is sparse. The next sections discuss quantified soft tissue tension, variables affecting this tension, and current soft tissue tension assessment devices.

A.7.1 Quantified soft tissue tension and relevant variables

The soft tissue tension in the hip differs between patients and can change over time. Schwachmeyer et al. (2013) found in a post-operative study that the soft tissue tension in the hip of active patients was significantly higher during isometric exercises than in patients with a passive lifestyle. The soft tissue tension was also found to be dependent on anthropometric variables such as leg length, segment masses, and muscle lever arms. This research was based on data gathered with the hip III implant, which is further discussed in section A.7.2. The isometric exercise datasets included force data measured in the hips of five patients lying face up in a relaxed state (Table 2). Due to the small sample size, these values only give an indication of the hip force distribution in two different hip and knee positions. In both positions, the bulk of the force acts along the axis of the implant neck and a considerable normal force acts in the posteroinferior direction.

Table 2: The mean minimal hip forces measured in patients who were lying face up and relaxing their hip muscles. The original axes were directed laterally (x), anteriorly (y), and superiorly (z). The implant neck was positioned in an 45° angle in the xz -plane. Data has been extracted from isometric exercise datasets in the Orthoload database (See appendix **Error! Reference source not found.**). The force was divided into components along and normal to the axis of the neck (F_{ax} and F_n). The normal force acts along angle α , which is 0 in the most inferior direction and increases in the anterior direction.

	Relaxed hip force (N)						
	$F_{res} \pm \sigma$	$F_x \pm \sigma$	$F_y \pm \sigma$	$F_z \pm \sigma$	$F_{ax} \pm \sigma$	$F_n \pm \sigma$	$\alpha \pm \sigma$ ($^\circ$)
Extended knee and hip	260 ± 82	137 ± 63	-40 ± 30	-211 ± 70	246 ± 80	80 ± 35	-38 ± 36
Flexed knee and hip	266 ± 74	139 ± 57	-14 ± 28	-221 ± 62	255 ± 72	70 ± 34	-15 ± 41

Intra-operative soft tissue tension

The soft tissue tension is lower during THA. According to Dr. B.J. Blaauw, expects the hip forces to range between $50 - 120 N$, with peak maxima of $200 N$ (Zhang, 2020). The main force component acts along the axis of the implant neck. The intra-operative soft-tissue tension depends on surgical approach, anaesthesia, and the surgeon. The incision of muscles and other soft tissues lowers tension, and the surgical approach determines which tissues are cut. Spinal anaesthesia and neuromuscular blocking agents relax the skeletal muscles, which further lowers tension [2], [46]. The surgeon introduces slight inaccuracies and variations in protocol, which can also affect soft-tissue tension [2]. Examples of this include specific placement and length of incisions and the force the surgeon applies when dislocating the hip.

Quantified intra-operative soft tissue tension assessment

It might be possible to develop an intra-operative test which provides the surgeon with a quantified joint force *safe zone* [2]. This *safe zone* could be a force range, direction, or pattern and could take most earlier mentioned variables into account. Perhaps such a *safe zone* can be found for the current soft tissue

assessments. Further research is needed to develop this test and to investigate the validity of a joint force *safe zone* in preventing soft-tissue imbalance.

A.7.2 Current soft tissue tension assessment devices

There are few devices that are designed to record the soft tissue tension in the hip either intra- or postoperatively. The most notable devices have been designed by the Julius Wolff Institute [48]. Their instrumented hip implants contain strain gages to assess the hip forces during daily activities and thus have a different goal than the device proposed in this thesis. The *Hip III* measures 6DOF – three forces and three moments. The device also contains a coil for power supply, a transmitter and an antenna (Figure 7A). This device has been implanted into ten patients [49]. The results of the tests performed with their devices can be found in the Orthoload database [50]. As these implants are permanent and remain in the patients after surgery, they must adhere to much stricter requirements than instrumented trial implants. The implant must be able to withstand the forces on the hip for several decades, and more equipment must be integrated to allow for wireless communication and power supply. All these restrictions are associated with higher costs. Strain gages could also be utilised in a trial implant. They are small and are suitable for the expected force range. Zhang’s design, discussed later in this section, also uses strain gages. However, the glues for strain gages in medical applications which are available in Europe are unsuitable for repeated sterilization in the Autoclave [2].

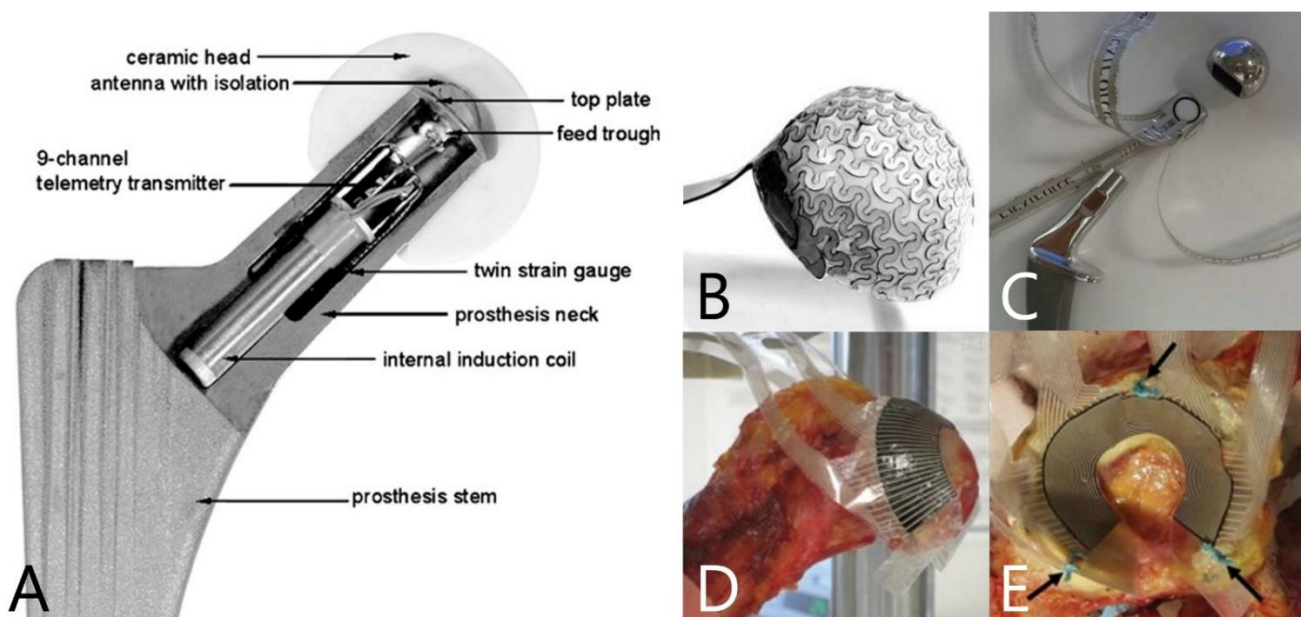


Figure 7: Current hip joint soft tissue assessment devices. A: Instrumented hip implant using strain gages [48]. B: Instrumented prosthetic cup insert consisting of folded capacitive sensors [51]. C: Instrumented hip implant using four piezoresistive force sensors [52]. D&E: Sensor consisting of radial and concentric arrays of transducers [53].

Müller et al. (2004) designed a prosthetic cup with an inlay of folded capacitive sensor arrays (Figure 7B) to assess pressure distribution in joints. It is unclear whether they aim for intra- or postoperative measurements. This design was measured *in vitro* to gather proof of principle. The principle works; however, the spatial resolution was poor. The pressure distribution is visualised in a coloured grid, in which the colours indicate the amount of pressure. The researchers noted that the sensors at the time of the research were too large for this kind of measurement. The sensor array changes the articular surface of the cup from a smooth curve to a multitude of flat surfaces. This might impede joint movement and influence the pressure distribution. Measuring pressure distribution requires a high number of sensors and gives a high number of output values, which in my opinion is unnecessarily convoluted. The articular surfaces of the implant are smooth, spherical, and similarly sized, which should result in a predictable pressure distribution pattern: concentric, with the peak pressure along the axis of the resultant force. This pressure distribution should not be able to give any additional valuable information to what can be gained from force measurement. Furthermore, presenting the pressure in such a fractured manner impedes making quantified comparisons. Biocompatibility was not considered yet.

Tanino et al. (n.d.) have designed an instrumented hip implant using four piezoresistive force sensors to assess the hip forces intraoperatively (Figure 7C). Three sensors, one for each axis, were mounted on a cube which

was inserted into a modified prosthetic head. The implant was tested in four patients. The accuracy, sensitivity and sample frequency were not reported in the source and no additional sources could be found. It is unclear how the sensors are connected to the implant and whether they were installed in a preloaded state. Furthermore, the source did not mention how the researchers account for the considerable drift, hysteresis, and sensor-to-sensor variation of the chosen sensor type ($< 5\%$ per logarithmic time scale, $< 4.5\%$ of full scale, and $\pm 40\%$ respectively; Tekscan, 2016).

Rudert et al. (2014) have developed a sensor which can measure dynamic contact stresses up to 20 MPa in hip-joints of cadavers (Figure 7D&E). The sensor is shaped like a 150° partial ring and consists of two layers of grid-array transducers separated by piezoresistive ink. The inner layer of transducers is arranged concentrically, the outer layer radially. A cadaver test was performed to compare the force output of the sensor to that of pressure sensitive film. The outputs varied less than $\pm 10\%$ during static loading and $\pm 26\%$ during dynamic loading. This device only measures the pressures on a limited area of the femoral head, which excludes areas such as the space around the axis of the femoral neck and the inferior part of the head. Both are high force-bearing areas in hip implants. Furthermore, this measurement method might be unsuitable for use in a hip implant due to the higher curvature of the implant head. The current design already tends to wrinkle due to the curvature of the femoral head.

Earlier designs in the StemForce project

Two devices for the assessment of soft tissue tension during total hip arthroplasty were designed in earlier research by the StemForce research group.

Van der Pol's design [2] (Figure 8A) is incorporated in the neck component of the Corail trial implant and can measure axial forces. This design consists of two concentric cylinders which act as an axial sliding bearing. The inner cylinder is connected to the base of the neck. A hall sensor is incorporated into the cylinder's top surface. The outer cylinder is connected to the head and a magnet is attached to the base of the cylinder's top surface. A rubber ring acts as a spring between the two surfaces. Lubrication was applied between the two cylinders to minimise friction. The sensor measures magnetic field. If force is applied axially to the head, the spring will compress, and the distance between the magnet and the sensor will decrease. This changes the magnetic field around the sensor and thus the sensor's output. A microprocessor can calculate the applied force based on the change of output. This device theoretically has a resolution of lower than 5 N when measuring forces below 130 N . The device encountered two so far unresolved issues: elastic hysteresis in the rubber spring and friction of the sliding bearing. Furthermore, the design only gives limited insight in the soft tissue tension, as it solely measures axial force. It disregards the normal force component and thus cannot determine the magnitude and direction of the resultant force.

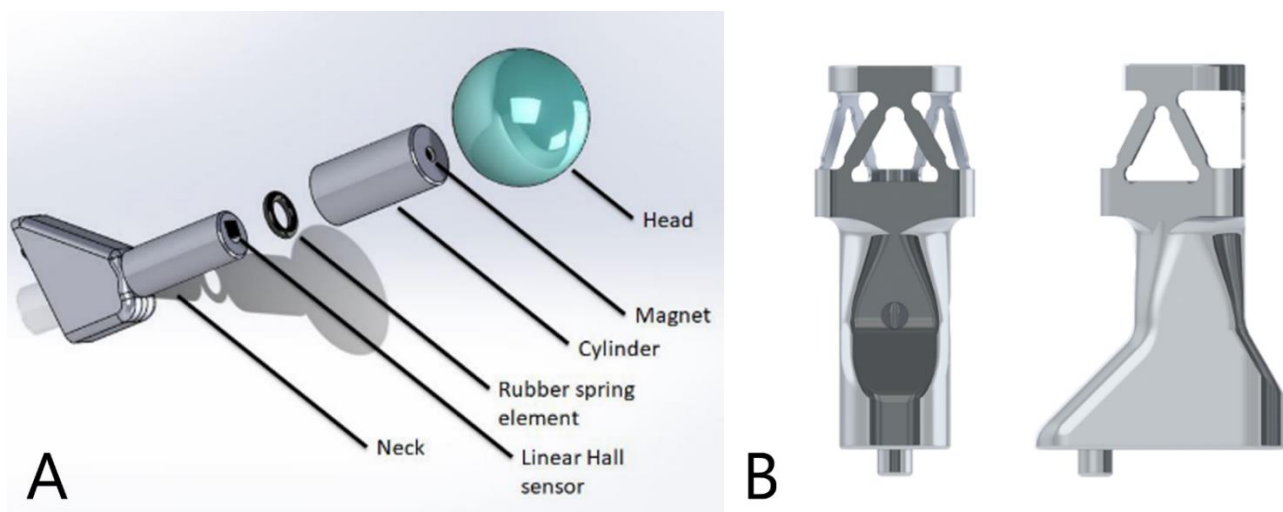


Figure 8: Stemforce devices for soft tissue tension assessment during total hip arthroplasty. A: Device measuring 1DOF, using hall sensors [2]. B: Device measuring 3DOF, using strain gages [55].

Zhang's design [55] (Figure 8B) is also incorporated into the neck component of the Corail trial implant. This design measures forces along three axes using strain gages and a steward platform. Axial compression tests

using a large-scale prototype showed good repeatability ($0.997 \leq R2 \leq 0.9999$ of measurement data to the regression line) and high accuracy ($NRMSE = 97.77\%$) under loads of up to around 300 N [55]. A follow up test along the x-, y-, and z-axis showed a resolution better than 1 N for compressive loads up to 150 N. This design has only been tested in larger geometry due to cost constraints. It requires many sensors and wires which would be difficult to connect in a scaled down version. Biocompatibility and sterilisation were not considered yet in this design. As with the HIP III, the glue of the strain gages might limit the designs suitability for sterilization.

A.8 Summary

THA is an effective procedure to treat severe hip pain and stiffness. Complications can be addressed in revision surgery by replacing part of or the whole hip implant. The incidence of THA is increasing rapidly and this is expected to complicate health care budgets. A disproportionate amount of the rise in cost will be caused by revision surgery.

Inadequate soft tissue tension increases the risk for hip instability and revision surgery. All current soft tissue tension assessment methods are based on subjective measurements and thus their effectiveness is reliant on the experience of the surgeon. Surgeon inexperience increases the risk for early revision and doubles the risk for dislocation. An objective assessment technique could aid surgeons in establishing proper tissue tension.

The StemForce project develops objective intraoperative testing tools, intended to be used predominantly by inexperienced surgeons to reduce the number of hip implant failures due to inadequate soft tissue tension. The 3DOF hip is part of the StemForce project. It is a novel force measurement mechanism which senses hip joint forces in three degrees of freedom. This thesis aims to validate, characterise, and optimise the 3DOF hip.

A.9 References

- [1] E. N. Marieb and K. Hoehn, *Human Anatomy & Physiology*, 10th ed. Harlow, Essex, United Kingdom: Pearson Education Limited, 2015.
- [2] D. Van der Pol, "Assessment of soft tissue tension during total hip arthroplasty." MSc Thesis, Dept. of Biomed. Eng., Techn. Univ. of Delft, Delft, 2017.
- [3] "Pelvis," *Encyclopaedia Britannica*. <https://www.britannica.com/science/pelvis> (accessed May 24, 2021).
- [4] "Muscles of the Pelvis and Thigh," *Musculoskeletal Key*. <https://musculoskeletalkey.com/10-muscles-of-the-pelvis-and-thigh/> (accessed May 21, 2021).
- [5] A. Jahan, K. L. Edwards, and M. Bahraminasab, "Total hip prostheses," in *Multi-criteria Decision Analysis for Supporting the Selection of Engineering Materials in Product Design*, 2nd ed. Oxford: Butterworth-Heinemann, 2016, pp. 147–225. doi: 10.1097/00003086-197009000-00008.
- [6] "Health economics," *CorailPinnacle*. <https://www.corailpinnacle.net/value-solutions/health-economics> (accessed Aug. 04, 2020).
- [7] "CORAIL® Revision," *Corail Pinnacle*. <https://www.corailpinnacle.net/corail/revision> (accessed Aug. 04, 2020).
- [8] J. R. H. Foran, "Total Hip Replacement," *OrthoInfo*, 2020. <https://orthoinfo.aaos.org/en/treatment/total-hip-replacement/> (accessed Apr. 22, 2021).
- [9] J. G. Wright, S. Rudicel, and A. R. Feinstein, "Ask Patients what They Want: Evaluation of Individual Complaints before Total Hip Replacement," *Journal of Bone and Joint Surgery*, vol. 76, no. 2, pp. 229–234, 1994.

- [10] V. K. Aggarwal, Y. M. Suh, L. Hutzler, L. Moscona, and P. Castañeda, "Total hip arthroplasty for secondary causes of arthritis an increase in time and money," *Bull Hosp Joint Dis*, vol. 77, no. 4, pp. 233–237, 2019.
- [11] M. Varacallo, T. D. Luo, and N. Johanson, "Total Hip Arthroplasty Techniques," *StatPearls*, 2020. https://www.statpearls.com/ArticleLibrary/viewarticle/22894#ref_20452180 (accessed Apr. 29, 2021).
- [12] S. Petis, J. L. Howard, B. L. Lanting, and E. M. Vasarhelyi, "Surgical approach in primary total hip arthroplasty: anatomy, technique and clinical outcomes," *Canadian Journal of Surgery*, vol. 58, no. 2, pp. 128–139, 2015, doi: 10.1503/cjs.007214.
- [13] "DePuy Synthes Pinnacle Surgical technique," *DePuy Synthes*. 2014. doi: 10.1016/j.neucli.2017.11.008.
- [14] "Corail Hip System Surgical Technique," *DePuy Synthes*. 2017. doi: 10.1017/S0890060408000218.
- [15] A. Bottle, S. P. Id, P. Aylin, and M. Loeffler, "Risk factors for early revision after total hip and knee arthroplasty: National observational study from a surgeon and population perspective," *PLoS One*, vol. 14, no. 4, pp. 1–15, 2019, doi: 10.1371/journal.pone.0214855.
- [16] K. L. Ong, E. Lau, J. Suggs, S. M. Kurtz, and M. T. Manley, "Risk of subsequent revision after primary and revision total joint arthroplasty," *Clin Orthop Relat Res*, vol. 468, no. 11, pp. 3070–3076, 2010, doi: 10.1007/s11999-010-1399-0.
- [17] U. Hedlundh, L. Ahnfelt, C.-H. Hybbinette, J. Weckstrom, and H. Fredin, "Surgical Experience Related to Dislocations after Total Hip Arthroplasty," *Journal of Bone and Joint Surgery*, vol. 78, no. 2, pp. 206–209, 1996.
- [18] B. Ravi *et al.*, "Relation between surgeon volume and risk of complications after total hip arthroplasty: Propensity score matched cohort study," *BMJ*, vol. 348:g3284, 2014, doi: 10.1136/bmj.g3284.
- [19] K. Zenk, S. Finze, D. Kluess, R. Bader, J. Malzahn, and W. Mittelmeier, "Einfluss der Erfahrung des Operateurs in der Hüftendoprothetik: Abhängigkeit von Operationsdauer und Komplikationsrisiko," *Orthopade*, vol. 43, no. 6, pp. 522–528, 2014, doi: 10.1007/s00132-014-2292-4.
- [20] G. Kelmer, A. H. Stone, J. Turcotte, and P. J. King, "Reasons for Revision: Primary Total Hip Arthroplasty Mechanisms of Failure," *J Am Acad Orthop Surg*, vol. 29, no. 2, pp. 78–87, 2021, doi: 10.5435/JAAOS-D-19-00860.
- [21] N. G. Burke, J. P. Gibbons, A. J. Cassar-Gheiti, F. M. Walsh, and J. P. Cashman, "Total hip replacement — the cause of failure in patients under 50 years old?," *Ir J Med Sci*, vol. 188, no. 3, pp. 879–883, 2019, doi: 10.1007/s11845-018-01956-8.
- [22] K. Liu, W. Wu, and J. Wang, "When and how do prosthetic hips fail after total hip arthroplasties? - A retrospective study," *Journal of the Formosan Medical Association*, vol. 115, no. 9, pp. 786–793, 2016, doi: 10.1016/j.jfma.2015.07.014.
- [23] J. S. Melvin, T. Karthikeyan, R. Cope, and T. K. Fehring, "Early Failures in Total Hip Arthroplasty — A Changing Paradigm," *Journal of Arthroplasty*, vol. 29, no. 6, pp. 1285–1288, 2014, doi: 10.1016/j.arth.2013.12.024.
- [24] K. J. Bozic, S. M. Kurtz, E. Lau, K. Ong, T. P. Vail, and D. J. Berry, "The Epidemiology of Revision Total Hip Arthroplasty in the United States," *J Bone Joint Surg*, vol. 91, no. 1, pp. 128–133, 2009, doi: 10.2106/JBJS.H.00155.

- [25] S. D. Ulrich, T. M. Seyler, D. Bennett, R. E. Delanois, and K. J. Saleh, "Total hip arthroplasties: What are the reasons for revision?," *Int Orthop*, vol. 32, no. 5, pp. 597–604, 2008, doi: 10.1007/s00264-007-0364-3.
- [26] O. Chechik, M. Khashan, R. Lador, M. Salai, and E. Amar, "Surgical approach and prosthesis fixation in hip arthroplasty world wide," *Arch Orthop Trauma Surg*, vol. 113, pp. 1595–1600, 2013, doi: 10.1007/s00402-013-1828-0.
- [27] "Posterolateral approach," *AO Surgery Reference*. <https://surgeryreference.aofoundation.org/orthopedic-trauma/periprosthetic-fractures/hip/approach/posterolateral-approach#protection-of-sciatic-nerve> (accessed Apr. 29, 2021).
- [28] "Direct lateral approach," *AO Surgery Reference*. <https://surgeryreference.aofoundation.org/orthopedic-trauma/adult-trauma/proximal-femur/approach/direct-lateral-approach#superficial-surgical-dissection> (accessed Apr. 29, 2021).
- [29] "Direct anterior approach," *AO Surgery Reference*. <https://surgeryreference.aofoundation.org/orthopedic-trauma/periprosthetic-fractures/hip/approach/direct-anterior-approach#table-and-positioning> (accessed Apr. 29, 2021).
- [30] M. R. Angerame, T. K. Fehring, J. L. Masonis, J. B. Mason, S. M. Odum, and B. D. Springer, "Early Failure of Primary Total Hip Arthroplasty : Is Surgical Approach a Risk Factor ?," *J Arthroplasty*, vol. 33, no. 6, pp. 1780–1785, 2018, doi: 10.1016/j.arth.2018.01.014.
- [31] D. Pincus, R. Jenkinson, M. Paterson, T. Leroux, and B. Ravi, "Association between Surgical Approach and Major Surgical Complications in Patients Undergoing Total Hip Arthroplasty," *JAMA - Journal of the American Medical Association*, vol. 323, no. 11, pp. 1070–1076, 2020. doi: 10.1001/jama.2020.0785.
- [32] T. Karachalios, G. Komnos, and A. Koutalos, "Total hip arthroplasty: survival and modes of failure," *EFORT Open Rev*, vol. 3, no. 5, pp. 232–239, 2018, doi: 10.1302/2058-5241.3.170068.
- [33] J. Dargel, J. Oppermann, G. Brüggemann, and P. Eysel, "Dislocation Following Total Hip Replacement," *Dtsch Arztebl Int*, vol. 111, pp. 884–891, 2014, doi: 10.3238/arztebl.2014.0884.
- [34] G. Ullmark, "The unstable total hip arthroplasty," *EFORT Open Rev*, vol. 1, no. 4, pp. 83–88, 2016, doi: 10.1302/2058-5241.1.000022.
- [35] C. D. Fackler and R. Poss, "Dislocation in total hip arthroplasties," *Clin Orthop Relat Res*, vol. 151, pp. 169–178, 1980, doi: 10.1097/00003086-198009000-00023.
- [36] G. Tsikandylakis, M. Mohaddes, P. Cnudde, A. Eskelinen, J. Kärrholm, and O. Rolfson, "Head size in primary total hip arthroplasty," *EFORT Open Rev*, vol. 3, no. 5, pp. 225–231, 2018, doi: 10.1302/2058-5241.3.170061.
- [37] K. Corten, R. B. Bourne, K. D. Charron, K. Au, and C. H. Rorabeck, "Comparison of total hip arthroplasty performed with and without cement: A randomized trial," *Journal of Bone and Joint Surgery*, vol. 93, no. 14, pp. 1335–1338, 2011, doi: 10.2106/JBJS.J.00448.
- [38] R. de Steiger and C. Wall, "Pre-operative optimisation for hip and knee arthroplasty: Minimise risk and maximise recovery," *Aust J Gen Pract*, vol. 49, no. 11, pp. 710–714, 2020, doi: 10.31128/AJGP-05-20-5436.
- [39] C. Kenney, S. Dick, J. Lea, J. Liu, and N. A. Ebraheim, "A systematic review of the causes of failure of Revision Total Hip Arthroplasty," *J Orthop*, vol. 16, no. 5, pp. 393–395, 2019, doi: 10.1016/j.jor.2019.04.011.

- [40] D. N. Bernstein *et al.*, “Evaluation of a Preoperative Optimization Protocol for Primary Hip and Knee Arthroplasty Patients,” *Journal of Arthroplasty*, vol. 33, no. 12, pp. 3642–3648, 2018, doi: 10.1016/j.arth.2018.08.018.
- [41] R. Moyer, K. Ikert, K. Long, and J. Marsh, “The Value of Preoperative Exercise and Education for Patients Undergoing Total Hip and Knee Arthroplasty: A Systematic Review and Meta-Analysis,” *JBJS Rev*, vol. 5, no. 12:e2, 2017, doi: 10.2106/JBJS.RVW.17.00015.
- [42] R. B. Bourne and C. H. Rorabeck, “Soft Tissue Balancing - The Hip,” *J Arthroplasty*, vol. 17, no. 4, pp. 17–22, 2002, doi: 10.1054/arth.2002.33263.
- [43] S. Eggli, M. Pisan, and M. E. Müller, “The value of preoperative planning for total hip arthroplasty,” *Journal of Bone and Joint Surgery - Series B*, vol. 80, no. 3, pp. 382–390, 1998, doi: 10.1302/0301-620X.80B3.7764.
- [44] M. N. Charles, R. B. Bourne, J. R. Davey, A. S. Greenwald, B. F. Morrey, and R. C. H., “Soft-Tissue Balancing of the Hip,” *J Bone Joint Surg*, vol. 86, no. 5, pp. 1078–1088, 2004.
- [45] P. Kosev, B. Valentinov, Y. Andonov, and C. Sokolov, “Soft Tissue Balancing In Total Hip Arthroplasty,” *Journal of IMAB*, vol. 21, no. 1, pp. 752–756, 2015, doi: 10.5272/jimab.2015211.752.
- [46] S. S. Sathappan, D. Ginat, V. Patel, M. Walsh, W. L. Jaffe, and P. E. Di Cesare, “Effect of Anesthesia Type on Limb Length Discrepancy After Total Hip Arthroplasty,” vol. 23, no. 2, pp. 203–209, 2008, doi: 10.1016/j.arth.2007.01.022.
- [47] V. Schwachmeyer, P. Damm, A. Bender, F. Graichen, and G. Bergmann, “In Vivo Hip Joint Loading during Post-Operative Physiotherapeutic Exercises,” *PLoS One*, vol. 8, no. 10, pp. 12–14, 2013, doi: 10.1371/journal.pone.0077807.
- [48] P. Damm, F. Graichen, A. Rohlmann, A. Bender, and G. Bergmann, “Total hip joint prosthesis for in vivo measurement of forces and moments,” *Med Eng Phys*, vol. 32, pp. 95–100, 2010, doi: 10.1016/j.medengphy.2009.10.003.
- [49] P. Damm, “Hip Joint - Instrumented Implants,” *Charité Universitätsmedizin Berlin*. https://jwi.charite.de/en/research/research_organ_level_biomechanics/joint_loading_musculoskeletal_analysis/instrumented_implants/hip_joint/ (accessed Aug. 21, 2020).
- [50] “OrthoLoad,” *Johan Wolff Institut*. <https://orthoload.com/> (accessed Aug. 21, 2020).
- [51] O. Müller, W. J. Parak, M. G. Wiedemann, and F. Martini, “Three-dimensional measurements of the pressure distribution in artificial joints with a capacitive sensor array,” *J Biomech*, vol. 37, no. 10, pp. 1623–1625, 2004, doi: 10.1016/j.jbiomech.2004.01.024.
- [52] H. Tanino, M. Higa, H. Ito, T. Sato, T. Matsuno, and S. Banks, “Intraoperative Soft-Tissue Tension Measurements During Total Hip Arthroplasty.” Poster presented at: 56th Annual Meeting of the Orthopaedic Research Society, New Orleans, Mar. 2010.
- [53] M. J. Rudert *et al.*, “A new sensor for measurement of dynamic contact stress in the hip,” *J Biomech Eng*, vol. 136, no. 3, pp. 035001–1–035001–8, 2014, doi: 10.1115/1.4026103.
- [54] “FlexiForce Standard Model 201,” *Tekscan*, 2016. <https://www.tekscan.com/products-solutions/force-sensors/a201> (accessed May 25, 2021).
- [55] N. Zhang, “Three-axis force-sensing hip implant for soft tissue tension assessment during total hip arthroplasty,” MSc Thesis, dept. of Biomech. Eng., Techn. Univ. of Delft, Delft, 2020.

B List of requirements

This appendix lists the list of requirements the mechanism must meet to be suitable for in-surgery use and compatible with the Corail implant. The requirements are divided into four sections: Force reading, Corail implant compatibility, suitability for in-surgery use, and assignment bounds. The justifications for the requirements are listed in *italics*.

B.1 Force reading

- B.1.1 Sensing range: 0 – 150 N for compressive axial forces, 0 – 75 N for normal forces, and 0 – 2π rad for the angle of engagement of the normal force.
Dr. B.J. Blaauw estimates the soft tissue tension during a THA to range between 50 – 120 N, with a peak maximum of 200 N [1]. The upper bound of the axial sensing range was set at 1.25 times the upper bound of the force range. The upper bound of the normal force range was set half as high, since most of the tension runs along the axial direction [1].
- B.1.2 Accuracy: Must have a maximum error of 20 N and, if the normal force exceeds 20 N, 0.15π rad. It would be nice to have a maximum error of 5 N and, if the normal force exceeds 5 N, 0.05π rad.
The required accuracy of the sensed forces is currently unknown. With an accuracy of 20 N and 0.15π rad the device can be used for approximating the force range and distribution within hip joints, information which can be used to update R.1.1 for further iterations of this design. However, I expect an accuracy of 5 N (10% of the lower bound of the estimated tension during surgery) and 0.05π rad, would be required to give sufficient insight into the force distribution within an individual hip.
- B.1.3 Resolution: 5 N.
10% of the lower bound of the estimated tension during surgery.
- B.1.4 Min. frequency: 10.3 Hz.
Annett et al. found that participants were not able to perceive latencies up to 97 ms when performing inking tasks with a stylus with an obstructed view, and while watching on a separate screen [2]. The surgeon will also be performing a physical task while watching the force display. The latency will not be exceeded if the code runs with a minimum frequency of 10.3 Hz.

B.2 Corail implant compatibility

- B.2.1 Size: May use the space of the Corail trial implant's neck (\emptyset 13 mm, h 38,5 mm | cavity: \emptyset 11 mm, h 25 mm) and head (\emptyset 32). The geometry may exceed these sizes, but then the restrictions in implant range of motion must be determined.

B.3 Suitability for in-surgery use

- B.3.1 Max. deformation: 1 mm under a load of 40 kg.
This value was determined in consultation with MD Bryan Blaauw in an earlier StemForce thesis [3].
- B.3.2 Max. static load: Must withstand a total of 300 N compressive axial force and normal force without breaking or permanently deforming.
The maximum expected hip force of 200 N multiplied by a safety factor of 1.5.
- B.3.3 Biocompatibility: All materials in direct contact with the patient must be biocompatible and resistant to bodily fluids. Wire connections must be sealed.
- B.3.4 Sterilisable: Must withstand temperatures up to 135 °C, and pressures up to 3.1 bar during at least three autoclave cycles.
Autoclaves have different types of sterilisation programs. The devices reach temperatures of around 110 – 135 °C, and pressures up to 3.1 bar [4], [5].
- B.3.5 Max. set-up time: 60 s.

B.4 Assignment bounds

- B.4.1 Working principle: Should use Hall sensors, magnets, and a compliant mechanical displacement amplifier.
- B.4.2 Adaptability: The device should be easily adaptable for different uses, needs, and further development.
- B.4.3 Compatibility: Must be compatible with the Inertial Measurement Unit (IMU) which will be installed on the trial implant.

B.5 References

- [1] N. Zhang, "Three-axis force-sensing hip implant for soft tissue tension assessment during total hip arthroplasty," MSc Thesis, dept. of Biomech. Eng., Techn. Univ. of Delft, Delft, 2020.
- [2] M. Annett, A. Ng, P. Dietz, W. F. Bischof, and A. Gupta, "How Low Should We Go? Understanding the Perception of Latency While Inking," in *GI '14: Graphics Interface*, Montreal Quebec Canada: Canadian Information Processing Society, May 2014, pp. 167–174.
- [3] D. Van der Pol, "Assessment of soft tissue tension during total hip arthroplasty." MSc Thesis, Dept. of Biomed. Eng., Techn. Univ. of Delft, Delft, 2017.
- [4] AutoclaveDepot, "Autoclave Comparison Chart | Compare Autoclaves Midmark & Tuttnauer." <https://www.autoclavedepot.com/autoclave-comparison-chart/> (accessed Sep. 02, 2019).
- [5] S. Ferretti, "Load type and process/ autoclave selection - Basics and Recent Developments for Autoclaves and Lyophilizers." Presentation slides, PDA Europe, Tel Aviv, Israel, Nov. 13, 2017. [Online]. Available: <http://pdaisrael.co.il/131117/PDA Fedegari Sara Ferretti AutoClave Selection.pdf>

C Mathematical derivation

This appendix describes the mathematical derivation of the 3 degrees of freedom hip force sensing mechanism. This mechanism makes use of three Hall sensors, each paired with a magnet and a compliant movement amplifier. Each sensor will put out voltages which correspond to the forces applied to their accompanying compliant amplifier. These forces must be converted to the axial component, the normal component, and the directional angle α of the normal component of the total applied force. Figure 1A shows a simplified top view of the mechanism, including sensor placement and angle definition. Angle α is 0 rad if the normal force is applied from the direction of sensor 1, increases to $2\pi/3$ rad when the force direction shifts to sensor 2, and to $4\pi/3$ rad when the force direction shifts to sensor 3. The z-axis runs along the axis of the implant neck and the mechanism.

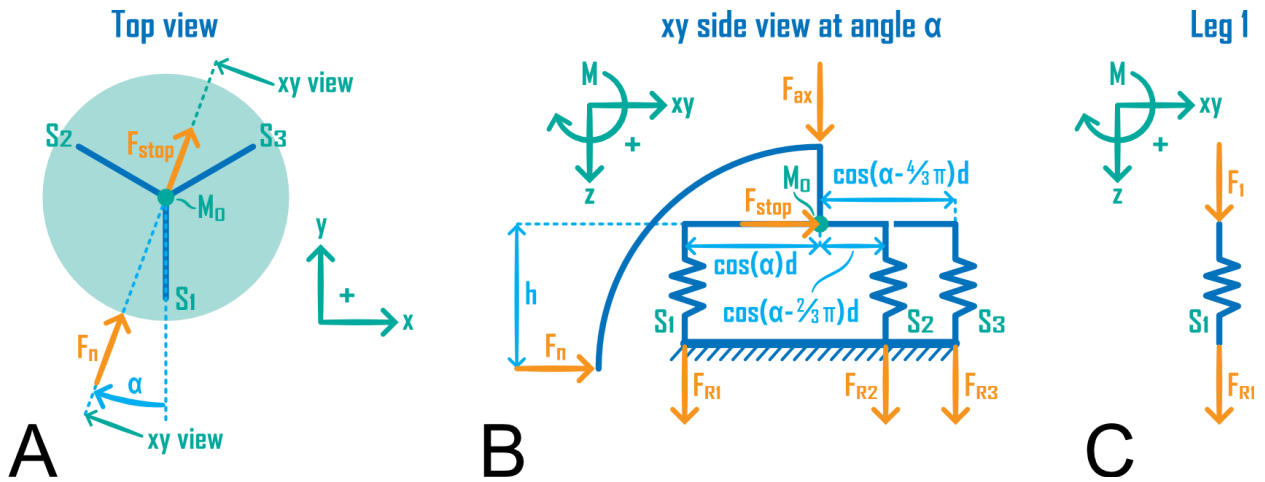


Figure 1: Free body diagrams of the mechanism. A: top view, the z-axis goes into the page. B: Slice made at angle α , side view. The xy-axis lies in the xy-plane. The figure shows a schematic view of the mechanism and part of the head. C: Forces acting on leg 1.

Figure 1B shows a simplified free body diagram of the mechanism, viewed from the side, perpendicular to normal force component. The xy-axis lies in the xy-plane, and changes along with angle α . The following simplifications and boundaries were assumed:

- The moment arm h of the applied normal force component is constant.
- The mechanical amplifiers are simplified to horizontal arms with constant length d , and vertical linear springs. Figure 1C shows the forces acting on one of the springs.
- No external moments act on the mechanism. All forces applied to the mechanism go through the centre of the head of the implant. The axial component of these forces acts as a point force on the centre joint of the arms. The normal component acts as a moment on the same centre joint. The springs are not subject to normal forces.

There are three equations of equilibrium:

$$C (1) \quad \Sigma F_{xy} = 0; F_n + F_{stop} = 0$$

$$C (2) \quad \Sigma F_z = 0; F_{ax} + F_{R1} + F_{R2} + F_{R3} = 0$$

$$C (3) \quad \Sigma M = 0$$

Rewriting yields:

$$\text{C (4)} \quad \mathbf{F}_{ax} = -\mathbf{F}_{R1} - \mathbf{F}_{R2} - \mathbf{F}_{R3} = \mathbf{F}_1 + \mathbf{F}_2 + \mathbf{F}_3$$

$$\text{C (5)} \quad M_n + M_1 + M_2 + M_3 = 0$$

$$\text{C (6)} \quad F_n \cdot h + F_{R1} \cdot d \cdot \cos(\alpha) + F_{R2} \cdot d \cdot \cos\left(\alpha - \frac{2}{3}\pi\right) + F_{R3} \cdot d \cdot \cos\left(\alpha - \frac{4}{3}\pi\right) = 0$$

$$\text{C (7)} \quad F_n = -\frac{d}{h} \cdot \left(F_{R1} \cdot \cos(\alpha) + F_{R2} \cdot \cos\left(\alpha - \frac{2}{3}\pi\right) + F_{R3} \cdot \cos\left(\alpha - \frac{4}{3}\pi\right) \right)$$

The reactive ground forces can be divided into two components: the components caused by F_n and the component caused by F_{ax} . The component caused by F_{ax} is equal on each amplifier, since it is an axial force:

$$\text{C (8)} \quad F_{R1} = -F_1 = -F_{1n} - \frac{F_{ax}}{3}; \quad F_{1n} = F_1 - \frac{F_{ax}}{3}$$

$$\text{C (9)} \quad F_{R2} = -F_2 = -F_{2n} - \frac{F_{ax}}{3}; \quad F_{2n} = F_2 - \frac{F_{ax}}{3}$$

$$\text{C (10)} \quad F_{R3} = -F_3 = -F_{3n} - \frac{F_{ax}}{3}; \quad F_{3n} = F_3 - \frac{F_{ax}}{3}$$

Combining formulas 7 to 10 yields:

$$\text{C (11)} \quad \mathbf{F}_n = \frac{d}{h} \cdot \left(\mathbf{F}_1 \cdot \cos(\alpha) + \mathbf{F}_2 \cdot \cos\left(\alpha - \frac{2}{3}\pi\right) + \mathbf{F}_3 \cdot \cos\left(\alpha - \frac{4}{3}\pi\right) \right)$$

The mechanism contains three linear springs. The linear spring formula is:

$$\text{C (12)} \quad F = k \cdot x$$

In which k is the spring stiffness in (N/m) and x is the displacement from the spring's neutral position in (m). This formula can be used for solely force components caused by F_n :

$$\text{C (13)} \quad F_{1n} = k \cdot x_1$$

$$\text{C (14)} \quad F_{2n} = k \cdot x_2$$

$$\text{C (15)} \quad F_{3n} = k \cdot x_3$$

In which x_1 , x_2 , and x_3 are the displacements from the springs' neutral position caused by F_n . The formulas can be combined to:

$$\text{C (16)} \quad \frac{F_{1n}}{x_1} = \frac{F_{2n}}{x_2} = \frac{F_{3n}}{x_3}$$

The springs have equal initial length and are connected to the same base and upper plate (Figure 2).



Figure 2: Bending of the mechanism.

Their displacements can be rewritten to:

$$C (17) \quad x_1 = \sin \beta \cos \alpha$$

$$C (18) \quad x_2 = \sin \beta \cos \left(\alpha + \frac{2}{3} \right)$$

$$C (19) \quad x_3 = \sin \beta \cos \left(\alpha + \frac{4}{3} \right)$$

Combining formulas 17 to 19 yields:

$$C (20) \quad \frac{F_{1n}}{\cos(\alpha)} = \frac{F_{2n}}{\cos\left(\alpha - \frac{2}{3}\pi\right)} = \frac{F_{3n}}{\cos\left(\alpha - \frac{4}{3}\pi\right)}$$

Rewriting yields:

$$C (21) \quad \frac{F_{1n}}{2 \cdot \cos(\alpha)} = \frac{F_{2n}}{\sqrt{3} \cdot \sin(\alpha) - \cos(\alpha)} = \frac{F_{3n}}{-\sqrt{3} \cdot \sin(\alpha) - \cos(\alpha)}$$

$$C (22) \quad F_{1n} \cdot (\sqrt{3} \cdot \sin(\alpha) - \cos(\alpha)) = F_{2n} \cdot (2 \cdot \cos(\alpha))$$

$$C (23) \quad \sqrt{3} \cdot \sin(\alpha) \cdot F_{1n} - \cos(\alpha) \cdot F_{1n} = 2 \cdot \cos(\alpha) \cdot F_{2n}$$

$$C (24) \quad \sin(\alpha) \cdot \sqrt{3} \cdot F_{1n} = \cos(\alpha) \cdot (2 \cdot F_{2n} + F_{1n})$$

$$C (25) \quad \frac{\sin(\alpha)}{\cos(\alpha)} = \tan(\alpha) = \frac{F_{1n} + 2 \cdot F_{2n}}{\sqrt{3} \cdot F_{1n}}$$

$$C (26) \quad \alpha = \arctan \left(\frac{F_{1n} + 2 \cdot F_{2n}}{\sqrt{3} \cdot F_{1n}} \right) + n \cdot \pi, \text{ with } n \in \mathbb{Z}$$

$$C (27) \quad \alpha = \arctan \left(\frac{3 \cdot F_1 + 6 \cdot F_2 - 3 \cdot F_{ax}}{3 \sqrt{3} \cdot F_1 - \sqrt{3} \cdot F_{ax}} \right) + n \cdot \pi, \text{ with } n \in \mathbb{Z}$$

The forces are calculated in newtons, the angles in radians, the distances in metres, and the moments in newton metres. A tangent can only be used to calculate angles between $-\frac{\pi}{2} \text{ rad}$ and $\frac{\pi}{2} \text{ rad}$, while the range of a full circle ($2\pi \text{ rad}$) is needed. Angle α calculated in formula 27 can be off by $\pi \text{ rad}$ and as a result the force F_n calculated in formula 11 would be negative. This must be corrected by adding $\pi \text{ rad}$ to the calculated angle and changing the sign of the normal force. The chosen bounds for angle α are $0 \text{ rad} \leq \alpha \leq 2\pi \text{ rad}$. The angle is adjusted by $2\pi \text{ rad}$ to adhere to these bound where needed.

The combination of formulas C 4, C 11, and C 27 describes the relationship between the forces per amplifier and the resolved applied force and its angle of engagement.

D Comparison between the simulation and the prototype

This appendix details the method used to compare the elastic deformation in the compliant mechanism between the physical proof-of-principle prototype and its simulated counterpart, while subjected to 65 *N* axial force.

D.1 Method

D.1.1 Definition of the deformation

The deformation was measured in a flexor, in the centre of the surface connected to a magnet (magnet-holder). It was defined as the horizontal displacement with respect to the centreline of the compliant mechanism, when the applied force load is increased from 0 *N* to 65 *N*.

D.1.2 Measuring and calculation methods

Solidworks simulation

The Solidworks model was subjected to an applied axial force of 65 *N*. The probing tool was used to measure the displacement.

Physical prototype

Photographs were made during test phase 3 of the proof-of-principle test, when the prototype sans head was subjected to an axial force ranging from 0 – 65 *N*. The displacement was estimated by comparing the photographs made of the prototype while it was subjected to 0 *N* and 65 *N* axial force. Lines were drawn on the photographs to assess the distance between the magnet plate (Figure 1):

D.1.2.1 Line *a*: drawn along the side of the support beam.

D.1.2.2 Line *b*: parallel to line *a*, drawn over the top outer edge of the flexor, just below the curvature connecting it to the rest of the compliant mechanism.

D.1.2.3 Line *c*: perpendicular to line *a*, connecting it with line *b*.

D.1.2.4 Line *d*: drawn on the magnet-holder.

D.1.2.5 Line *e*: parallel to line *c*, connects line *a* with *d* along the top of the magnet holder.

D.1.2.6 Line *f*: parallel to line *c*, connects line *a* with *d* along the bottom of the magnet holder.

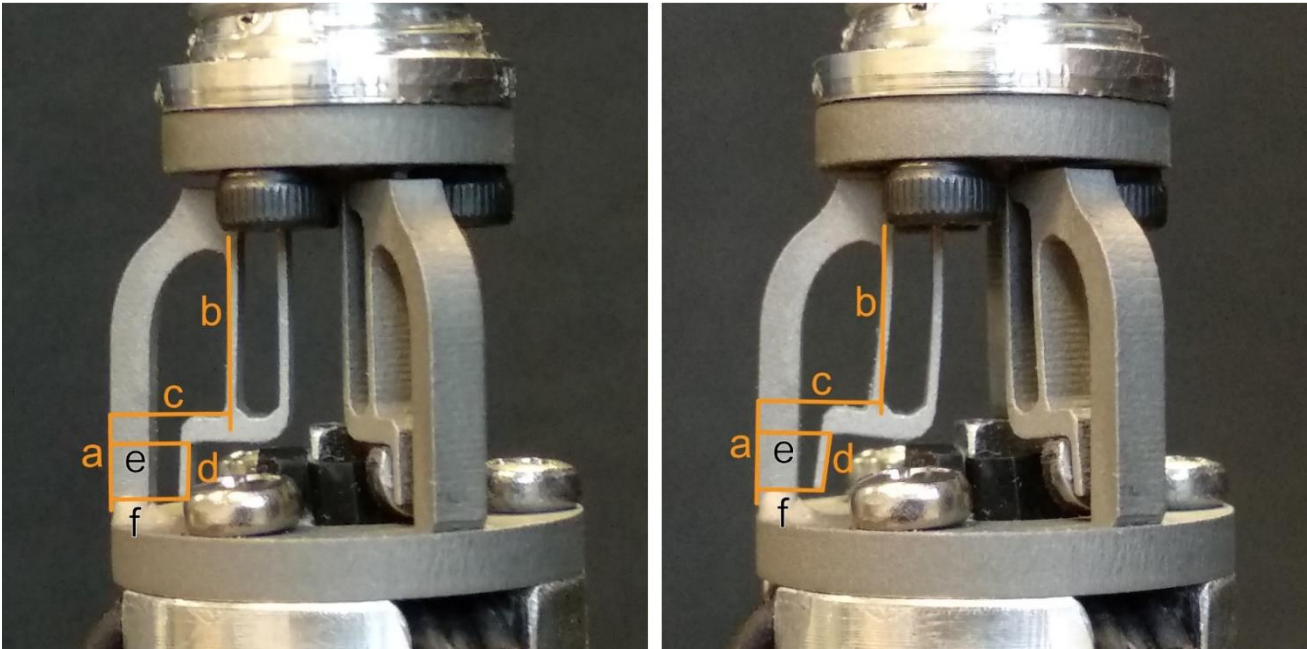


Figure 1: The lines drawn on top of the photographs of the mechanism. The left picture was taken prior to force loading, the right was taken during a force appliance of 65 N.

According to the Solidworks model, the length of line c is $C = 4 \text{ mm}$. The lengths of lines $c, e,$ and f are measured in both photos. The distance between the support beam and the magnet plate was defined for each photo using the following formula:

$$(D1) \text{ Distance} = \frac{e+f}{2} \cdot \frac{C}{c}, \text{ in } mm \text{ and in which the lowercase symbols refer to the lengths of the lines.}$$

The displacement was calculated by subtracting the distance of the 0 N photograph from the 65 N photograph.

The difference between the simulation and prototype

The difference between the displacements of the simulation and the prototype was calculated by dividing the latter displacement by the former.

E Code

This appendix is a collection of all the code used during the force tests of the prototypes.

E.1 Matlab code proof-of-principle prototype

```
% This code reads the output of 3 Hall sensors through an Arduino
% Created by Tessa Mol, 06-12-2019.

%% Set-up
clear all
close all
clc
global a V1 V2 V3                % Ensure the variables can be shared with the button
function
a = arduino();                  % Connect to the Arduino Uno

%% Preparing the animated figure
% Preparing the live figure
f1 = figure;                    % Open figure
V1 = animatedline('Color','b'); % Create an animated line for sensor 1
V2 = animatedline('Color','r'); % Create an animated line for sensor 2
V3 = animatedline('Color','y'); % Create an animated line for sensor 3
ax = gca;                       % Return the current axes for the current figure
ax.YGrid = 'on';                % Turn on grid
ax.YLim = [2.5 3.5];           % Set Y-axis range to 0-1 V
xlabel('time (s)'), ylabel('voltage (V)'), title('Voltage output of the Hall sensors')
legend('Sensor 1','Sensor 2','Sensor 3')

%% Acquire and display sensor data
% Creating a start/stop button for data recording
Stop_Button = uicontrol('Style','ToggleButton',...
    'String','Plot data', ...
    'Callback', @plotButtonPushed);

% button function including code for acquiring and saving data
function plotButtonPushed(hObject,eventdata,handles)
% hObject    handle to togglebutton1 (see GCBO)
% eventdata  reserved - to be defined in a future version of MATLAB
% handles    structure with handles and user data (see GUIDATA)

global a V1 V2 V3                % Share the variables with the function
button_state = get(hObject,'Value'); % Read the button state (0 or 1)
t_start = datetime('now');       % Set the starttime to current time

if button_state == get(hObject,'Min') % If the button is unpressed...
    clear t v1 v2 v3             % Clear variables for receiving data
    [t_date,v1] = getpoints(V1); % Copy measured datapoints sensor 1 to
logs                               % Copy measured datapoints sensor 2 to
    [t_date,v2] = getpoints(V2); % Copy measured datapoints sensor 3 to
logs                               % Copy measured datapoints sensor 3 to
    [t_date,v3] = getpoints(V3); % Copy measured datapoints sensor 3 to
logs                               % Copy measured datapoints sensor 3 to
    t = (t_date-t_date(1))*24*3600; % recalculate time to elapsed seconds

    f2 = figure;                % Preparing the plot
    plot(t,v1,t,v2,t,v3)        % Plotting the measured values
```

```

xlabel('Elapsed time (s)')
ylabel('Measured voltage (V)')
title('Voltage output of the Hall sensors')
legend('Sensor 1','Sensor 2','Sensor 3')

date = datestr(now,'mm-dd-yyyy_HH-MM-SS'); % Create datestring for filename data
save(date,'t','v1','v2','v3') % Save measured data to external file
saveas(f2,[date,'_Voltages']) % Save figure 3 to external file
saveas(f2,[date,'_Voltages'],'png') % Save figure 3 to external file

clear t v1 v2 v3 t_date % Clear variables for new data collection
clearpoints(V1) % Clear animated line for new data
collection
clearpoints(V2) % Clear animated line for new data
collection
clearpoints(V3) % Clear animated line for new data
collection
end

while button_state == get(hObject,'Max') % While the button is pressed...
    v1 = readVoltage(a,'A1'); % Read the current voltage value of
    sensor 1
    v2 = readVoltage(a,'A2'); % Read the current voltage value of
    sensor 2
    v3 = readVoltage(a,'A3'); % Read the current voltage value of
    sensor 3
    t = datetime('now') - t_start; % Get the current time
    addpoints(V1,datenum(t),v1) % Add point to animated line sensor 1
    addpoints(V2,datenum(t),v2) % Add point to animated line sensor 1
    addpoints(V3,datenum(t),v3) % Add point to animated line sensor 1
    ax.XLim = datenum([t-seconds(10) t]); % Update axes
    datetick('x','keeplimits') % Convert x-axis labels to time-based
    labels while preserving the axis limits
    drawnow % Force Matlab to immediately update the
    figure
    button_state = get(hObject,'Value'); % Fetch current button state
end

end

```

E.2 Arduino code final prototype

```

void setup() {

    // put your setup code here, to run once:

    Serial.begin(500000); // open the serial port at 500000 bps:

    analogReadResolution(12);

}

uint16_t n = 16; // Set number of measurements for filter

uint64_t S1 = 0; // Create variable to stack Analogread results (64 bits)

uint64_t S2 = 0; // Create variable to stack Analogread results (64 bits)

```

```
uint64_t S3 = 0;    // Create variable to stack Analogread results (64 bits)
```

```
void loop() {  
    // put your main code here, to run repeatedly:  
  
    S1 = 0;  
  
    S2 = 0;  
  
    S3 = 0;  
  
    for (int i = 0; i < n; i++){  
  
        S1 += (uint64_t)analogRead(A1);  
  
        S2 += (uint64_t)analogRead(A0);  
  
        S3 += (uint64_t)analogRead(A3);  
  
    }  
  
    Serial.print("V1=");  
  
    Serial.print(((double)((double)S1/(double)n),8);  
  
    Serial.print("V2=");  
  
    Serial.print(((double)((double)S2/(double)n),8);  
  
    Serial.print("V3=");  
  
    Serial.print(((double)((double)S3/(double)n),8);  
  
    Serial.println("END");  
  
    //delay(500);  
  
}
```

E.3 Matlab code final prototype displaying voltages

```
% This code reads the output of 3 Hall sensors through an Arduino.  
% To be used with the final prototype during calibration.  
% Created by Tessa Mo1, updated 08-03-2022
```

```
%% Set-up  
clear all  
close all  
clc  
global COM v V1 V2 V3           % Ensure the variables can be shared with the separate  
functions
```

```

COM = "COM4";           % Specify the COM-port number (check at device manager)
v = zeros(1, 3);       % Make empty voltage vector

%% Preparing the animated figure
% Preparing the live figure
f1 = figure;           % Open figure
V1 = animatedline('Color',[0 .447 .741]); % Create an animated line for sensor 1
V2 = animatedline('Color',[.85 .325 .098]); % Create an animated line for sensor 2
V3 = animatedline('Color',[.929 .694 .125]); % Create an animated line for sensor 3
ax = gca;              % Return the current axes for the current
figure
ax.YGrid = 'on';      % Turn on grid
ax.YLim = [0 1.5];   % Set Y-axis range in V
xlabel('time (s)'), ylabel('voltage (V)'), title('Voltage output of the Hall sensors')
legend('Sensor 1','Sensor 2','Sensor 3','Location','southwest')

%% Acquire and display sensor data
% Creating a start/stop button for data recording
Stop_Button = uicontrol('Style', 'ToggleButton',...
    'String', 'Plot data', ...
    'Callback', @plotButtonPushed);

% button function including code for acquiring and saving data
function plotButtonPushed(hObject,~,~)
    % hObject    handle to togglebutton1 (see GCBO)
    % eventdata  reserved - to be defined in a future version of MATLAB
    % handles     structure with handles and user data (see GUIDATA)

    global COM v V1 V2 V3 % Share the variables with the
function
    button_state = get(hObject, 'Value'); % Read the button state (0 or 1)

    if button_state == get(hObject, 'Min') % If the button is unpressed...
        clear t v1 v2 v3 % Clear variables for receiving data
        [~,v1] = getpoints(V1); % Copy measured datapoints sensor 1
to logs
        [~,v2] = getpoints(V2); % Copy measured datapoints sensor 2
to logs
        [t_date,v3] = getpoints(V3); % Copy measured datapoints sensor 3
to logs
        t = (t_date-t_date(1))*24*3600; % recalculate time to elapsed seconds

        f2 = figure; % Preparing the plot
        plot(t,v1,t,v2,t,v3) % Plotting the measured values
        xlabel('Elapsed time (s)')
        ylabel('Measured voltage (V)')
        title('Voltage output of the Hall sensors')
        legend('Sensor 1','Sensor 2','Sensor 3','Location','southwest')

        date = datestr(now, 'mm-dd-yyyy_HH-MM-SS'); % Create datestring for filename data
        save(date, 't', 'v1', 'v2', 'v3') % Save measured data to external file
        saveas(f2,[date, '_Voltages']) % Save figure 3 to external file
        saveas(f2,[date, '_Voltages'], 'png') % Save figure 3 to external file

        clear t v1 v2 v3 t_date % Clear variables for new data
collection
        clearpoints(V1) % Clear animated line for new data
collection
        clearpoints(V2) % Clear animated line for new data
collection
        clearpoints(V3) % Clear animated line for new data
collection

```

```

clear COMsensor % Disconnect from COM port
end

if button_state == get(hObject,'Max') % If the button is pressed... Load
COM port
COMsensor = serialport(COM,500000); % Set COM-port number and baud rate
(data transfer speed)
configureTerminator(COMsensor,"CR"); % Specify terminator character as
enter (enter is the end of the message)
configureCallback(COMsensor,"terminator",@ReadSensors); % Calls the function as
soon as there is new data
v = zeros(1,3); % Empty v, making sure no old data is
used
pause(2); % Wait for Matlab to start processing
measurements from Arduino
t_start = datetime('now'); % Set the starttime to current time

while button_state == get(hObject,'Max') % While the button is pressed...
t = datetime('now') - t_start; % Get the current time
addpoints(V1,datetime(t),v(1)) % Add point to animated line sensor 1
addpoints(V2,datetime(t),v(2)) % Add point to animated line sensor 1
addpoints(V3,datetime(t),v(3)) % Add point to animated line sensor 1
datetick('x','keeplimits') % Convert x-axis labels to time-based
labels while preserving the axis limits
drawnow % Force Matlab to immediately update
the figure
button_state = get(hObject,'Value'); % Fetch current button state
end
end
end

function ReadSensors(src, ~) % Function which reads the data sent
by the Arduino

global v % Give access to global variable v
data = char(readline(src)); % Read last send data line from
Arduino
ind1 = strfind(data,"V1="); % Find sensor 1 data in dataline
ind2 = strfind(data,"V2="); % Find sensor 2 data in dataline
ind3 = strfind(data,"V3="); % Find sensor 3 data in dataline
indend = strfind(data,"END"); % Find sensor 3 data in dataline

if ~isempty(ind1) && ~isempty(ind2) && ~isempty(ind3) % Check if sensor
data is present
numdatachars1 = (ind2-1) - (ind1+3); % Determine data
length per data point
numdatachars2 = (ind3-1) - (ind2+3); % Determine data
length per data point
numdatachars3 = (indend-1) - (ind3+3); % Determine data
length per data point
v1var = str2double(data(ind1+3:ind1+3+numdatachars1)); % Grab sensor 1
datastring from data line and convert to double
v2var = str2double(data(ind2+3:ind2+3+numdatachars2)); % Grab sensor 2
datastring from data line and convert to double
v3var = str2double(data(ind3+3:ind3+3+numdatachars3)); % Grab sensor 3
datastring from data line and convert to double
if ~isempty(v1var) && ~isempty(v2var) && ~isempty(v3var) % Check if all sensor
data is valid (doubles)
v(1) = v1var*0.0008056640625; % Convert sensor 1
data from ADC bits to V (/2^12*3.3 V) and output to global variable
v(2) = v2var*0.0008056640625; % Convert sensor 2
data from ADC bits to V (/2^12*3.3 V) and output to global variable

```

```

        v(3) = v3var*0.0008056640625; % Convert sensor 3
data from ADC bits to V (/2^12*3.3 V) and output to global variable
    end
end
end

```

E.4 Matlab code final prototype displaying calculated forces

```

% This code reads the output of 3 Hall sensors through an Arduino and uses
% this to calculate the force input on the prototype.

```

```

% To be used with the final prototype during testing.
% Created by Tessa Mol, updated 08-03-2022.

```

```

% Ensure vcor values, DSHB, and regression lines are from the correct
% calibration

```

```

%% Set-up

```

```

clear all

```

```

close all

```

```

clc

```

```

global COM Fa Fn an v Regs % Ensure the variables can be shared with the button
function

```

```

COM = "COM4"; % Specify the COM-port number (check at device manager)

```

```

v = zeros(1, 3); % Make empty voltage vector

```

```

load('calibration.mat'); % Load calibration values

```

```

%% Preparing the animated figure

```

```

f1 = figure; % Open figure

```

```

    set(gcf, 'units','normalized','outerposition',[0 0.1 1 .9]);

```

```

    ax = gca; % Return the current axes for the current

```

```

figure

```

```

    ax.YGrid = 'on'; % Turn on grid

```

```

    yyaxis left

```

```

    Fa = animatedline('Color',[0 .447 .741]); % Create an animated line for Force x

```

```

    Fn = animatedline('Color',[.929 .694 .125]); % Create an animated line for Force y

```

```

    ax.YLim = [-100 100]; % Set Y-axis range to V

```

```

    set(gca,'YTick',0:20:100)

```

```

    ylabel('Force (N)')

```

```

    yyaxis right

```

```

    an = animatedline('Color',[.85 .325 .098]); % Create an animated line for Force z

```

```

    ax.YLim = [0 4*pi]; % Set Y-axis range to 0-1 V

```

```

    set(gca,'YTick',0:pi/3:2*pi)

```

```

    ax.YGrid = 'on';

```

```

    ax.YTickLabel = {'0', '^1}/_3 \pi', '^2}/_3 \pi', '\pi', '^4}/_3 \pi', '^5}/_3

```

```

\pi', '2\pi'};

```

```

    yline(2*pi);

```

```

    xlabel('time (s)'), ylabel('Angle (\alpha)'), title('Axial force, normal force,
normal force angle')

```

```

    legend('Axial force','Normal force','Force angle','Location','west')

```

```

%% Acquire and display sensor data

```

```

% Creating a start/stop button for data recording

```

```

Stop_Button = uicontrol('Style', 'ToggleButton',...

```

```

    'String', 'Plot data', ...

```

```

    'Callback', @plotButtonPushed);

```

```

% button function including code for acquiring and saving data

```

```

function plotButtonPushed(hObject,~,~)

```

```

    % hObject handle to togglebutton1 (see GCBO)

```

```

    % eventdata reserved - to be defined in a future version of MATLAB

```

```

    % handles structure with handles and user data (see GUIDATA)

```

```

    global COM Fa Fn an v Regs % Share the variables with the
function % Read the button state (0 or 1)
    button_state = get(hObject, 'Value');

    if button_state == get(hObject, 'Min') % If the button is unpressed...
        clear t F % Clear variables for receiving data
        [~,F{1}] = getpoints(Fa); % Copy measured axial force to logs
        [~,F{2}] = getpoints(Fn); % Copy measured normal force to logs
        [t_date,F{3}] = getpoints(an); % Copy measured normal force angle to
logs % recalculate time to elapsed seconds
        t = (t_date-t_date(1))*24*3600;

        f2 = figure; % Preparing the plot
        sgtitle('Final prototype test data')
        subplot(1,2,1)
            plot(t,F{1},t,F{2}) % Plotting the measured forces
            xlabel('Elapsed time (s)')
            ylabel('Force (N)')
            title('Measured forces')
            legend('Fa','Fn')
        subplot(1,2,2) % Plotting the tangential force angle
            plot(t,F{3})
            xlabel('Elapsed time (s)')
            ylabel('Angle (rad)')
            title('Measured tangential force angle')
            legend('\alpha')

        date = datestr(now, 'mm-dd-yyyy_HH-MM-SS'); % Create datestring for filename data
        save(date, 't', 'F') % Save measured data to external file
        saveas(f2,[date, '_Forces']) % Save figure 3 to external file
        saveas(f2,[date, '_Forces'],'png') % Save figure 3 to external file

        clear t F t_date % Clear variables for new data
collection % Reset v
        v = zeros(1,3); % Clear animated line for new data
        clearpoints(Fa) % Clear animated line for new data
collection % Clear animated line for new data
        clearpoints(Fn) % Clear animated line for new data
collection % Clear animated line for new data
        clearpoints(an)
collection
    end

    if button_state == get(hObject, 'Max') % If the button is pressed... Load
COM port % Set COM-port number and baud rate
        COMsensor = serialport(COM,500000);
        (data transfer speed)
        configureTerminator(COMsensor, "CR"); % Specify terminator character as
enter (enter is the end of the message)
        configureCallback(COMsensor, "terminator", @ReadSensors); % Calls the function as
soon as there is new data
        v = zeros(1,3); % Empty v, making sure no old data is
used % Wait for Matlab to start processing
        pause(2);
measurements from Arduino

        for j = 1:50 % Collect the first 50 datapoints for
startpoint correction
            vcor(j,:) = v;
        end
end

```

```

vcor = [0.41729 - mean(vcor(:,1)), 0.79854 - mean(vcor(:,2)), 0.85083 -
mean(vcor(:,3))]; % Calibration zero - the average of the first 50 datapoints
t_start = datetime('now'); % Set the starttime to current time

while button_state == get(hObject,'Max') % While the button is pressed...
    t = datetime('now') - t_start; % Get the current time
    vcorr = v+vcor; % Correct voltage
    F123 = -[Regs{1}(vcorr(1));Regs{2}(vcorr(2));Regs{3}(vcorr(3))]; % Convert
voltages from the sensors to predicted reaction forces per sensor

    % Divide the forces into components - The force angle is zero towards flexor
1, and increases clockwise.
    Fana(1) = -sum(F123); % Axial force
    Fs123 = F123 + (Fana(1)/3); % Subtracting the axial components
of F1 F2 and F3

    % Determine the angle alpha - This angle is always between -pi/2 and pi/2.
    Fana(3) = atan((Fs123(1)+2*Fs123(2))./(sqrt(3).*Fs123(1))); % Alpha

    % Determine the normal force (First value is DSHB)
    Fana(2) = -(1.594111672234739)*(cos(Fana(3))*F123(1)+cos(Fana(3)-
2/3*pi)*F123(2)+cos(Fana(3)-4/3*pi)*F123(3));

    % Adjust the angle alpha and the tangential force - Alpha is off by the pi if
the tangential force is negative. This must be corrected
    if Fana(2) < 0
        Fana(2) = -Fana(2);
        Fana(3) = Fana(3)+pi;
    end

    % Correct the current range (-pi/2 to 3pi/2) to the preferred range (0pi to
2pi)
    if Fana(3) < 0
        Fana(3) = Fana(3)+2*pi;
    end

    % [Fana] = FP_VtoN(v); % Convert the measured voltages to
axial and tangential forces and force angle.
    addpoints(Fa,datenum(t),Fana(1)) % Add point to animated line Fa
    addpoints(Fn,datenum(t),Fana(2)) % Add point to animated line Fn
    addpoints(an,datenum(t),Fana(3)) % Add point to animated line an
    datetick('x','keeplimits') % Convert x-axis labels to time-based
labels while preserving the axis limits
    drawnow % Force Matlab to immediately update
the figure
    button_state = get(hObject,'Value'); % Fetch current button state
end
end
end

function ReadSensors(src, ~) % Function which reads the data sent
by the Arduino

    global v % Give access to global variable v
    data = char(readline(src)); % Read last send data line from
Arduino
    ind1 = strfind(data,"V1="); % Find sensor 1 data in dataline
    ind2 = strfind(data,"V2="); % Find sensor 2 data in dataline
    ind3 = strfind(data,"V3="); % Find sensor 3 data in dataline
    indend = strfind(data,"END"); % Find sensor 3 data in dataline

```

```

    if ~isempty(ind1) && ~isempty(ind2) && ~isempty(ind3)           % Check if sensor
data is present
        numdatachars1 = (ind2-1) - (ind1+3);                       % Determine data
length per data point
        numdatachars2 = (ind3-1) - (ind2+3);                       % Determine data
length per data point
        numdatachars3 = (indend-1) - (ind3+3);                     % Determine data
length per data point
        v1var = str2double(data(ind1+3:ind1+3+numdatachars1));     % Grab sensor 1
datastring from data line and convert to double
        v2var = str2double(data(ind2+3:ind2+3+numdatachars2));     % Grab sensor 2
datastring from data line and convert to double
        v3var = str2double(data(ind3+3:ind3+3+numdatachars3));     % Grab sensor 3
datastring from data line and convert to double
        if ~isempty(v1var) && ~isempty(v2var) && ~isempty(v3var)   % Check if all sensor
data is valid (doubles)
            v(1) = v1var*0.0008056640625;                          % Convert sensor 1
data from ADC bits to V (/2^12*3.3 V) and output to global variable
            v(2) = v2var*0.0008056640625;                          % Convert sensor 2
data from ADC bits to V (/2^12*3.3 V) and output to global variable
            v(3) = v3var*0.0008056640625;                          % Convert
sensor 3 data from bits to v (/2^12*3.3 V) and output to global variable
        end
    end
end
end

```

F Material and production method selection

This appendix discusses both the materials and production processes selection of the compliant mechanism and the sensor base. The production processes and material are dependent on each other and on the geometry of the design. The materials of both the compliant mechanism and the sensor base should be biocompatible, non-magnetic, able to withstand bodily fluids and withstand multiple cycles of the autoclave in hot steam.

F.1 Compliant mechanism

F.1.1 Production processes selection

The design is unsuitable for milling out of one part, because of the intricacy of the geometry. Therefore, it was decided to divide it into separate parts made from plate material. Two production methods needed to be selected: one which cuts the parts from plate material and one which joins the parts.

The material database Granta EduPack (2021 R2, Ansys, Canonsburg, USA) was used to select three cutting methods for consideration: water jet cutting, laser cutting, and wire electrical discharge machining (EDM). These methods can cut with excellent precisions and are suitable for use during prototyping, as they only require a digital drawing of the parts. Further information was gathered during a consultation with Bert Bakker from Dienst Elektronische en Mechanische Ontwikkeling (DEMO, Delft, the Netherlands). The parts were to be produced to a tolerance of ± 0.01 mm.

Water jet cutting

During water jet cutting the material is cut using a thin water jet which can be enriched with an abrasive medium. The process was found unsuitable for this project, as the minimal jet diameter is too large for creating the tight gap in the pivot of the mechanism [1].

Laser cutting

Laser cutting uses a thin laser to cut the material. This method was the most accessible and was used for the proof-of-principle prototype, albeit not to the tight tolerances required for the final design. Two companies consulted by Bert Bakker could produce the parts to the required tolerances.

Wire EDM

In wire EDM material is removed by electrical discharges between a wire and the plate material [2]. This method can cut the parts to the required precision but is several times more expensive than laser cutting.

Joining processes: silver brazing and laser welding

The compliant mechanism of the proof-of-principle prototype was assembled using silver brazing. This method results in strong connections between parts, but also subjects the parts to a lot of heat. This can change material properties and warp the geometry. Additionally, this method could not reach the desired precision. In consultation with Bert Bakker it was decided to change the joining process to laser welding. This method is more precise and faster, requiring the material to be heated for a shorter time.

Selection

It was decided to cut the compliant mechanism parts by laser cutting and join them by laser welding. Precisie Laser (Veenendaal, the Netherlands) produced three compliant mechanisms for € 78,63/p.

F.1.2 Material selection

The compliant mechanism must withstand high forces while remaining flexible, e.g., the young's modulus (σ_y) to yield strength (E) ratio of the material should be low. Thermoplastics were not considered, as they exhibit elastic hysteresis; it requires more energy to cause strain than release strain due to internal friction. Correspondingly, these materials show different curves on a stress strain graph during the loading and unloading phase. The quicker the loading and unloading is performed, the more noticeable the hysteresis is. This phenomenon would cause inaccuracy in the results. The materials should be compatible with at least one of the earlier mentioned cutting methods and laser welding. Possible materials were selected using the GRANTA Edupack materials database (2020 R2, Ansys, Canonsburg, USA) and Van der Pol's prior research [3]. The database enables the comparison of the materials that meet the above-mentioned requirements through a visual medium. Van der Pol's prior research shows his selection process of materials which had to meet similar requirements. The next paragraphs describe the considered materials.

Titanium

Titanium has an excellent σ_y/E ratio (Table 1), especially titanium alloy Ti-12Mo-6Zr-2Fe. The material is non-magnetic. Titanium is not suitable for brazing and was excluded from consideration when this was the preferred joining method.

Table 1: The average young's modulus to yield strength ratio, based on values reported by GRANTA Edupack Database 2020.

Average σ_y/E ratio			
Titanium	Nitinol		Stainless steel
Ti-12Mo-6Zr-2Fe	Austenitic	Elgiloy	AISI 301
$8.5 \cdot 10^{-2}$	$3.1 \cdot 10^{-1}$	$1.6 \cdot 10^{-1}$	$2.1 \cdot 10^{-1}$
	Martensitic: $4.9 \cdot 10^{-1}$		

Nitinol

The crystal structure of this nickel titanium alloy can change between martensitic and austenitic state while undergoing temperature changes or while under pressure within a certain temperature range. This transition is reversible. The transition temperature can be between -50 to 150, depending on the composition of the material. The shape of the structure is defined in the austenitic phase - when the material is above the transition temperature. The structure will revert to this shape when it is heated to the austenitic phase, even when it has been deformed in the martensitic phase. This phenomenon could be used to undo any accidental permanent deformations to the structure. For this to work, the transition temperature should lay between body temperature and autoclave temperature. However, nitinol shows considerable elastic hysteresis during its phase transition. Thus, phase transitions should be avoided during measurements. Nitinol can be soldered, but it can be a difficult process [4]. There are only few suppliers, thus the material is difficult to acquire. Especially considering the strict qualifications that are needed.

Stainless steel alloy AISI 301

This material is also called spring steel. It has a low σ_y/E ratio (Table 1) and is suitable for brazing. Its price per volume is the lowest of all materials considered and the TU Delft already had contact with a supplier. However, during simulations the requirements could not be met when the compliant mechanism was made of this material. Therefore, this material was found unsuitable.

Elgiloy

This cobalt-based alloy has a low σ_y/E ratio (Table 1), is non-magnetic, suitable for brazing, and has an excellent fatigue strength. It is more expensive per volume than titanium, but also has a higher yield strength. This means less material is needed to withstand the same force loads and thus reduces the effective price difference. The smaller amount of material needed is a huge benefit, since there is only limited space available for the compliant mechanism.

Selection

Elgiloy was selected, as it was the only available material which met all the criteria. Thicker titanium sheet metal could be a suitable substitute in further designs, since the prototype is no longer joined by brazing.

F.2 Sensor base

The sensor base of the proof-of-principle prototype was made from aluminium. The sensors needed to be wrapped in insulation tape to prevent short circuiting. The sensor base of the final design is in contact with both the sensors as well as the PCB. It was designed to change the material to an electrical insulator to forgo the need for additional insulating barriers. Additionally, the material needs excellent dimensional stability throughout multiple autoclave cycles. Warping in the base changes the positions of the sensors, which would reduce the mechanism's force measuring accuracy and might even cause the need for recalibration. Other factors considered were material price and processability. Suitable materials were sought by consulting the material database Granta EduPack (2021 R2, Ansys, Canonsburg, USA) and the lists of autoclavable plastics on both Ensinger's and Modern Plastic's websites [5], [6]. Little information is available on most plastic's dimensional stability when autoclaved. However, a suitable material was found.

Medical grade polyacetal copolymer

Medical grade polyacetal copolymer (POM-C) material has excellent dimensional stability [6] and most grades can be autoclaved up to 800 sterilization cycles without showing significant loss of mechanical properties [5]. This material is suitable for both injection moulding and machining, which can be suitable production methods depending on the production size.

F.3 References

- [1] "Precision and Quality," *Waterjet University*. <https://wardjet.com/waterjet/university/precision-quality> (accessed May 28, 2021).
- [2] Headland, "How Does Wire EDM Work?" <https://www.headland.com.au/how-does-wire-edm-work/> (accessed May 28, 2021).
- [3] D. Van der Pol, "Assessment of soft tissue tension during total hip arthroplasty." MSc Thesis, Dept. of Biomed. Eng., Techn. Univ. of Delft, Delft, 2017.
- [4] E. Bastow, "What is the best way to solder to Nitinol?," 2011. <https://www.indium.com/blog/what-is-the-best-way-to-solder-to-nitinol.php> (accessed Sep. 02, 2020).
- [5] "Sterilisable and autoclavable medical grade plastics," *Ensinger Plastics*. <https://www.ensingerplastics.com/en/shapes/plastic-material-selection/sterilisable-autoclavable> (accessed Dec. 21, 2021).
- [6] "Better Plastics for Medical Devices," *Modern Plastics*. <https://modernplastics.com/industries/plastics-for-medical-devices/> (accessed Mar. 20, 2023).

G Sensor-magnet distance test

G.1 Introduction

In this test, the interaction between two different types of Hall sensors and several magnets was sampled at varying distances. This was done to identify the pairing and distance range which yielded the highest sensitivity, the highest output voltage change per movement range.

G.2 Method

Table 1 lists the used sensor and magnet types and Figure 1 shows the test set-up. Callipers were placed in a cardboard stand. A Hall sensor was taped to the lower jaw of the callipers with double sided tape. Wires were soldered to the sensor pins and connected to an Arduino (Uno, Arduino, USA). A magnet was stuck to the upper jaw of the callipers. The Arduino was connected to a laptop running Matlab (2019A, Natick, USA).

Table 1: The pre-selected sensors and magnets. Sensor data from datasheets. [1], [2]

Company	Type	Size (mm)	Input (V)	Operating temp. (°C)
Allegro, USA	A1302	4.1 · 3.0 · 1.5	4.5 – 5.5	–40 – 150
Honeywell, USA	SS49E	4.1 · 3.0 · 1.7	2.7 – 6.5	–40 – 100

Company	Size (mm)
Supermagnete, Germany	Ø2 · 1
Supermagnete, Germany	Ø3 · 2
Wish, USA	Ø2 · 1
Wish, USA	Ø3 · 2

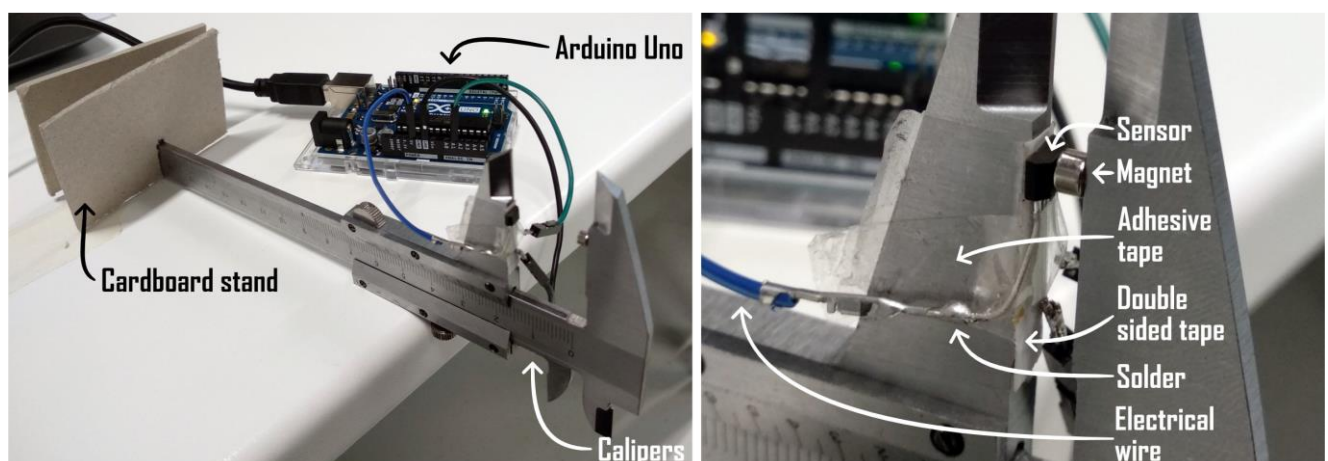


Figure 1: Sensor and magnet selection test set-up.

At the start of each measurement round the callipers were closed as far as possible and recalibrated to zero. The sensor output was read using Matlab at distances between 0 – 4.5 mm with 0.5 – 1 mm intervals. The distance was plotted against the output voltage. Additional data points were collected to smoothen out the

curve. Sensors and magnets were switched between measurements. The Allegro sensor was paired with each magnet type, the Honeywell sensor only with the Supermagnete magnets.

The chosen magnet did not have an accompanying specification sheet. Therefore, the magnet strength was approximated.

The equation for the magnetic flux density on the symmetry axis of a disc magnet is:

$$B = \frac{Br}{2} \left(\frac{D+z}{\sqrt{r^2 + (D+z)^2}} - \frac{z}{\sqrt{r^2 + z^2}} \right) \quad \text{Eq.1}$$

In which:

- B is the flux density in *Gauss*,
- z is the distance from the magnet in *mm*,
- r is the magnet radius *mm*,
- D is the magnet thickness *mm*,
- Br is the remanence field, the magnetic strength of the magnet [3].

The sensor output can be described by:

$$V_{out} = B \cdot sens + V_{out(Q)} \quad \text{Eq.2}$$

In which:

- V_{out} is the output in Volts,
- B is the flux density in *Gauss*,
- $sens$ is the output sensitivity in *V/Gauss*,
- $V_{out(Q)}$ is the quiescent voltage output.

These equations were combined into:

$$V_{out} = \frac{Br}{2} \left(\frac{D+z}{\sqrt{r^2 + (D+z)^2}} - \frac{z}{\sqrt{r^2 + z^2}} \right) \cdot sens + V_{out(Q)} \quad \text{Eq.3}$$

The strength of the chosen magnet was approximated by visually matching the voltage-distance plot of a theoretical magnet of equal size over that of the chosen magnet.

G.3 Results

The highest slopes, and thus the highest sensitivities, were achieved with the A1324 Allegro Hall sensor combined with one of the $\varnothing 2 \cdot 1 \text{ mm}$ magnets (Figure 2). The $\varnothing 2 \cdot 1 \text{ mm}$ Neodymium axial disc magnet from Wish is the most suitable for the mechanism, as the slope of the output curve remained high at a wider distance range. The voltage output was the most sensitive at a sensor-magnet distance ranging from 0.7 to 1.6 *mm*.

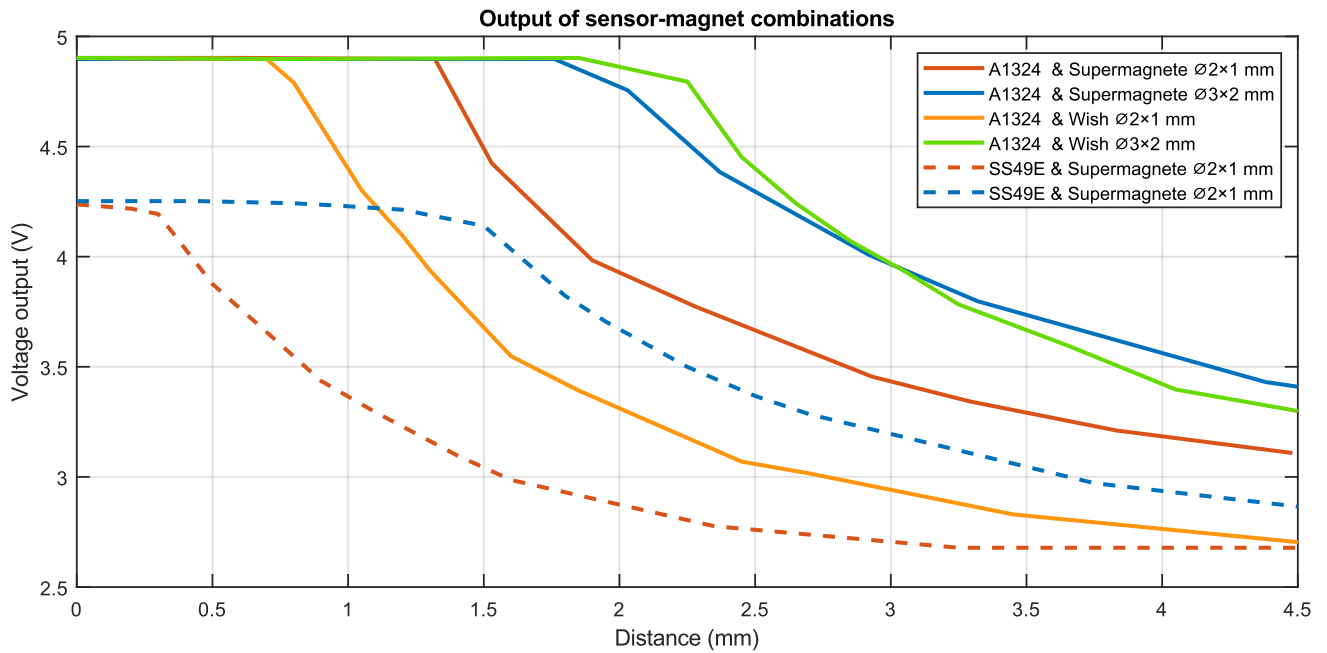


Figure 2: Voltage output of the Hall sensor-magnet pairs at varying distances.

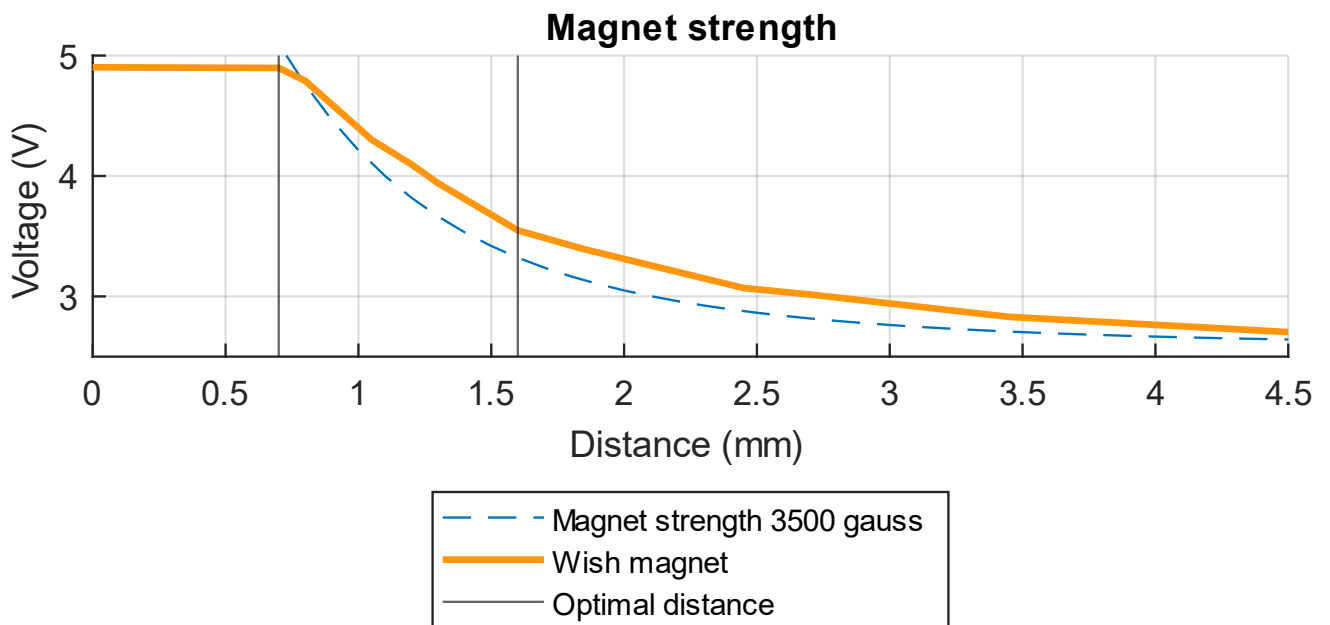


Figure 3: Approximation of the magnet strength of the magnet procured at Wish.

G.4 Conclusion

The mechanism should use A1324 Allegro Hall sensors combined with $\varnothing 2 \cdot 1 \text{ mm}$ Neodymium axial disc magnets from Wish, with a distance ranging from 0.7 to 1.6 mm. The magnet strength was approximately 3500 Gauss.

G.5 References

- [1] "Low-Noise Linear Hall-Effect Sensor ICs with Analog Output A1324, A1325, and A1326." Datasheet, Allegro MicroSystems, 2020. Accessed: Apr. 09, 2021. [Online]. Available: <https://www.allegromicro.com/-/media/files/datasheets/a1324-5-6-datasheet.pdf>
- [2] "SS39ET/SS49E/SS59ET Series." Datasheet, Honeywell International Inc., 2015. Accessed: Apr. 09, 2021. [Online]. Available: <https://prod-edam.honeywell.com/content/dam/honeywell-edam/sps/siot/en->

us/products/sensors/magnetic-sensors/linear-and-angle-sensor-ics/common/documents/sps-siot-ss39et-ss49e-ss59et-product-sheet-005850-3-en-ciid-50359.pdf?download=false

- [3] “How do you calculate the magnetic flux density?,” *Supermagnete*.
<https://www.supermagnete.nl/eng/faq/How-do-you-calculate-the-magnetic-flux-density> (accessed Sep. 18, 2023).